

CHARGE CONJUGATION SYMMETRY
in
PROTON-ANTIPROTON INTERACTIONS
at
5.4 GeV CMS ENERGY

John D Whittaker

A DISSERTATION
PRESENTED TO THE
FACULTY OF PRINCETON UNIVERSITY
IN CANDIDACY FOR THE DEGREE
OF DOCTOR OF PHILOSOPHY
RECOMMENDED FOR ACCEPTANCE BY THE
DEPARTMENT OF
PHYSICS

January 1978

TABLE OF CONTENTS

	Page
ABSTRACT	
CHAPTER I: THEORY AND BACKGROUND.....	1
A) INTRODUCTION.....	1
B) LIMITS ON C, P, AND T CONSERVATION.....	2
C) THE MILLI-SPONG MODEL OF CP VIOLATION.....	5
D) C AND P IN PP SYSTEMS.....	7
E) PREVIOUS RESULTS.....	9
F) REQUIREMENTS OF A NEW TEST.....	12
CHAPTER II: APPARATUS.....	16
A) INTRODUCTION.....	16
B) BEAM AND TARGET.....	17
1) BEAM LINE.....	17
2) BEAM CHERENKOV COUNTER.....	20
3) HYDROGEN TARGET.....	21
C) SPECTROMETER.....	23
1) SCINTILLATION COUNTERS AND TRIGGER.....	23
2) MUON FILTER.....	25
3) SPECTROMETER MAGNETS.....	25
4) THRESHOLD CHERENKOV COUNTER.....	29
5) WATER CHERENKOV COUNTER.....	29
6) WIRE CHAMBERS.....	33
7) READOUT.....	37

11-9-77

CHAPTER III: DATA ANALYSIS.....	39
A) INTRODUCTION.....	39
B) PRIMARY ANALYSIS - TRACK FINDING.....	39
C) SECONDARY ANALYSIS.....	42
D) TERTIARY ANALYSIS.....	43
CHAPTER IV: CHARGE ASYMMETRY AND CORRECTIONS.....	49
A) INTRODUCTION.....	49
B) CORRECTIONS.....	50
1) TARGET EMPTY.....	50
2) PARTICLE MISIDENTIFICATION.....	51
3) PIONS IN INCIDENT BEAM.....	59
C) FINAL ASYMMETRY.....	59
CHAPTER V: CONCLUSIONS.....	62
ACKNOWLEDGEMENTS.....	64
APPENDIX A: MAGNET MEASUREMENTS.....	66
APPENDIX B: BEAM MOMENTUM.....	68
APPENDIX C: BEAM PROFILE MONITOR.....	71
APPENDIX D: DIFFERENTIAL PION ABSORPTION.....	72
FOOTNOTES.....	74
FIGURE CAPTIONS.....	78
TABLE CAPTIONS.....	84

ABSTRACT

The charge conjugation symmetry of the reaction $\bar{p}p \rightarrow \pi^+ + X$ was checked at $\sqrt{s}=5.4$ GeV. The measurement was made with a double arm spectrometer, with each arm triggered independently. Each spectrometer arm had an acceptance of 15 milliradians and subtended an angular range of 16° to 20° in the lab, 77° to 91° in the pion center of mass system, (CMS). The asymmetry $(N^+ - N^-)/(N^+ + N^-)$ was determined at 90° CMS over a P_t range of .5 to 2.7 GeV/c. Corrections were made for target empty, for pions in the incident beam, and for particle misidentification in the spectrometer. The resulting asymmetry was $.0084 \pm .0090$; consistent with zero. The asymmetry introduced by differential pion absorption in the spectrometer was estimated to be .0021. In the P_t regions of .48 to .67, .67 to 1.00, and 1.00 to 2.7 GeV/c, the asymmetries were $.0037 \pm .0115$, $.0178 \pm .0145$, and $-.0025 \pm .0311$, respectively. The corresponding limits on the amplitude ratio $V = \text{Re}(C\text{-nonconserving amplitude}) / (C\text{-conserving amplitude})$ are one half of the asymmetry limits.

CHAPTER I
THEORY AND BACKGROUND

A) INTRODUCTION

Since the discovery of CP violation in K^0 decays, <1>, much theoretical and experimental effort has been applied to find the source of the effect <2>. While much is known of CP violation in the K^0 decay, no other examples of the effect have been found. The transverse momentum transfer to each pion in the K^0 decay is approximately .2 GeV/c; it is noteworthy that all but two experimental tests of C, CP, or T invariance to date have been at low average momentum transfers, <3>. One may conjecture that violation of discrete symmetries is a short distance phenomenon, which would become more evident at high transverse momentum, P_t . In particular, CP violation may have its roots in a P_t dependent C violating interaction. We note that for the reaction $\bar{p}p \rightarrow \pi X$ the transverse momentum transfer, P_t , to an exiting pion is proportional to the q^2 of the reaction. The exact method of calculating the q^2 is highly model dependent; for a general idea we will take the q^2 from the incident \bar{p} to an exiting pion at 90° CMS. Here $q^2 = m_p^2 + m_\pi^2 - \sqrt{s}P_t$, and $q^2 \propto P_t^2$. Models of q^2 dependent symmetry breaking have been proposed, for example Trieman and Pais <4>.

The experiment described here was part of a continuing

program to investigate C-invariance at high momentum transfer. In the following subsections we will discuss the current state of C, P, and T tests as they apply to our experiment.

B) LIMITS ON C, P, AND T CONSERVATION

CPT invariance is nearly universally accepted as a fundamental symmetry of nature. Theoretically, this is supported by the generality of the CPT theorem. Experimentally, the best support comes from the limit on the mass difference of K^0 and \bar{K}^0 , which CPT predicts to be zero. This limit can be inferred from the value of τ_{+-} and the mass difference of the K_L and K_S . A rough estimate yields $(M_{K^0} - M_{\bar{K}^0})/M_K \lesssim 4 \times 10^{-17}$, <5>.

The first discovery of any of C, P, or T violation was that of parity non-conservation in weak decays <6>. When it became known that only left handed neutrinos and right handed antineutrinos exist, <7>, a violation of both C and P was implied. CP conservation was then postulated to be fundamental to weak processes. The discovery of the K_L decay to two pions, with a branching ratio of approximately 2×10^{-3} , showed the existence of a CP violating interaction. With CPT it implied a T violating effect. The origin of this CP violation is at present not known.

At this date the only known violations of C, P, or T occur

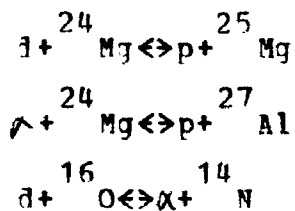
in the weak interactions; however, theories have been proposed which attribute CP violation to the weak, electromagnetic, and strong interactions <2>.

Parity conservation has been checked to a high degree of accuracy in the strong and electromagnetic interactions through measurements of net circular polarization of gamma rays from nuclear transitions. Gamma ray circular polarizations of $-(6 \pm 1) \times 10^{-6}$ have been measured <8>, consistent with weak interaction effects. Thus, if the CP violating force resides in the strong or electromagnetic interactions, the effect must violate C and P.

In the electromagnetic interaction, C-symmetry has been tested by examining the decays $\rho^+ \rightarrow \pi^+ \pi^- \pi^0$. The check has been for an asymmetry between the energy spectra of the π^+ and the π^- . When the data from the three pions were plotted on a Dalitz plot, a +/- asymmetry of $1.5 \pm .5\%$ was found, <9>. This does not include systematic errors, which may be of the same order <10>. One may conclude that C-invariance holds in electromagnetic interactions to at least the 1% level. The limits on the electric dipole moment of the neutron also furnish an indirect test of C-symmetry in electromagnetic interactions. Following Perkins <11>, we estimate an electric dipole moment of charge times a length times a T(P) violation parameter, f. The charge is the unit electron charge. Since an electric dipole moment would violate both T and P, we can choose a weak interaction length, GM, where G is the

fermi coupling constant and where M is chosen as the nucleon mass, set equal to 1. G_M is then $\approx 10^{-5}/M$. In this system of units $\hbar=c=1$. Taking $1/M$ to be the neutron Compton wavelength of 2×10^{-14} cm, we estimate that the EDM $\approx f \times 10^{-19}$ e-cm, where f is the violation parameter. The current limit on the neutron electric dipole moment is $(.4 \pm 1.1) \times 10^{-24}$ e-cm <12>. This implies that PT is conserved to the level of $f \approx 10^{-5}$, and with CPT , C must have the same limit.

In the strong interaction, T invariance has been shown to be correct to better than .3% through the study of detailed balance experiments, <13>. In particular, the angular dependence of the differential cross sections in the reactions and inverses



have been compared to produce this limit.

The current limits on C -noninvariance in the strong interaction will be discussed in subsection E) of this chapter. The next two subsections will discuss respectively the motivation for the tests described in this thesis and the parameters which are measured.

C) THE MILLI-STRONG MODEL OF CP VIOLATION

If the origin of CP violation lies with the strong interaction, it must be a small part of the major strong interaction effects. Various forms of such a model have been proposed in the literature, and will be summarized below.

Prentki and Veltman <14> have suggested a source for C and P violation in the semi-strong interactions, those which violate SU3. These interactions conserve isospin, as is seen through the success of the isospin multiplet classification of particles and through the charge independence of nuclear forces. The authors make an estimate of the size of the effect based on the mass splitting of isospin multiplets. The multiplet splittings are first order in the coupling constant "f" of the SU3 breaking forces, while electromagnetic splittings of charged and uncharged baryons are first order in α . SU3 splittings are on the order of 75 to 150 MeV and electromagnetic splittings are on the order of 1 to 6 MeV. An estimate of 25 to 100 times α is thus obtained for f, yielding C violating contributions of up to 10% in the strong interaction.

Lee and Wolfenstein <15> consider the CP violating Hamiltonian as a combination of two parts, $H_G + H_F$. Here G signifies that the interaction is governed by the usual Fermi coupling constant, and F represents the coupling constant of the

new part. H_G satisfies $\Delta S \neq \pm 2$ and is invariant under CP and T; H_F does not conserve CP. If H_F taken alone satisfies $\Delta S = 0$ and does not contain leptonic operators, then F/G can be as large as 10^3 while being consistent with the $K_L \rightarrow 2\pi$ amplitude. Thus $(4\pi)^{-1} F_m^2 \approx (g^2) \approx 2 \cdot 10^{-3}$. As in the model of Prentki and Veltman, C and T are not conserved, P is conserved. If H_F is chosen to satisfy $\Delta T = 0$ then it may be considered as a small C or T violating part of the strong interaction, otherwise it can be thought of as a totally new force. The model predicts that both the strong and the weak interactions will have C and T noninvariant amplitudes on the order of the $K_L \rightarrow 2\pi$ branching ratio, i.e., about .1%. The $K_L \rightarrow 2\pi$ and other CP or T violating weak processes would then proceed through an H_{GF} term, requiring an intermediate state. The authors also consider an H_F with $\Delta S = \pm 1$ or $\Delta S = \pm 2$, yielding a hamiltonian for weak processes and for superweak processes, respectively.

L. B. Okun¹, <16>, has also suggested a milli-strong model, which is P conserving and CP nonconserving with $\Delta Y = 0$. The coupling constant is $\approx 10^{-3}$ that of the strong interaction, and is also $\approx 10^3$ that of the weak interaction. In this scheme the $K_L \rightarrow 2\pi$ mode is a three step process, involving the milli-strong interaction X, the weak interaction W, and the strong interaction S.

K_L	$W \rightarrow$	i_1	$X \rightarrow$	i_2	$S \rightarrow$	2π
CP=-1		CP=-1		CP=+1		CP=+1
C=+1		C=-1		C=+1		C=+1
P=-1		P=+1		P=+1		P=+1
$Y=+1$		Y=0		Y=0		Y=0

The $\Delta Y=0$, non-leptonic interaction should lead to C and CP violating effects in all strong interactions, at the level of the ratio of the X to S coupling constants, i.e., $\approx .1\%$. The author states that the combined S, W, and X interactions with $\Delta Y=0$ would yield a neutron electric dipole moment on the order of 10^{-23} to 10^{-24} e-cm, which is almost ruled out by current results. The current upper limit on the neutron electric dipole moment is $(.4 \pm 1.1) 10^{-24}$ e-cm, <12>.

In summary, the various milli-strong models predict a C-violating effect in the strong interactions on the order of .1%. If the violation of discrete symmetries is a short distance phenomenon, the effect could be larger at high q^2 .

The next subsection will discuss the parameters by which a strong component of a C-violating effect could be detected.

D) C AND P IN $\bar{p}p$ SYSTEMS

We shall limit the discussion of C-violation in the strong interaction to $\bar{p}p$ systems, which will be shown to be eigenstates

of CP and CR, where R is a rotation of 180° . Pais first discussed the effects of C, P, and CP non-invariance in particle-antiparticle interactions <17>. Following his paper we examine the reactions $\bar{p}p \rightarrow 1+X$ and $\bar{p}p \rightarrow \bar{1}+X$, where 1 and $\bar{1}$ are particle and antiparticle. In the CMS, we consider the effect of the charge conjugation operator C on the initial state of $|\bar{p}(r_1), p(r_2)\rangle$.

$$C|\bar{p}(r_1), p(r_2)\rangle = (-1)^{1+s} |p(r_1), \bar{p}(r_2)\rangle$$

Thus, in general, the initial state is not an eigenstate of C. The operation R, a rotation of 180° about an axis perpendicular to the $\bar{p}p$ line, can be chosen to interchange r_1 and r_2 . The initial state is an eigenstate of CR, and similarly, it is an eigenstate of CP.

Turning our attention to the final state particles, C takes a particle into its antiparticle, and we can choose the axis of R to be perpendicular to the $(\bar{p}, 1)$ plane, so that for r in that plane, R takes r to $-r$. As seen in Fig. 1 c, θ is transformed into $\pi-\theta$. If we denote the probability of finding a particle of type 1 and energy E at angle θ as $W(1, E, \theta)$, then $W(1, E, \theta) = W(\bar{1}, E, \pi-\theta)$. The result also holds for CP. We have tacitly assumed that an unpolarised beam is incident on an unpolarised target, where many interactions average over spin states.

We now consider final state correlations in reactions with three or more particles detected in the final state: $\bar{p}p \rightarrow 1+2+X$ and $\bar{p}p \rightarrow \bar{1}+\bar{2}+X$. We choose the axis for the rotation R to be perpendicular to the $(\bar{p}, 1)$ plane, and let ϕ be the azimuth of 2 relative to the $(\bar{p}, 1)$ plane. As seen in Fig. 1 b, PR yields

$$W(1, E_1, \theta_1; 2, E_2, \theta_2; \phi) = \bar{W}(\bar{1}, E_1, \theta_1; \bar{2}, E_2, \theta_2; -\phi)$$

CR yields, Fig. 1 c:

$$W(1, E_1, \theta_1; 2, E_2, \theta_2; \phi) = \bar{W}(\bar{1}, E_1, \pi - \theta_1, \bar{2}, E_2, \pi - \theta_2; \pi - \phi)$$

and CP yields, Fig. 1 d:

$$W(1, E_1, \theta_1; 2, E_2, \theta_2; \phi) = \bar{W}(\bar{1}, E_1, \pi - \theta_1; \bar{2}, E_2, \pi - \theta_2; \pi + \phi)$$

Thus, charge symmetry violating effects may be separated from P and CP violating effects. Bubble chamber experiments have been done to check both the θ and the ϕ dependence. These experiments have been conducted at lower energies than the experiment reported here, which, however tests only the asymmetry at 90° CMS.

The next subsection will discuss the limits imposed on C-violating strong effects by the bubble chamber experiments.

E) PREVIOUS RESULTS

All previous results on charge symmetry in $\bar{p}p$ interactions have been obtained from bubble chamber data, and all but one have been at significantly lower energies. One of the earliest results was obtained by a group from Columbia University, using the Brookhaven 30" bubble chamber <18>. They investigated the

reactions for stopping \bar{p} 's, $\sqrt{s}=1.9$ GeV, $\bar{p}p \rightarrow \pi^+ + X$ and $\bar{p}p \rightarrow K^+ + X$. The average pion multiplicity for $\bar{p}p \rightarrow n$ at rest is four, $\langle 19 \rangle$, yielding an average P_t per pion of $\approx .27$ GeV/c. The limits obtained on the charge asymmetry $(N^+ - N^-)/(N^+ + N^-)$ are 1% for pions and 3% for kaons. These limits were obtained by forming the χ^2 of the difference in the plus and minus charge distributions for various dynamical variables,

$$\chi^2 = \sum_{i=1}^{N_B} \frac{(N_i^+ - N_i^-)^2}{(N_i^+ + N_i^-)}.$$

Here N_B is the number of bins and N_i is the number of events in each bin. A χ^2 of N_B was expected for no C violating effect. For each distribution, the χ^2 were consistent with no C violating effect. The variance of the χ^2 is $\sqrt{2N_B}$. Thus the uncertainty in the asymmetry is $\sqrt{(\sqrt{2N_B}/N)}$, where N is the total number of counts.

A collaboration at CERN used a 1.2 GeV/c \bar{p} beam, $\sqrt{s}=2.1$ GeV to study both K and π final states $\langle 20 \rangle$. The average pion multiplicity at this energy is five, $\langle 19 \rangle$, yielding an average P_t per pion of $\approx .27$ GeV/c. They were able to measure both θ and ϕ in the multiparticle final states, and could thus test separately CP, C, and P symmetries.

Their results for the ratio of the relevant nonconserving to conserving amplitudes are:

$$V_{CP} = (.4 \pm 1.0) 10^{-2}$$

$$V_C = (.4 \pm 1.0) 10^{-2}$$

$$V_P = (.1 \pm 1.0) 10^{-2}$$

These limits are obtained from the asymmetry $(N-\bar{N})/(N+\bar{N})$ as follows: Let α be the nonconserving amplitude and let β be the conserving amplitude, then

$$N = |\beta + \alpha|^2 = \alpha^2 + \beta^2 + 2\text{Re}(\alpha\beta)^*$$

$$\bar{N} = |\beta - \alpha|^2 = \alpha^2 + \beta^2 - 2\text{Re}(\alpha\beta)^*$$

Forming the asymmetry, we find:

$$(N - \bar{N}) / (N + \bar{N}) = (2\text{Re}(\alpha\beta)^*) / (\alpha^2 + \beta^2) = (2\text{Re}\alpha) / \beta = 2V$$

Where we have taken $\beta \approx 1$. The statistical limits on $\text{Re}\alpha/\beta$ are thus $1/\sqrt{2(N+\bar{N})}$.

A recent paper by a bubble chamber group at Argonne National Laboratory <21> presented results of $\bar{p}p$ at 2.32 GeV/c, $\sqrt{s}=2.5$ GeV. They studied $\bar{p}p \rightarrow \pi^+ \pi^+ \pi^- \pi^-$ and $\bar{p}p \rightarrow K^+ K^- \pi^+ \pi^-$, and as seen in Fig. 2, their results are also consistent with no C violating effect being present.

A Dubna collaboration, <22>, has recently reported results in $\bar{p}p$ at 22.4 GeV/c. This experiment was intended primarily to study the charge asymmetry as a function of y^* , the rapidity in the CMS. This author has replotted the data as a function of CMS angle, Fig. 3. From the figure, there is a distinct leading

particle effect which increases with P_t . This author then fit the data to straight lines using a least squares routine. The asymmetries at 90° CMS thus determined were:

P_t RANGE	ASYMMETRY
0.->.5	.050 \pm .010
.5->1.	.038 \pm .020
1.->1.5	-.020 \pm .080

In interpreting these asymmetries, we must bear in mind that the experimenters were not concerned with producing an asymmetry result, and did not consider the systematic errors from this point of view. One notices that the asymmetry is largest at small momentum transfer, where systematic effects would be expected to be largest. If we ignore the lowest P_t bin, we may conclude that these data are consistent with no C-violating effect being present.

The following subsection will outline the apparatus requirements for a new test of C-violation in the strong interactions.

F) REQUIREMENTS OF A NEW TEST

As seen in subsection D) of this chapter, to test for C-invariance in the strong interactions, it is enough to measure the asymmetry $(N^+ - N^-) / (N^+ + N^-)$ at 90° in the CMS. The reaction

of $\bar{p}p \rightarrow \pi^+ + X$ required an antiproton beam incident on a liquid hydrogen target. The beam was to be of as high an energy as possible to provide the largest P_t 's of exiting particles. As seen in Fig. 6, the antiproton flux is a strongly dependent function of beam energy. The incident momentum was thus restricted by the requirement of a high event rate. Compatibility with a search for charmed mesons using the same apparatus resulted in the spectrometer arms being set at $\pm 18^\circ$ to the beam line, for which 90° is obtained with a 19 GeV/c beam. The data rate proved to be too low at this energy, so a 15 GeV/c beam was used, placing 90° CMS on the outer edge of the spectrometer arm apertures.

The design of the spectrometer was determined to provide an optimum data sample for the asymmetry measurement. The basic requirements were (1) effective particle and momentum identification, and (2) effective elimination of systematic backgrounds. These will be discussed separately below.

Momentum analysis of the charged reaction products required a magnetic field for the bending of particle trajectories, and wire chambers for measuring the trajectories. A Brookhaven standard beam line dipole magnet was chosen, with a gap nine inches across and pole faces measuring eighteen inches by thirty-six inches deep. The magnet current was set for a transverse momentum impulse of ≈ 450 MeV/c providing maximum

momentum resolution in the range 1-5 GeV/c. The wire chambers were chosen to be drift chambers, providing the highest accuracy in track resolution now available.

Cherenkov counters were required to provide information on the $\beta = v/c$ of the particles. When both β and the momentum are known, the particle mass may be deduced, yielding a particle identification. For this purpose, a new design differential water Cherenkov counter was employed to separate protons, kaons, and pions, augmented by a threshold Cherenkov counter to aid in separating out pions above 3 GeV/c.

In order to collect data rapidly, the entire experiment was automated. Scintillation counters were used to quickly select events and trigger the data recording. The scintillators also provided a start signal for the drift timers. To further maximize the data rate, all elements of the spectrometer were designed to be as compact as possible, maximizing the solid angle for the acceptance of reaction products.

The spectrometer was designed for easy removal of systematic errors. The possible sources of systematic errors which were identified were (1) the asymmetry resulting from the different trajectories followed by the positive and negative particles, and (2) asymmetries due to the polarization of the incident beam. The first was easily removed by requiring that the magnet polarity be reversible, with data taking at both polarities. The

second required that the data be taken along two directions, separated by 180° in the CMS scattering plane. For practical reasons an arrangement of two separate spectrometer arms was chosen. The magnets were positioned for vertical bending in order to decouple measurements of production angle and momentum.

The next chapter will discuss the apparatus in more detail.

CHAPTER II

APPARATUS

A) INTRODUCTION

The Brookhaven National Laboratory Alternating Gradient Synchrotron provided the experiment with a beam of negative particles at a momentum of 14.8 ± 0.2 GeV/c, see Fig. 4. Cherenkov counters in the beam line were used to identify antiprotons. The beam was incident on a liquid hydrogen target, and the reaction products were analysed in each arm of a double arm spectrometer. The two identical spectrometer arms were set at $\pm 18^\circ$ to the beam line, see Fig. 5. This configuration permitted the easy removal of systematic effects arising from the apparatus and from beam polarization. The spectrometer magnets were Brookhaven standard beam line dipoles, 18D36's, enlarged to a gap of 9" wide, and measuring 18" vertically by 36" deep. They were run at an $\int B \cdot dl$ of about .45 GeV/c. Each spectrometer arm was equipped with scintillation counters, which provided the data trigger, with drift chambers and multiwire proportional chambers which indicated particle track positions, and with Cherenkov counters for particle identification. The apparatus will be discussed section by section in more detail below.

B) BEAM AND TARGET

1) BEAM LINE

The particle source was the High Energy Unseparated Beam at the Brookhaven Alternating Gradient Synchrotron. Fig. 4 schematically represents the beam line. The extracted proton beam of 28 GeV/c was incident on a heavymet target, measuring 4" in the beam direction. It was 100 mils wide, by 40 mils high, and presented $\approx 177 \text{ gm/cm}^2$ to the beam. Secondary particles were accepted at zero degrees. There were approximately 2×10^{12} protons per pulse on the target, with about 10^7 secondaries accepted by the beam line. At 15 GeV/c nearly 3×10^4 of the secondaries were antiprotons, approximately 10^5 were kaons, and the rest were pions, see Fig. 6. The zero degree production angle minimized secondary beam polarization. Particle production at this target was monitored by a scintillation counter telescope at 90° to the beam direction. Three vertically focussing quadrupoles were followed by two horizontally focussing quadrupoles and by a pair of dipole magnets. Between the dipoles was a lead and brass collimator, C1 on the diagram, which was five interaction lengths thick. The collimator could be set to five different apertures and a beam plug; the largest aperture accommodated the entire beam. The pair of dipoles was followed by a pipe twelve inches in diameter passing through approximately

650" of iron. This was followed by a momentum selecting collimator, C2, with four adjustable jaws, each made of four interaction lengths of steel. The collimator was set to accept a momentum bite of $\pm 3\%$ about the central momentum value. The beam line was optically symmetric about the momentum slit, containing two more bending dipoles and two more pairs of quadrupoles, the pair furthest downstream focussing vertically. The magnets were followed by a twelve inch hole through another 120" of iron, and by a halo absorber, C3, consisting of a 5"x7" hole through approximately five interaction lengths of heavynet and copper. The hydrogen target was centered approximately 300" from the last quadrupole.

The momentum was initially set at 19.0 GeV/c, which would have centered the spectrometer aperture on 90° CMS, for $\beta=1$ particles. The antiproton flux at this energy proved to be too low for efficient data collection. A beam momentum of 15.0 GeV/c was accepted as a compromise value, placing 90° CMS at the outer edge of the spectrometer acceptance, but increasing the antiproton flux. A beam line optics program using published beam line data was employed to set the quadrupole currents to provide a nearly parallel beam at the target. Final tuning of the last bending magnet and of the quadrupoles was done with the beam. The magnets were tuned to maximize the rate of coincidence counts between the left and right arms, maintaining roughly equal rates

in each arm. This corresponded to centering the beam on target, with the maximum beam current hitting the target. Throughout the data taking the beam line magnet currents were monitored and stabilised to better than 1% by a computer control system <23>. Tests of the beam momentum yielded a value of 14.8 ± 0.2 GeV/c; see Appendix B.

The beam was defined further through the use of two threshold Cherenkov counters, BC1 and BC2 in Fig. 4, positioned downstream of the momentum slit. The first contained carbon dioxide at 1.5 psi above vacuum, for detecting pions; the second contained Freon 12 at atmospheric pressure for detecting kaons, <24>. The signals from these counters were used to veto the trigger in the case of a negative pion or kaon impinging on the target.

Two plastic scintillation veto counters, V1 and V2, were positioned just upstream of the target. The first had a 2"x3" aperture, positioned about 30" upstream of the target, and the second had a 2" diameter circular aperture, positioned just upstream of the target box and centered on the 2 1/2" diameter hydrogen flask.

2) BEAM CHERENKOV COUNTER

Antiprotons in the beam were signaled by a differential Cherenkov counter which used carbon dioxide at high pressure as the radiator <25>; see Fig. 7. The phototubes were RCA 8575's, mounted against quartz windows with an optical coupling compound. They were run at positive high voltage to protect the photocathodes from damage due to leakage currents into the surrounding steel. An inner and outer ring of six phototubes each accepted light through one inch wide concentric apertures; see Fig. 8 a. For the purposes of this experiment only the outer ring was used, stopped down to a 1/8" wide annular slit, as shown in Fig. 8 b. The phototube signals were sent into discriminators and thence to a "voter" coincidence unit. During data taking this unit was set to respond on five out of six of the phototube signals, providing a 90% increase in rate over six out of six operation.

An antiproton was signaled by an output from the "voter" coincidence unit in anticoincidence with the outputs from the kaon and pion threshold Cherenkov counters, and with the halo scintillation counters. While monitoring this signal, the gas pressure in the differential counter was varied to produce the curve shown in Fig. 9. The antiproton peak appeared at 230 psi above vacuum, with a half-width of 5 psi, and a 3% flat

background. Throughout the data taking, the counter pressure and exterior temperature were monitored, and the pressure was periodically adjusted to maximize the rate.

3) HYDROGEN TARGET

The target flask, Fig. 10, was a cylinder 9" long by 2 1/2" in diameter made of 10 mil mylar. To preserve right-left symmetry the overlap seam of the cylinder was centered on the vertical axis. The end caps were hemispherically pressed from 10 mil mylar. To minimize the amount of material inside the target volume a collar made of low density plastic was machined to hold the flask from the outside. This method eliminated metal bushings and fill lines inside the flask itself. The only projections into the flask were level sensing resistors extending about one quarter inch inside at the top and bottom. The entire flask was covered with 10 layers of one quarter mil aluminumized mylar "super insulation".

The target flask was centered in an aluminum "clam shell" vacuum box. A 3 1/2" diameter entrance window was provided, as was a 4" wide exit window extending beyond the horizontal and the vertical acceptance of the spectrometer. The windows were of 7 mil mylar.

The flask was kept full by gravity feed from an elevated

reservoir, as shown in Fig. 11 . A bleeder valve on the exhaust line was adjusted to produce just enough back pressure to compensate for the elevation of the reservoir; maintaining a constant level of liquid hydrogen. When the target was full, both the upper and lower resistors indicated a lowered resistance. The target was emptied by closing the exhaust valve. This permitted the boil-off gas to expel the liquid back toward the reservoir. When the lower resistor indicated an empty target, the fill line was closed. Remote indicators signalled the conditions of the top and bottom resistors at all times. A bottle of pure hydrogen gas was attached to the exhaust line and provided a means of warming and purging the system in the event of a freeze-up.

Contaminations of oxygen and nitrogen occasionally caused partial blockage of the exhaust line. The boil-off gas pressure would increase, reducing the liquid level until the pressure was sufficient to break through the blockage. The liquid level would then return to normal. From the observed time that the liquid was low, and from the observed purge time, it was estimated that the level was decreased by 1/2" at worst, an effect which occurred much less than one tenth of the time. Since the fiducial vertical height of the target was taken to be one inch above center, this occasionally cut down into the top one quarter inch of the fiducial volume. The effect was sufficiently

small that no corrections were made for it.

C) SPECTROMETER

1) SCINTILLATION COUNTERS AND TRIGGER

In each spectrometer arm plastic scintillation counters were placed in front of the first wire chambers, and behind the last and next to last wire chambers, as seen in Fig. 5. The positions of the counters are tabulated in Table 1. The front most counter position, S1, contained a pair of detectors. The main counter was 4"x5" and 1/8" thick, with the second being 1"x5" and 1/8" thick. The counters were suspended side by side with their longest axis vertical. The narrow counter was on the beam line side of each arm, and both counters taken together were centered on the arm axis. The counters covered the spectrometer acceptance aperture. The purpose of the separate narrow counter was to permit a software veto of beam halo particles, if that had proven to be a significant background.

The scintillators at the second counter position, S2, covered the active region of the preceding wire chamber. These counters were 1/8" thick, each 30" long and 12" wide. Two of them were hung vertically in each arm, with a small horizontal overlap so that the overall width would not exceed that of the wire chamber. The light was viewed by phototubes at both ends of

each counter.

The final hodoscope at position S3 covered the active chamber area horizontally, but limited the spectrometer acceptance vertically. This limit set a lower bound of approximately 1 GeV/c for particles detected by the spectrometer. The scintillator array consisted of three counters, 1/4" thick, each measuring 16" horizontally and 18" vertically, supported one above another. The entire assembly was centered on the spectrometer aperture.

The signals from all phototubes at each position were summed, and a coincidence made of the three stations, separately for each arm. A signal from either arm in coincidence with a signal indicating an antiproton incident on the target was the trigger for read out of counter and chamber data.

The signals from each phototube were delayed, and tagged in a CAMAC module during a 20 ns window following the trigger. The trigger logic, CAMAC units, and all other data processing hardware were housed in an air conditioned office trailer adjacent to the spectrometer.

2) MUON FILTER

Directly behind the last hodoscopes were the muon filter telescopes. These are shown in Fig. 5. The first section was a tower of three cast iron buoy anchors, each 4'X4' across and 5' tall, resting on a one foot high pad of concrete shielding blocks. This was followed by a layer of scintillation counters, at position S4, and by a second iron tower, resting on the floor. A final layer of scintillation counters, at S5, was placed against this tower, covering the geometric acceptance aperture. The one foot offset of the towers with respect to one another staggered the stacking spaces and small hollow regions of the two towers. Muons of >2.8 GeV/c penetrated both iron towers, muons of >1.4 GeV/c penetrated the first.

3) SPECTROMETER MAGNETS

The spectrometer magnets were two Brookhaven 18036 beam dipoles, positioned on end for vertical bending. The gap was 9" wide, with pole faces measuring 18" high by 36" deep. This geometry permitted a compact spectrometer arm, increasing the geometric acceptance. Data were taken with the magnets in two polarity configurations: A, with the magnetic fields pointing away from the beam line in both arms, and B, with both field

vectors pointing toward the beam line. Fig. 5 shows the A polarity configuration. The magnet polarities were sensed automatically, and were recorded as a bit pattern along with all other event data on magnetic tape. Magnet polarity was switched typically three times every twenty four hours, with both target full and target empty data taken at each polarity.

The field of the 18D36 magnets is highly uniform, so that a detailed point by point field map was unnecessary. Instead, the measurement was made in terms of $\int B \cdot dl$ parallel to the aperture axis. The field was measured using a ten foot long flip coil mounted on a wooden form. The form width, averaged over measurements taken every foot, was 1.988". The coil consisted of three turns of #36 gauge copper wire. The measuring apparatus is described in Appendix A, and is illustrated in Fig. 12 .

Following preliminary checks, to set the current for the desired central $\int B \cdot dl$, measurements were made with the coil parallel to the magnet axis; centered on the points of a one inch grid. The bottom one-half of the magnet in the left arm was mapped at each point on the grid, while the upper half was measured at two inch intervals up to the final two inches near the coils, which were again measured at one inch intervals. The entire volume of the magnet in the right arm was measured in the same manner as the top half of the magnet in the left arm. Again, this was possible because the field was uniform to better

than .1% over the central region.

Flux return plates of 3" steel were mounted parallel to the ends of the magnets. Using a Hall probe, it was verified that the field strength fell rapidly outside the flux return plates. Thus, the ten foot long flip was sufficient to include all significant fringe fields.

For each measurement, the initial reading of the integrating DVM was recorded, and the value with the coil flipped 180° about its longitudinal axis was recorded. The coil was then flipped back 180° to its original position, and the final value recorded. By dividing the difference of the first and last measurements by two, the drift of the DVM at the time of field measurement was determined and subtracted. Since these measurements were repeatable to an accuracy of better than .01%, the majority of the points were measured with only one flip cycle.

During the field measurements the current from the power supply to the magnet was determined by measuring the voltage across a shunt resistor with a sensitivity of 1mV/40 amps. The magnets were designated D05 in the left arm, and D06 in the right arm. During the measurements, D05 was at 56.25 mV \Rightarrow 2250 amps, and D06 was at 56.00 mV \Rightarrow 2240 amps. This yields a transverse momentum impulse, P_t , for the magnets of 438.25 MeV/c for D05, and 438.54 MeV/c for D06. During data taking, these were increased to 2318 and 2310 amps, for P_t 's of 451.75 MeV/c and

452.24 MeV/c. Five months after the experiment was completed, a calibration check was done with an incident beam momentum of $\approx 5\text{GeV}/c$. The reaction $pp \rightarrow np\pi^+$ was used, detecting the p and π^+ . The known mass of the neutron yields a P_t impulse for the magnet of 443 ± 3 MeV/c. Taking into account possible drifts of the power supply current reading systems, the P_t 's of 451.75 and 452.24 MeV/c were used, with uncertainties of ± 5 MeV/c. This results in uncertainties in the momentum bin widths of $\pm 1\%$.

Over the active magnet aperture, the maximum departures from the central field integral were $\pm 1\%$, found in the vicinity of the coils. Software corrections to deviations from the central P_t of the magnet were correspondingly made in the upper and lower one quarter of the magnet. The central region was left uncorrected; here the maximum variations from the central value were $\pm .1\%$, near the pole faces, see Fig. 13.

The corrections were calculated by estimating the point of intersection of the track with the midplane of the magnet and then averaging the corrections in the volume traversed by the track about that point. Since the two inch wide coil already provided an averaging of the field and since horizontally the tracks were within that volume only vertical averaging was done.

4) THRESHOLD CHERENKOV COUNTER

The spectrometer threshold Cherenkov counters were designed to fit inside of the magnets, as shown in Fig. 5. The main body of each counter was made of G-10 and molded fiberglass, eliminating the eddy-current vibrational problems of an earlier aluminum counter. The counter volume was viewed by two phototubes mounted at a right angle to the beam direction, one receiving light primarily from the top half of the counter, and the other receiving light primarily from the bottom. Spherically shaped mirrors were used to direct the Cherenkov light into an air core light guide of aluminized glass. The mirrors and phototubes were mounted in an aluminum housing outside of the magnet gap. The magnetic fringe field inside of the tube shields was measured to be negligible. The entrance and exit windows to the counter were made of ten layers of one quarter mil aluminized mylar. Freon 12 at atmospheric pressure was used as the radiator, having a pion Cherenkov threshold of 3 GeV/c.

5) WATER CHERENKOV COUNTER

The radiator volume for the water Cherenkov counter, <26>, was one and one-half inches thick, twelve inches in diameter, and was filled with distilled water. The outer face was made of

one-eighth inch ultraviolet transmitting lucite. Both inner and outer faces were molded to a spherical shape, with a radius of curvature of $37 \frac{1}{8}$ " ; see Fig. 14 . Cherenkov light was collected and focussed with an aluminum, free standing spherical mirror, having a radius of curvature of 17". This system was chosen for compactness. The radiator meniscus was optically designed to compensate for the angular divergence of incident particles. The annular ring of Cherenkov light was focussed two inches behind a conical mask. The openings in the mask were outlined by curves given by:

$$R = ((R_1 + R_0) / 2) + ((R_1 - R_0) / \pi) \arcsin(\frac{80}{\pi} - 1), \quad R_1 = 9.5";$$

$$R_0 = 7.5".$$

Four of the openings pointed inward and four pointed outward. These rosette sections were separated by one inch gaps, allowing for structural support, and permitting the installation of light buckets. The light buckets were made of aluminized mylar and followed roughly the parameters described by Winston <27>. The phototubes were 8854's, capable of resolving a single photoelectron. Bases for the phototubes were designed with Zener diodes to stabilize the dynode voltages and to prevent the gain from changing at high rates. As with the beam Cherenkov counter, the phototubes were run at positive high voltage with the photocathode at ground to avoid leakage currents through the glass which could destroy the photocathode. To prevent a base

line offset of the phototube output, which was AC coupled, clipping lines were attached, which produced a reflected pulse after approximately sixty nanoseconds.

The phototube pulses were stored in CAMAC ADC's (analog to digital converters), after being delayed. Pulses to the ADC's were accepted during a twenty nanosecond window provided by the trigger. From the height and width of the pulse height distribution, it was deduced that there were between thirteen and twenty photoelectrons collected per event, or about two per phototube. The data were read out via CAMAC and written on magnetic tape.

The phototube voltages were adjusted for a 20 mV pulse from one photoelectron, measured at the ADC input. A sample of data from the first few runs was used to determine the pedestal width. To provide a reference for determining differences and drifts in the phototube gain, the pulse height data were fit to a Poisson distribution. The original fit was made to two parameters: the number of photoelectrons, which gave the width of the distribution, and the number of ADC counts per photoelectron, which took into account the phototube gain. During track reconstruction for each data tape, punched cards were produced giving the pulse height spectrum for each of the phototubes for high energy pions. These data were selected with the requirements of (1) a signal from the threshold counter, (2)

momentum greater than 3.2 Gev/c, and (3) a track passing through the water counter radiator within two inches of the center. When a statistically significant sample was obtained, the spectra were compared with the spectra of the previous sample, and if necessary, the gain correction parameter was changed. During subsequent analysis steps these correction parameters were used to subtract pedestals and to adjust the pulse heights for the variations in phototube gain. The sum of pulse heights in the inner ring, IN, in the outer ring, OUT, and in both rings, SUM, were formed. The $RATIO = (OUT-IN)/(OUT+IN)$ was also calculated for each event, and corrected a small amount for the angle of the track.

The counter was designed to produce signals from particles with $\beta = .95$ to $\beta = 1.0$. Pions were first seen at .42 Gev/c, kaons at 1.5 Gev/c, and protons at 2.8 Gev/c. As can be seen from Fig. 15, the pion/proton separation in terms of RATIO was very good. This graph was obtained by monté-carlo calculations, which were also used to determine the $\beta\gamma$ dependence of RATIO. For a given hypothesis of particle type, the RATIO for a pion, kaon, or proton of a given $\beta\gamma$ was found to be equal to the RATIO for a 3 Gev/c pion minus $1.8/\beta\gamma$:

$$RATIO(\pi, k, p) = RATIO(\pi, 3Gev/c) - 1.8/\beta\gamma.$$

6) WIRE CHAMBERS

Particle tracks were sampled at four locations, using two sets of chambers in front of the magnet, and two sets in back of the magnet; see Fig. 5. The chamber positions and active areas are summarized in Tables 2 and 3. The front most chambers were proportional wire chambers, (PWC's), with 1/8" wire spacing <28>. The remaining stations used drift chambers with one inch drift regions. We used PWC's in the front to reduce the problems of multiple hits on a wire during the drift time window of 500 ns.

The PWC's consisted of an X and a Y plane, X measuring the horizontal position, and Y measuring the vertical position. The wires were held at ground potential and were positioned between aluminum foil planes at positive high voltage. Each wire was equipped with an amplifier and a discriminator. The signals were transported to latches in the instrument trailer via 100 Ω ribbon cables. The signals were delayed approximately 150 ns to permit a trigger test on the scintillation counter signals. When a good trigger was detected, an enable signal 20 ns wide was applied to the CAMAC latch modules, and all wires firing within that time window were recorded.

The drift chamber stations in positions two and three consisted of X and Y planes; the final station consisted only of

a Y plane. Each plane was formed of two units displaced perpendicular to the wire direction by one inch, providing information for determining on which side of the sense wire the track occurred; see Fig. 16 a. Each such unit was composed of three planes of wires. The outer ground planes were made of 2 mil copper-berillium wire with $1/16$ " spacing. One half inch inward from either ground plane were the drift (-HV) and sense wires (+HV). Each drift or sense position was actually a pair of wires displaced perpendicular to the central plane by $\pm 1/16$ "; see Fig. 16 b. The pairs were directly connected and functioned electronically as a single wire. The combination of drift wires, sense wires, and ground planes shaped an electric field for drifting the electrons from a particle track toward the sense wires. During chamber development we had experienced low chamber efficiencies for tracks near the drift wires when single sense and field wires were used; see Fig. 17. The choice of two wires at each position helped to provide a more uniformly linear electric field in the drift region, and yielded 100% chamber efficiency at both ends of the drift region; see Fig. 18.

The drift wires were made of 7 mil copper-berillium wire, while the sense wires were made of .8 mil gold plated tungsten wire. The small diameter of the sense wires provided a high electric field near the wires. When an electron from a particle track drifted into this vicinity, collisions with the chamber gas

molecules yielded an avalanche of electrons at the wire, with a resulting cloud of positive ions expanding away from the wire. Signals on the wires were typically 20 mV high and 50 ns long, when the wires were terminated through a 500 pf capacitor and 500 Ω .

Each wire of the drift chamber was coupled to an amplifier, having a gain of 200, and then to a discriminator. The discriminator threshold was 150 millivolts, and it produced an output pulse approximately 20 ns long. The circuit is given in Fig. 19. The discriminator signals were channelled to a line driving amplifier, and were transported to the instrument trailer by shielded twisted pair wires. The length of this cable delayed the signals sufficiently for the scintillation counter trigger to be formed. The trigger signal was used to start the master clock on the drift timing unit. Each sense wire had its own clock.

The timing unit worked on a vernier principle, using a master clock frequency of 21 MHz and a vernier clock frequency of 24 MHz. Each master clock interval was divided into eight sub-intervals by the vernier; see Fig. 20. The timing resolution was thus 6ns. The drift rate of 500 ns/inch then yielded a spacial resolution of $305/\sqrt{12}$ microns. The vernier clock was started by an input signal from a chamber wire. The number of vernier cycles before a coincidence with a master clock signal was stored in a register on the timing board, along with

the total number of master cycles from the scintillator trigger. This data was read out wire by wire after each event, <29>.

The initially used gas mixture was 80% ethylene and 20% argon. Due to leaks in the chambers, oxygen was present in the gas. Ionisation of the ethylene in the presence of oxygen caused it to polymerize on the wires, and in some cases to form carbon filaments. The chambers were cleaned and a new gas mixture of 82% argon, 8% methane, 8% isobutane, and 2% methylal vapor was employed. The chambers were run for 1000 hours with this mixture, and showed no deterioration in performance. Fig. 21 indicates the linearity of drift velocity with distance from the sense wire for both gas mixtures. A continuous gas flow rate of eight cubic feet per hour through all twenty eight chambers in parallel was maintained at all times. Bubblers were used on the chamber exhaust lines to maintain a small positive pressure inside the chambers.

High voltage efficiency plateaus were measured for all chambers using an on line computer. The efficiency was estimated from the ratio of events with two hits per chamber, (assumed to be adjacent wires), to events with one hit. Recall that adjacent wires were contained in separate chambers, Fig. 16, so that each wire functioned independently of its neighbors. The stated ratio is $E_2/E_1 = \frac{e^2}{2e(1-e)}$, where e is the efficiency of a single wire; $e = \frac{2E_2}{E_1 + E_2}$.

7) READOUT

The data were read out and written on magnetic tape as illustrated in Fig. 22. The data flow was through CAMAC. The CAMAC crate contained a fixed data unit, which provided four data words unique to the file of magnetic tape being written. Included were a start of event word, (alternating 0's and 1's), a run number, a trigger type number, and indicators of magnet polarity and beam energy. Three 16 bit pattern units recorded signals from the scintillation counters, and included four bits of measured magnet polarity data. Cherenkov counter pulse height data was recorded in three eight-input ADC's. Six quad scalers were used to record various signal rates. The PWC latches were fitted in CAMAC modules, as was a special read out module for the drift timers.

The scintillation counter trigger signal was used to gate the ADC's, pattern bits, PWC latches, and the drift timer. Following the signal gate the trigger was vetoed by a dead time signal for 3ms while the data were read into a buffer memory unit, <30>. The unit terminated read out upon detection of an end of event word which consisted of eight 1's followed by eight 0's. A read out from the buffer memory to magnetic tape was initiated at the end of each beam spill, or after 32 events had been accumulated.

The first 500 words of each beam spill were also sent to an HP 2116 computer for a rough on line analysis, <31>. The on line program displayed wire chamber data and Cherenkov pulse height information for one event from every beam spill. The chamber "wire on" positions were displayed on a storage scope, permitting a quick eyeball estimate of track detection efficiency. Chamber and phototube data were also accumulated in histogram form to yield information on wire and tube response frequencies, on drift times, and on Cherenkov counter pulse heights. These features were invaluable for setting up, debugging, and monitoring the apparatus.

Chapter III

DATA ANALYSIS

A) INTRODUCTION

During data taking, a total of 2×10^6 triggers were recorded, representing approximately 5×10^9 antiprotons on target. The data filled approximately 80 magnetic tape reels, which were processed on the Brookhaven CDC 7600 computer.

The data analysis was carried out in four successive steps. A first pass analysis found tracks in the chambers. A second pass computed particle momenta and other particle identification parameters from the basic Cherenkov and track information, and placed some rough cuts on the event quality. The third pass produced plots of numbers of events versus event parameters with cuts on other parameters such as particle type, charge, Cherenkov signals, momentum, and angle of track. The data as binned in plots of the momentum distributions were then used to determine the charge asymmetry with corrections for systematic effects. These steps will be discussed in more detail below.

B) PRIMARY ANALYSIS - TRACK FINDING

The first pass analysis program, <32>, began by assigning

spacial coordinates to the chamber wires which had carried a signal. The program then initiated a search for tracks, beginning in the back of the spectrometer. Fig. 23 summarizes the track search routine. Because each plane consisted of two displaced sections, slopes of the track could be determined when both sections yielded signals. This was accomplished as follows. For tracks normal to the chambers let $t_1 + t_2 = t_c$ be the mean total drift time. From Fig. 16 b, it is seen that tracks at an angle θ with respect to the normal yield $t_1 + t_2 = t_c - \Delta t = t_c - \sin\theta/v_0$, where v_0 is the drift velocity in inches/ns, and where the spacing between planes is one inch. Thus θ can be determined. Using the chamber points and slopes, tracks were projected forward along "roads" of a width reflecting the uncertainty in the track direction. The intersection of a "road" with successive chambers indicated "windows" for further track points. Track positions found within windows were used to extrapolate a road to the next chamber, the process continuing until all chambers had been examined. If a track was found in the chambers behind the magnet, it was projected to the center of the magnet, and that point used as a constraint on roads in the front. A further constraint on tracks in the front was an intersection with the target volume. In this first pass, any event with a track in the back half of the spectrometer (chambers three and four) was saved, even if no matching track was found in

the front.

The program compiled detailed distributions of drift times, and produced a plot of wire activity versus wire number. Track finding efficiencies and track distributions within roads were also compiled. This information was used to assure that the apparatus, in particular the drift timer, was working properly, and that the track finding parameters were correct. A modified version of this program was used to monitor the first 1000 events of one data tape every day.

An output tape was produced by the primary program which contained all the original information for each reconstructed event, plus the track fitting information. The output from four data tapes could be contained on a single secondary tape. The ratio of (events out)/(events in) for this step varied between 35% and 40%.

Before production analysis was begun, data taken with the spectrometer magnets turned off, and at low beam intensity, was used to provide a sample of straight tracks. These were used to determine small offsets of the chamber positions from the surveyed values <33>. The final position values were used in the track reconstruction, and are listed in Table 2 .

C) SECONDARY ANALYSIS

The secondary analysis program, <34>, first placed cuts on the track fit parameters. These cuts are summarized in Table 4. They included conditions on the number of track points, on the quality of the fit, and a requirement on the presence of track points in the front of the spectrometer. For events passing these tests, the pattern bit data were decoded to indicate which scintillation counters had given a signal. The ADC data were adjusted for phototube gain variations, and the ADC pedestals were subtracted to provide the true Cherenkov counter pulse heights. The water Cherenkov variables were computed. These were the sum of all inner ring phototube signals, IN , of all outer ring phototube signals, OUT , of all phototube signals, SUM , and the $RATIO = (OUT-IN)/(OUT+IN)$. Assuming a magnet p_t of .45 GeV/c for all tracks, and using the magnet polarity bits, the particle charge was determined.

Tracks were then checked for correlations with the scintillation counter hodoscopes. Rejections from this test are also listed in Table -4-. The events were classified by incoming particle (antiproton or not), and by the presence of a muon, as detected by the muon filter hodoscopes. For this program, the ratio of (events out)/(events in) varied between 50% and 70%.

D) TERTIARY ANALYSIS

The tertiary analysis program consisted of a particle identification section and a section which produced plots of the data, binned according to event characteristics.

The primary instrument used in particle identification was the water radiator differential Cherenkov counter. To establish the identification cuts on the RATIO signal, a data sample consisting almost entirely of pions was used. This selection required (1) that the threshold counter be "on", i.e. >3.0 ADC counts, (2) that the momentum be between 3.2 and 5.0 GeV/c, and (3) that the charge be negative. Since the spectrometer accepted p^+ primarily from the backward hemisphere in the CMS, and since for p^+ within the chosen momentum range, the spectrometer acceptance was peaked in the backward direction, the antiproton contamination of this sample was much less than the corresponding proton contamination to a positive charge sample. The RATIO signal was histogrammed for this data, and is nearly gaussian; as is seen in Fig. 24. The center and standard deviation of the distribution were determined for each arm separately. For a given hypothesis of particle mass, the measured momentum was used to give $\beta\gamma$. Monté-carlo calculations show that knowing the center of the RATIO distribution for these high energy pions, ($\beta=1$), the center of the RATIO distribution for the given

should be $C = C_{\pi} - 1.8/\delta Y$. To be identified by this criteria, the measured RATIO was required to lie within one standard deviation of the hypothesised central value. The approximation was made that the standard deviation of the RATIO distribution was unchanged with δY .

The same cuts as above, but without the charge requirement, were used to select a data sample for histogramming the water counter SUM. This distribution is a rough gaussian with a long tail, as is seen in Fig. 25. The primary source of the tail was multiple particles simultaneously traversing the radiator; a second source included particles directly hitting the phototubes. Delta rays formed a negligible contribution to this effect. A lower cut of roughly one standard deviation was selected to remove protons, and an upper cut of approximately three standard deviations was selected to remove most multiparticle events. These cuts will be referred to as the "one particle" cuts.

The sum of the outer phototubes only, OUT, was also histogrammed for all particles of momentum between 2.2 and 2.5 GeV/c. A clear peak is seen for pions, and a pile up near zero represents protons. An upper OUT cutoff for protons was thus established; see Fig. 26.

Particles were identified as protons if they passed one of two tests; as outlined in Table 5. In the first test, the momentum was required to be less than 2.8 GeV/c, and the outer

ring of the Cherenkov counter was required to have less than 15 (17) counts in the right (left) arm. In the second test, the momentum was required to be greater than 2.8 GeV/c, the threshold counter was required to be off, (less than 3.5 counts), and the water counter RATIO was required to match that expected for a proton of the given momentum. For protons, most of the events had almost no light in the outer ring, for $RATIO \approx -1$.

Particles were identified as kaons if they were within the cuts on the SUM as determined for single particles, and if the RATIO was correct for a kaon of the given momentum; see Table 5 .

Particles were identified as pions if they passed either of two tests; see Table 5 . In the first test, the threshold counter was required to be "on", the momentum was required to be greater than 2.8 GeV/c, the SUM of the water counter phototubes was required to be within the one particle cuts, and the outer ring of the water counter was required to have more than 15 (17) counts. In the second test, the momentum was required to be less than 3.5 GeV/c, the RATIO was required to fall within one standard deviation of the adjusted pion peak, the SUM was required to be within the one particle cuts, and again the outer ring signal was required to be above the proton cutoff.

Under this scheme, an event could be classified in up to three ways; see Fig. 27 . Approximately 60% of the events were

unclassifiable in any category, due to ambiguous water counter or momentum data. The classification scheme was established so as to maximize the number of actual pions, and to minimize the proton contamination of the pion sample. From the diagram, there is a small overlap in identification of pions and protons. Since these events had a substantial outer ring signal, most of the particles were probably real pions. They were made ambiguous by having a momentum between 2.8 and 3.5 GeV/c, where the threshold counter was just becoming sensitive.

The kaons posed a more difficult problem. Of the events classified as kaons, only 2.4% were not also classified as pions or protons. To estimate kaon production, we used data available from pp interactions. Since in pp interactions at least two baryons must be produced in the final state, data from $pp \rightarrow pp+k+X$ at 19 GeV/c should compare well with $\bar{p}p \rightarrow k+X$ at 15 GeV/c. Using the data presented in Particle Spectra, <35>, for 19.2 GeV/c incident protons with a 2 GeV/c secondary particle at 18° in the lab, we find the production ratio $\bar{\pi}/p^+ = 1$, in agreement with our $\bar{p}p$ data, and $\bar{\pi}/k^- = 10$. The particle identification program yields a $\bar{\pi}/k^-$ ratio of 2.2 for our data, so that only about 1/5 of the so-called kaons actually were kaons. From our observed $\bar{\pi}/k$ overlap, this implies a 6% kaon contamination of the pion signal. A kaon contamination of 6% would require a charge asymmetry of 17% to produce a 1% effect in the pion data. Since

the kaon CMS angle spanned 90° symmetrically, there were no acceptance effects in charge asymmetry. We expect that any kaon asymmetry would contribute less than .1% to the final result, which is well below our statistical limits. The kaon contribution to the proton signal was nearly identical to that of the pion sample, and could be ignored for the same reasons. Thus, any event uniquely labeled a kaon was thrown out of the sample, and those which were ambiguous were taken as pions or as protons.

Following particle identification, the data sample was further refined and binned. Events were selected which had a single identified pion track in at least one arm, and which intersected the vertical dimension of the target within one inch of the target center. These events were sorted according to angle of track intersection with the beam line, according to the p_t of the particle, according to the charge of the pion, according to the arm giving the signal, according to magnet polarity, and according to the target state, (full or empty). The angular bins ranged from 15.1° to 17.2° , 17.2° to 18.8° , and 18.8° to 21.8° in the laboratory, or centered on roughly 80° , 84° , and 88° in the CMS, assuming a pion $\beta \approx 1$. The p_t bins ranged from .48 to .67, from .67 to 1.0, and from 1.0 to 2.7 GeV/c. The uppermost limit is the limit for the production of a single pion pair. About .8% of the events at this stage showed unphysical

momenta, i.e. greater than 8.4 GeV/c, or 2.7 GeV/c P_t , and were removed from the sample. For each magnet polarity of each arm, the data was thus presented in 18 bins in P_t , θ , pion charge, and for each of target full and empty. The data so binned were recorded on tape for further analysis. A typical momentum distribution is shown in Fig. 28 .

Data with protons identified in the spectrometer arms and data obtained with a pion trigger on the incident beam were sorted and recorded in the same manner.

CHAPTER IV

CHARGE ASYMMETRY AND CORRECTIONS

A) INTRODUCTION

For each of the 36 data bins in P_t , angle (θ), magnet polarity (A,B), and arm (L,R), the charge asymmetry $(N^+ - N^-) / (N^+ + N^-)$ was calculated for the target full data. These uncorrected values are shown in Table 6. The format for this table is the same as for successive tables, and will be summarized below. The first column lists the magnet polarity, A or B. The second column indicates the spectrometer arm bin, R or L. The third column indicates the CMS angle bin, 1 centered on 80° , 2 on 84° , and 3 on 88° CMS. The fourth column gives the data counts for positively charged particles, from a full target. The fifth column gives the data counts for negatively charged particles from a full target. Columns six and seven present the data counts for positively and negatively charged particles from an empty target. Columns eight and nine present the results and statistical errors of the normalized subtraction of target empty data from target full data for plus and minus charges, which is described in the next subsection, and is not applicable to this particular table. The tenth column, labeled DELTA, gives the

charge asymmetry; in terms of columns it is $(8-9)/(8+9)$. The errors are statistical. The final column is the algebraic average of DELTA over A and B polarities for each angle bin, for example the first entry is the average of DELTA from rows 1 and 7.

Corrections were made for target empty, for protons in the spectrometer which were misidentified as pions, for pions in the incident beam which were misidentified as antiprotons, and for differential pion absorption in the spectrometer arms. Systematic asymmetries resulting from the apparatus and beam polarization were removed. Finally, the asymmetries from the three angular bins were used to determine the asymmetry at 90° CMS. These procedures will be discussed in more detail below.

3) CORRECTIONS

1) TARGET EMPTY

Data were taken both with the liquid hydrogen target full and empty, with triggers recorded in the ratio of 3:1. This combination was established to maximise the total number of target full triggers for a given run time while keeping the target empty contribution to the statistical error small. The contribution to the statistical error increases as the amount of target empty data decreases. The antiproton flux outside of

deadtimes, i.e., the $\bar{p} \cdot (DT)$ flux, was recorded for all runs. The ratio of total $\bar{p} \cdot (DT)$ for full target to total $\bar{p} \cdot (DT)$ for empty target at each magnet polarity was calculated. These ratios were used to normalize the number of target empty triggers to the $\bar{p} \cdot (DT)$ flux on target full, requiring a factor of 1.7 for A polarity, and 1.5 for B polarity. The normalized distribution was then subtracted from the target full data for each data category separately, removing contributions from the target flask, holder, super insulation, and vacuum windows. The target empty asymmetries are tabulated in Table 7.

2) PARTICLE MISIDENTIFICATION

The next major contamination of the signal was from protons of less than 3.5 GeV/c which were misidentified as pions, due to the simultaneous presence of additional particles in the water counter. This was a severe problem because of the wide angular acceptance of protons in the CMS. Pions were accepted in the CMS angular range of 77° to 92° , kaons in the range of 82° to 103° , and protons in the range of 86° to 129° , where 0° is in the \bar{p} direction. The lower limits were set by a 5 GeV/c particle at 16° in the lab, and the upper limits by a 2 GeV/c particle at 20° in the lab. Since antiprotons from elastic scattering predominated in the forward hemisphere, and protons in the

backward hemisphere, the acceptance asymmetry resulted in a large charge asymmetry for protons. The proton asymmetries were as large as 50% at 1 GeV/c and 20% at 3 GeV/c. The charge asymmetry for protons in the spectrometer, with target empty correction, is shown in Table 8.

To estimate the multiparticle background, a track intersecting the target within one inch of center was required in the L(R) arm, with no track in the back chambers of the other arm, R(L), but with a water counter RATIO appropriate for a pion in that arm. These "opposite arm" particles were probably low momentum pions which were swept away by the magnet. All events were required to have a track in at least one arm, but only .7% of the events had reconstructed tracks in both arms. Thus the contamination of the "opposite arm" signal by real double arm events was negligible. The SUM of all water counter phototube signals was histogrammed for "opposite arm" events and the number of events within the "one particle cuts" was determined; see Fig. 29. These events had satisfied all criteria for a pion of less than 3.5 GeV/c except for the presence of a track. A similar plot was made of the water counter RATIOS for such events, where the cut was on the water counter SUM, and the number of events with the proper pion RATIO were added up from the histogram; see Fig. 30. Results for the two approaches, for either arm, agreed to within 1%. For the R(L) arm, this number of events was

divided by the number of events with reconstructed tracks in the L(R) arm to yield a fraction of events with one particle in each arm, one of which left no track in the rear chambers, but which gave a pion like signal from the water counter. This fraction is taken to be .09.

We note that the probability of having a reconstructed track in the L(R) arm, plus a particle in the R(L) arm water counter which appeared to be a pion, is not equal to the probability that both occurred in the same arm. Our concern, however, is with the contamination of the proton signal by slow pions in the same arm. To correct for the reduction in reconstruction efficiency when there were two particles in an arm, and to correct for kinematic effects, plots of number of events versus the SUM were made of R(L), requiring a track in L(R), with no other cuts. For events with a track in the right arm the number of events within the "one particle cuts" in the left arm was 31604, see Fig. 31. For events with a track in the left arm the number of events within the "one particle cuts" in the right arm was 35218. A second set of SUM histograms was made of R(L), requiring only a track in R(L). Here a distinct central pion peak was seen, with a long tail due to two particles. The events in this tail were taken to be "two particle" events. In the right arm the number of "two particle events" is 23596; see Fig. 32. In the left arm it is 30922. We have chosen the last twenty bins, excluding

the overflow bin, for the width of the tail, corresponding to the width of the one particle cut. This results in an overlap of the two regions by three bins. This is acceptable since the choice of boundary is uncertain and since an equal number of bins is the only reasonable way of comparing the two regions; i. e. following a scenario where the two particle region is a displacement by a constant SUM of a portion of the one particle region. This yields a suppression of .75 for tracks in the right arm and of .87 for tracks in the left arm. The average of both arms is approximately .8. This is taken to be the observed suppression of two particle events with both particles in the same arm, compared to each in a separate arm.

The suppression of "two particle events" from two arms to one was calculated on a separate data sample from that used in calculating the ratio of spurious pion events for the following reasons: (1) the opposite arm data used in calculating the spurious pion signal gave a clean sample of non-tracks which produced pion like water signals, and (2) the suppression factor, which was the crudest part of the estimate, could be determined independently over all pairs of particles, rather than over the subsample of those that had pion signals in the water counter. This latter subsample had the preselection of a pion-like water counter signal, so that in the "same arm" plot, the event would most likely consist of a real pion, providing most of the light,

and some second particle, perhaps also a pion, adding a smaller fraction of the light. Thus, the sample would be enriched with actual pions even outside the "one particle" cuts. The uncut sample reflected only the change in "two simultaneous particle" probability from two arms to one, for any true particle track accompanied by a slow pion.

The procedure described above provided a rough estimate of the fraction of tracks which were accompanied by slow pions. For high energy pions accompanied by a slow pion, the water counter RATIO remained unchanged; however, some events were removed from the sample due to a large SUM in the water counter. Unless there is a sizable correlation between the electric charges of the fast and slow pions, this would not result in a charge asymmetric effect, and so was ignored. There is a known correlation of like charged pairs of pions tending to have smaller opening angles than unlike charged pairs, <36>, but there is no evidence of an overall charge asymmetry in this effect.

For protons accompanied by a slow pion the probability of the event appearing as a high energy pion varied with proton energy. As the momentum increased from 1.5 to 3.0 the proton left an increasing amount of light in the water counter. The more light it left, the less the slow pion contributed to the total signal, and the less was the chance of misidentification. Above a momentum of 3 GeV/c, the threshold counter identified

true pions and removed almost all of the proton background.

In an attempt to arrive at the contamination fractions quantitatively, SUM plots were made with cuts requiring that the track extrapolate to within one inch of the center of the target, and that the RATIO was between -1.2 and $-.75$, (most light in the inner ring, and outside the pion cut). The SUM plots were made for six momentum intervals: 1.2 to 1.5 , 1.5 to 1.8 , 1.8 to 2.1 , 2.1 to 2.4 , 2.4 to 2.7 , and 2.7 to 3.0 GeV/c. The distributions showed a substantial proton peak which became centered at higher SUM values as the average particle energy increased. Below 2.1 GeV/c, the SUM for the particles under the peak was negligible, so that any proton in this range, when accompanied by a slow pion, would appear to be a pion; see Fig. 33. Since the SUM increased with proton momentum, the range of SUMs for a second particle which could be added to a track particle and still be counted as a good pion became shifted downward, due to the upper SUM cut. Because of the shape of the second particle SUM distribution, this had the effect of reducing the number of accepted second particles. The magnitude of the reduction was estimated from the shift in the central position of the proton SUM peak. In the range 2.1 to 2.4 GeV/c, this was the only reducing effect; see Fig. 34 and 35. In the range 2.4 to 2.7 GeV/c, see Fig. 36, the proton SUM distribution was becoming broader, and the proton was contributing a larger fraction of the

total light. As in the range of 2.1 to 2.4 GeV/c the SUM shift resulted in a reduced number of spurious pion signals. The width of the proton SUM distribution also became important in this range because of the spreading of the combined proton plus slow pion SUMS outside of the SUM cuts. The lower 1/3 of the proton SUM distribution when combined with the lower 1/3 of the slow pion distribution, still had too low a SUM to be counted as a pion. The upper 1/3 of the proton distribution, when combined with the upper 1/3 of the slow pion distribution, had too high a SUM. Those events consisting of a proton in the upper 1/3 and a slow pion in the lower 1/3 had more than one-half of the light from the proton, and would be rejected by the low RATIO. Only the combination of a proton in the lower 1/3 and a slow pion in the upper 1/3 would get through the pion cuts, as would any combination of a proton and a slow pion both from the middle 1/3. Thus the total fraction surviving the pion cuts was $1/3 + (1/4 \times 2/3) = 1/2$. In the range 2.7 to 3.0 GeV/c, see Fig. 37, the distribution of proton SUMS was broader and centered higher. The same considerations applied as before, with some additions. One-half of those protons in the middle 1/3 had enough light to dominate over the light of the slow pion, reducing that contribution through the RATIO cut. Most of the protons had a SUM in the upper 1/3, where all combinations were rejected by their proton dominated low RATIO. This effect was estimated to

reduce the number of spurious pion signals by 1/2. Thus, $(1/3 \times 1/2 + 1/4 \times 1/3) \times 1/2 = 1/6$ survived the pion cuts.

The three reducing factors described above for each momentum interval were multiplied to produce the overall proton contamination fractions. These correction factors were given systematic errors of $\pm 40\%$ of their values, due to uncertainties in the estimating technique. The resulting fractions of protons which can give a pion signal are then:

P_+ (GeV/c)	FRACTION
<2.1	.07
2.1-→2.4	.07
2.4-→2.7	.03
2.7-→3.0	.01
3.0-→8.4	.00

As a first order correction, the correction fractions multiplied the number of protons measured in each momentum range, and the result was subtracted from the number of pions in that range. This was done for each bin in angle, P_t , magnet polarity, and target FULL or EMPTY. The data so corrected was used to calculate the charge asymmetry $\Delta = (N^+ - N^-) / (N^+ + N^-)$; see Table 9. The computer code which generated this table incorporated the correction described above in calculating DELTA, using the data tabulated in table 8.

3) PIONS IN INCIDENT BEAM

To correct for any asymmetry due to pions in the incident beam a small fraction of the data were taken at lower intensity, without the antiproton requirement in the trigger. Since there were approximately 300 pions for every antiproton in the beam, this was essentially a trigger on negative pions. A pressure curve of the CO_2 Cherenkov counter indicated a pion contamination of the antiproton signal at the 3% level; see Fig. 9. The entire analysis was carried out on the pion incident data exactly as for the \bar{p} incident data. The asymmetries obtained are shown in Table 10.

C) FINAL ASYMMETRY

The asymmetries, with target empty and proton misidentification corrections, were averaged over A and B polarities, removing exactly any systematic up-down asymmetries in the apparatus. In the left arm, the switch from A to B polarity produced, on the average, a change in the value of the asymmetries of .04. In the right arm, the average change was .27.

The resulting asymmetries represented eighteen bins, sorted

according to left or right arm, angular bin, and P_t range; see Table 9. Within each P_t range, the asymmetries were fit to a straight line and extrapolated to 90° in the CMS. To calculate the CMS angles, the incident beam momentum was taken to be 14.8 GeV/c. A systematic uncertainty of $\pm 2\%$ was assigned to the final asymmetry results based on an uncertainty of ± 0.2 GeV/c in the beam momentum. Within each P_t bin, the average pion momentum within that bin was determined and used to calculate the average CMS angle for each of the three laboratory angle bins.

The χ^2 per degree of freedom of the fits were better than 1.5/DOF in all cases, and averaged to .4/DOF. A linear extrapolation to 90° is reasonable, since the measured pion spectra are nearly flat in this angular region. Thus, near 90° , we expect Δ to be a nearly flat, linear, and an odd function crossing zero near 90° CMS. The data of the Dubna group, <22>, Fig. 2, bears this out.

The measurements from each arm were essentially independent, and were averaged for each momentum range. Since the arms were placed symmetrically about the beam axis, this average removed beam polarization effects.

The pion incident data was independently extrapolated to 90° after subtraction of target empty and proton backgrounds. The χ^2 per degree of freedom for the fits averaged to 1.1/DOF, and was as bad as 2.8/DOF in one instance, presumably due to poor

statistics. The resulting asymmetries were averaged over right and left arms. This result was divided by 33.3 and subtracted from the antiproton incident asymmetries to produce the final results; see Table 11.

The resulting asymmetries for the p_t^+ bins .48 to .67, .67 to 1.0, and 1.0 to 2.7 GeV/c are $.0037 \pm .0115$, $.0178 \pm .0145$, and $-.0025 \pm .0311$. The errors are entirely statistical. The systematic errors produced in the p_t^+ subtraction are of the same order as the statistical errors and are $\pm .014$ for the .5 to .6 GeV/c bin, $\pm .009$ for the .6 to 1.0 GeV/c bin, and 0.0 for the 1.0 to 2.7 GeV/c bin. In all cases, our results are consistent with zero charge asymmetry. The asymmetries from the three bins may be considered as three independent measurements over the momentum range .5 to 2.7 GeV/c. The asymmetries may thus be combined by weighting according to the statistics of each:

$$\Delta_{\text{Overall}} = (\sum (\Delta_i / \sigma_i^2)) / (\sum (1 / \sigma_i^2))$$

$$\sigma_{\text{Overall}} = 1 / \sum (1 / \sigma_i^2)$$

When the data from all three bins are combined, the asymmetry is $.0084 \pm .0090$. In Appendix D the effect of matter in the spectrometer on the differential absorption of π^+ is addressed. A spurious asymmetry of .0021 was estimated, which is probably good to within a factor of two. Because this limit is well within our statistical error, and because of the uncertainty in the magnitude of the limit, we leave it stated separately.

CHAPTER V

CONCLUSIONS

As shown in a previous section, the ratio of Re(C-violating) to (C-conserving) amplitudes is just 1/2 of the asymmetry. In terms of amplitudes, our limits in the respective P_t bins are ± 0.0058 , ± 0.0073 , and ± 0.0156 , or ± 0.005 overall. While these limits are of the same order as those of previous C symmetry tests, this experiment has investigated exclusively high P_t events.

A comparison of the slopes of the data when plotted in asymmetry versus CMS angle was made with the Dubna results. The Dubna data was obtained from a plot of asymmetry versus rapidity in the CMS, y^* , <22>, and replotted as asymmetry versus angle in the CMS, see Fig. 2. For the three P_t intervals which were used, the fitted slopes were:

P_t (GeV/c)	Slope: Asymmetry/Degree
0.0-→0.5	.0036±.0012
0.5-→1.0	.0083±.0018
1.0-→1.5	.0105±.0009

The fitted slopes given by this experiment, see Fig. 38, are:

P_t (GeV/c)	Slope: Asymmetry/Degree
.5-→.6	.0056±.0021
.6-→1.	.0047±.0006
1.-→2.7	.0063±.0065

While the Dubna data shows a distinct increase of slope with P_t , i.e. an increasing front-back charge asymmetry in the CMS, this experiment shows such a trend only weakly. As seen in Fig. 38, the data points for the different P_t regions fall within each others error bars, as do the points from successive angular bins. Moreover, the angular range of the Dubna data is wider, permitting a finer discrimination of slope. Thus, the lack of a clearly defined slope trend in our data is understandable.

In conclusion, the results of this experiment are consistent with no C-violating amplitude in $\bar{p}p \rightarrow \pi^+ X$ to the level of .5%, over the P_t range .5-→2.7 GeV/c. This result is consistent with those obtained at lower P_t , and with the expectations of the milli-strong model, which predicts an effect on the order of .1% at low P_t .

ACKNOWLEDGEMENTS

The author wishes to acknowledge a immense debt to all those who contributed to the success of this experiment. The originator and prime mover in the experiment was Professor V. L. Fitch, who provided leadership and direction during all phases of the effort. M. Witherell, R. Webb, R. Regge, M. May, and R. Kadel all were essential to the design, development, and construction of the apparatus, and contributed vitally to the task of data taking.

Most of the computer code was composed by V. Bearg, M. Witherell, and R. Regge. The expertise and tireless enthusiasm of Victor Bearg was especially appreciated.

The success of the drift timing circuitry was due to the design effort of M. Isailas, who also headed the team that built the system. The dedication and good humor of Ann David was particularly appreciated on this and other projects.

The task of reading out and recording the data was mastered by C. Bopp, who designed and built the computer and tape drive interface hardware.

The author wishes to thank the Elementary Particles Laboratory shop staff for their role in fabricating the wire drift chambers, the Cherenkov counters, and the scintillation counters which formed the operational body of the experiment.

Finally, the efforts of the Brookhaven AGS staff were appreciated for their essential role in installing the apparatus and in providing the particle beam and support facilities throughout the duration of the experiment.

APPENDIX A

MAGNET MEASUREMENTS

During the flip coil magnet measurements, the coil voltage was amplified and integrated by an operational amplifier integrator, as shown schematically in Fig. 12. Here, $V_1 = -GV_0$, where $G = R_f/R_o$ is the gain.

$$\begin{aligned} \text{Then } V_2 &= -1/RC \int V_1 dt \\ \Rightarrow V_2 &= -1/RC \int (-GV_0) dt \\ \Rightarrow V_2 &= G/RC \int V_0 dt. \end{aligned}$$

For the setup used, $R=100k\Omega$, $C=8\mu f$, $G=5$. From Faraday's law, $\mathcal{E} = -1/c \, d\Phi/dt$. Integrating, we find $\mathcal{E}t = -\Phi/c$, where \mathcal{E} is the electromotive force induced in a loop while cutting through an amount of magnetic flux, Φ , in time t . Thus statvolt-seconds is equal to $-1/c \text{ gauss-cm}^2$; converting statvolts to millivolts, gauss to kilogauss, the relation of units becomes $\text{kilogauss-cm}^2 = 100 \times \text{mV-sec}$. Thus $\Delta \Phi (\text{kgauss-cm}^2) = 10^2 RC/G (\text{mV-sec})$ is the change in flux through the loop.

To get $\int B \cdot dl$ for the line along the center of the flip coil, we must divide (1) by two for the 180° flip which reverses the field as seen by the coil, (2) by the number of turns on the coil, which is three, and (3) by the average width of the coil

form, 1.988".

Thus $\int B \cdot dl$ (kgaus-in) = 207.91 X mV-sec. From the Lorentz force law $\vec{F} = q/c \vec{v} \times \vec{B}$, we find that $d\vec{p} = q/c d\vec{x} \times \vec{B}$, and integrating, $p = q/c Bl$, so that P_t (GeV/c) = $(1/1313.22) \int B \cdot dl$ (kgaus-in). Summarising these results, $P_t = .1583 \text{ X (mV-sec)}$.

APPENDIX B

BEAM MOMENTUM

The magnets in the beam line were adjusted for a 15.0 GeV/c beam. A number of calibration checks were made using a 48D48 magnet in the beam line, as shown in Fig. 39. At $223\frac{1}{2}$ " downstream from the magnet center, a horizontally moveable scintillation counter, $\frac{1}{4}$ " wide, and 6" in the vertical direction, was mounted to determine the beam position. This counter was placed in coincidence with the beam pion threshold counter, and normalized to the 90° beam monitor at the production target. The scan was made in $\frac{1}{4}$ " intervals. A magnet current of 1710 amperes was chosen to produce a beam offset of one half the scanner travel, thus allowing room to map the edges of the beam. This produced a measured deflection of 3.96" at the scanner.

A portable Hall probe was used to verify the linearity of the central field as a function of magnet current, between 600 and 2000 amps. A previous field map of the magnet, <37>, provided a calibration measurement of P_t along the central axis, at 3000 amps, and verified the linearity of the field with current 3000 amps; see Fig. 40. Using $\int B \cdot dl$ over a line ± 70 " from the magnet center, the P_t of the magnet was given as

442.9 MeV/c. Since we had the magnet positioned at an angle of 15° to the beam line, the P_t was increased to approximately $442.9/\cos 15 = 458.5$ MeV/c. Scaling this by 1710/3000, the operating P_t under our conditions was 261.6 MeV/c. This implied a beam momentum of 14.73 GeV/c.

An alternative calibration at 3000 amps was also provided, <37>. Using a computer model of the magnet, the P_t was integrated along a track at 15° through the magnet center. This yielded a P_t of 451.8 MeV/c, which implies a beam momentum of 14.5 GeV/c.

Since the magnet had been moved and connected to a new power supply between the previous calibration and our use, an independent measure of $\int B \cdot dl$ was attempted using a ten foot long flip coil. The computer control for the magnet power was not operating when this test was made, so that the magnet current was monitored at the power supply in terms of millivolts across a shunt resistor, which gave 40 amps/mV. Measurements were made at $47.93 \pm .1$ mV, $42.75 \pm .05$ mV, and $75.0 \pm .05$ mV. At the last two values, Hall probe measurements were made for comparison with the previously compiled data. These measurements revealed a 10.9 mV offset on the shunt voltage, which required a correction coefficient varying with magnet current. The first two measurements, with their respective correction factors, yield P_t 's of 262.1 MeV/c and 265.5 MeV/c, and thus beam momenta of 14.75

and 14.95 GeV/c.

Finally, the high pressure Cherenkov counter was used to estimate the beam momentum. The efficiency ϵ of the RCA 8575 phototubes was plotted as a function of frequency, and divided into eight frequency intervals of width b_i . At the center of each interval, the index of refraction n_i of CO_2 was calculated from an empirical dispersion relation <38>, normalized to the observed index at 5460 \AA , <39>. The average index of refraction was obtained by evaluating $\sum_i \epsilon_i b_i / \sum_i b_i = \bar{n} = (7.25 \pm 0.05) 10^{-3}$. This value, combined with the $\cos\theta = 0.994783 \pm 0.000033$, of the differential Cherenkov ring, yields a beam momentum of 14.8 ± 0.2 GeV/c.

The beam momentum as finally used in the data analysis was 14.8 ± 0.2 GeV/c. Superimposed upon this is a $\pm 3\%$ momentum spread allowed by the central momentum slit collimator.

APPENDIX C

BEAM PROFILE MONITOR

A MWPC, similar to those used in the front of the spectrometer, with both X and Y modules, was set up downstream of the target to monitor beam position and size, see Fig. 5. Wires were grouped together for an effective 3/8" resolution. Each group of three wires was attached to an integrator consisting of a $22M\Omega$ resistor and a 500pF capacitor. This in turn was connected to an MOS switch. The circuit is given in Fig. 41. The integrator accumulated charge from the wires, which was read out when a scanner closed the MOS switch. The scanning device consisted of a series of shift registers. As the one "on" bit was sequentially shifted along, it operated the MOS switch attached to that register output. The outputs of all the MOS switches were summed together, amplified, and sent out over a 50Ω cable to be displayed as a beam profile histogram on an oscilloscope.

APPENDIX D

DIFFERENTIAL PION ABSORPTION

Checks were made on the contribution to the asymmetry of the differential absorption of π^+ and π^- by nuclear matter in the spectrometer. The difference of the π^+ and π^- cross sections on protons were averaged over the momentum spectrum of pions to yield $\bar{\sigma}(\pi^+ - \pi^-) = 3.9 \pm .9$ mb/proton $\langle 40 \rangle$.

It is known that $\sigma(\pi^+ p) = \sigma(\pi^- n)$; $\sigma(\pi^+ n) = \sigma(\pi^- p)$. For the isotopically pure nuclear states, ($I=0$), of carbon, oxygen, and nitrogen, the nuclear interaction effects cancel; however, coulomb effects and the interference of the coulomb and strong interaction do yield differential absorptions for these nuclei.

The apparatus contains 1.01 gram/cm^2 of excess protons, mainly from liquid hydrogen and water, and $.031 \text{ gram/cm}^2$ of excess neutrons from fluorine, aluminum, chlorine, and argon. Shielding of these neutrons by other nucleons effectively reduced the neutron density by about a factor of three, for an effective difference of $1.01 - .031/3 = 1.0 \text{ gram/cm}^2$ of excess protons over neutrons.

We define ϕ as the differential probability of a π^- being absorbed in the spectrometer with respect to a π^+ .

$$\text{Then } \phi = 1.0 \times 6.022 \times 10^{23} \times 3.9 \times 10^{-27} = (2.35 \pm .54) \times 10^{-3}.$$

If we split δ up between an attenuation of π^- and an enhancement of π^+ cross sections, then the measured N^+ can be represented as $N_{\text{true}}^+ (1+\delta/2)$, and N^- as $N_{\text{true}}^- (1-\delta/2)$. Dropping the subscript "true", we find that the asymmetry

$$\begin{aligned} \delta &= \frac{N^+ (1+\delta/2) - N^- (1-\delta/2)}{N^+ (1+\delta/2) + N^- (1-\delta/2)} \\ &= \frac{N^+ - N^-}{N^+ + N^-} + \delta/2 = \delta_{\text{true}} + \delta/2. \end{aligned}$$

So that $\Delta\delta = \delta/2 = (1.17 \pm .27) \times 10^{-3}$ is the contribution to the asymmetry.

The coulomb interaction introduces a second order effect, decreasing the $\pi^+ p$ cross section with respect to the $\pi^- n$ cross section and increasing the $\pi^- p$ cross section with respect to that of $\pi^+ n$. For our detector, the average Z of the nuclei was ≈ 7 , the total mass was 8.58 gram/cm^2 , and the average pion momentum was 2.01 GeV/c . As shown in <41>, this yields an asymmetry of $(4.45 \pm .02) \times 10^{-4}$.

The interference of coulomb and strong forces for a pion within the nucleus yields a charge asymmetry which may be estimated using optical model calculations, as shown in <41>. The asymmetry was estimated to be $(4.87 \pm .44) \times 10^{-4}$, <42>.

The total contribution to the charge asymmetry from differential π^+ absorption in the spectrometer arms was thus $2.10 \pm .52 \times 10^{-3}$. We emphasise that this is an estimate, and may be off by as much as a factor of two.

FOOTNOTES

- <1> Christenson, J.; Cronin, J.; Fitch, V.; Turlay, R.; Phys. Rev. Lett. 13, 138, (1964).
- <2> Kleinknecht, K.; Ann. Rev. Nucl. Sci., 26,1, (1976) A review article with an extensive bibliography.
- <3> The exceptions were (1) a test of T invariance in particular electromagnetic channels at SLAC and CEA; Boos, S.; et. al.; Phys. Rev. Lett., 24, 748, (1970) Chen, J. R.; et. al.; Phys. Rev. Lett., 21, 1279, (1968) and (2) a test of C invariance at Dubna, Boos, R. G.; et. al.; Proceedings of the Third European Symposium on Nucleon-Antinucleon Interactions, 441, (1976), Pergamon Press, Oxford.
- <4> Pais, A.; Trieman, S. B.; Phys Lett., 29B, 308, (1969).
- <5> This estimate neglects phase information, which would yield an even lower limit.
- <6> Wu, C. S.; Ambler, E; Hayward, R. W.; Hoppes, D. D., Hudson, R. P.; Phys. Rev., 105, 1413, (1957).
- <7> Goldhaber, M.; et. al.; Phys. Rev., 103, 1015, (1958).
- <8> Lobashov, V. M.; Nazarenko, V. A.; Saenko, L. F.; Smotrisky, L. M.; Kharekevitch, G. I.; Phys. Lett., 25B, 104, (1967).

- <9> Gornley, M. E.; et. al.; Phys. Rev. Lett., 21, 402, (1968)
- <10> Perkins, D. H.; Introduction to High Energy Physics, 113, (1972) Addison-Wesley.
- <11> Ibid., 120.
- <12> Dress, W. B.; Miller, P. D.; Ramsey, N. P.; Phys. Rev. D7, 3147, (1973). Ramsey, N., P.; Bull. Am. Phys. Soc., 21, 61, (1976).
- <13> Weitkamp, W.G.; et. al.; Phys. Rev., 165, 1233, (1968).
Von Witsch, W.; et. al.; Phys. Rev., 169, 923, (1968).
Thornton, S. T.; et. al.; Phys. Rev. Lett., 21, 447, (1968).
- <14> Prentki, J.; Veltman, M.; Phys. Lett., 15, 88, (1965).
- <15> Lee, T. D.; Wolfenstein, L.; Phys. Rev. 138B, 1490, (1965).
- <16> Okun', L. B.; Soviet Journal of Nuclear Physics, 1, 670, (1965).
- <17> Pais, A.; Phys. Rev. Lett, 3, 242, (1959). Pais, A;
Treiman, S. B.; Phys. Rev., 187, 2076, (1969).
- <18> Baltay, C.; et. al.; 15, 591, (1965).
- <19> Kitagaki, T.; et. al.; Symposium on Antinucleon-Nucleon Interactions, CERN 74-18, 269, (1974).
- <20> Dobrzynski, L. et. al.; 22, 105, (1966).

- <21> Chen, C. K.; et al.; Argonne Laboratory pre-print, ANL-HEP-PR-77-22, (1977).
- <22> Boos, E. G.; et. al.; Proceedings of the Third European Symposium on Nucleon-Antinucleon Interactions, 441, (1976), Pergamon Press, Oxford.
- <23> The magnet control system was designed and maintained under the direction of Derek Lowenstein, BNL.
- <24> These counters were used courtesy of the Weisberg group at the University of Pennsylvania.
- <25> The beam Cherenkov counter was used courtesy of Ted Kvcia, BNL.
- <26> Fitch, V. L.; A Broad-Band Focusing Cherenkov Counter. Internal report, Princeton University.
- <27> Hinterberger, H.; Winston, R.; Rev. Sci. Inst., 37, 1094, (1966).
- <28> The proportional wire chambers were used courtesy of A. J. S. Smith, Princeton.
- <29> The time digitizer was designed by Marius Tsailas, and built at Princeton by Marius Tsailas, Ann David, Dick Baherman, and others.
- <30> The digital readout interface was designed and built by Carl Bopp, at Princeton.

- <31> The on-line program was created by Victor Bearg, Princeton.
- <32> The primary analysis program was created principally by Victor Bearg.
- <33> The straight through analysis was done by Mike Witherell.
- <34> The secondary analysis program was produced mainly by Victor Bearg and Rosanna Regge.
- <35> Grate; Hagedorn; Ranft; Particle Spectra, CERN publication, (1970).
- <36> Goldhaber, G.; et. al., Phys. Rev. Lett., 3, 181, (1959).
Goldhaber, G.; et. al.; Phys. Rev., 120, 300, (1960).
- <37> The magnet measurements were provided by the Engles group of Carnegie Mellon University.
- <38> Cuthbertson, C.; Cuthbertson, M.; Proc. Royal Soc., 97A, 152, (1920).
- <39> Hays, E. R.; et. al.; Argonne National Laboratory Report, ANL6916, Chemistry, (1964).
- <40> H hler, G.; et. al.; Z. Physik, 180, 430, (1964).
- <41> The differential absorption problem in this apparatus is analogous to that analysed by Robert Webb in his doctoral thesis: Webb, R.; Princeton University Technical Report #3, 48, (1972).
- <42> A modified version of a computer program written by Robert Webb for another spectrometer was used to compute this result.

FIGURE CAPTIONS

- 1- A) Coordinates for $\bar{p}p \rightarrow 1+2+X$
 - B) Action of PR on $\bar{p}p \rightarrow 1+2+X$
 - C) Action of CR on $\bar{p}p \rightarrow 1+2+X$
 - D) Action of CD on $\bar{p}p \rightarrow 1+2+X$
- 2- CMS angular distributions for π^+ and π^- in $\bar{p}p \rightarrow \pi^+ \pi^+ \pi^- \pi^-$ at 2.32 GeV/c.
- 3- CMS charge asymmetry in $\bar{p}p \rightarrow$ anything at 22.4 GeV/c.
- 4- Schematic representation of the 14.8 GeV/c beam line at BNL.
- 5- Plan view of the double arm spectrometer.
- 6- A plot of π^- , K^- , and \bar{p} fluxes in the High Energy Unseparated beam at BNL.
- 7- The high pressure carbon dioxide differential Cherenkov counter.
- 8- A) Light buckets for the beam Cherenkov counter
 - B) Aperture mask for the beam Cherenkov counter.
- 9- Pressure curve of the beam Cherenkov counter.
- 10- The liquid hydrogen target flask and vacuum box, end and side views.
- 11- Schematic representation of the liquid hydrogen filling system.

-12- Schematic representation of the flip coil voltage integrator.

-13- Measured deviations of the 18036 field from the central value, in units of .01%.

-14- Sectional view of the water differential Cherenkov counter, with a view of the rosette light mask.

-15- Monté-Carlo plot of the particle separation in the water Cherenkov counter, based on the RATIO parameter.

-16- A) Sectional view of a drift chamber plane, demonstrating the offset of the two structural units

B) Sectional view of a drift chamber plane, with the doubled sense and drift wires, demonstrating the definition of track slope.

-17- Drift chamber efficiency with single drift and sense wires, using ethylene as the chamber gas. Notice that the efficiency at the drift wire does not plateau at 100%.

-18- Drift chamber efficiency with doubled drift and sense wires. Notice that the efficiency at the drift wire plateaus much earlier than in the single wire case, and reaches 100%.

-19- The circuit for the amplifier/discriminator card at each sense wire.

-20- A demonstration of the functioning of the vernier clock.

- 21- Drift time versus distance plots for ethylene and argon-isobutane- methane-methylal.
- 22- The data read-out and recording system.
- 23- The track search routine of the primary analysis program.
- 24- A typical plot used in determining the center and width of the `RATIO` distribution for pions. The data are from the left arm, requiring a threshold Cherenkov signal of more than 3.5 counts, a particle momentum of greater than 3.5 GeV/c, and a particle of negative charge.
- 25- A sample plot used in determining the center and width of the `SUM` for a single particle. The data are from the left arm, requiring a threshold Cherenkov signal of more than 3.5 counts, and a particle momentum of greater than 3.5 GeV/c.
- 26- A typical plot used in setting the proton limits in the `OP` parameter. The data are from the right arm, with a requirement that the particle momentum be in the range of 2.2 to 2.5 GeV/c.
- 27- A typical distribution of particle identifications.

-28- A typical P_t distribution. The cuts required a positive pion in the right arm, with a track intersecting the target vertically within one inch of center, and required that the angle of the track be between 17.2° and 18.8° in the lab, falling in the central angular bin; centered at about 84° CMS.

-29- A typical plot of the water counter SUM from the right arm, for "opposite arm" events, requiring that a particle track in the left arm intersected the target vertically within one inch of center, and that the RATIO was in the pion region, i.e., -0.7 to -0.05 . The data plotted correspond to 103,676 events in the left arm. The events within the one particle limits are shaded.

-30- A sample data plot of the water counter RATIO from the left arm for "opposite arm" events, requiring that a particle track in the right arm intersected the target vertically within one inch of center, and that the SUM was within the one particle limits. The data plotted correspond to 97,732 events in the right arm. The events which fall within the pion RATIO limits are shaded.

-31- An example plot of the water SUM for "opposite arm" events, with no cuts on the data. Events within the one particle limits are shaded.

-32- A typical plot of the water counter SUM for tracks in the right arm, with no cuts on the data. Events outside of the single particle limits are shaded.

-33- A plot of the water counter SUM for the right arm. Cuts restricted the momentum to the range 1.8 to 2.1 GeV/c, required a track in the right arm to intersect the target vertically within one inch of center, and required a water counter PATIO suitable for a proton, i.e., -1.2 to -.75.

-34- This is the same plot as seen in Fig. -29-, partitioned to demonstrate the effect of the proton momentum on the range of "opposite arm" slow pions which were combinable with a proton.

-35- A plot of the water counter SUM for the right arm. Cuts restricted the momentum to the range 2.1 to 2.4 GeV/c, required a track in the right arm to intersect the target vertically within one inch of center, and required a water counter PATIO suitable for a proton, i.e., -1.2 to -.75. Notice that the proton peak has moved out from zero and is broadening.

-36- A plot of the water counter SUM for the right arm. Cuts restricted the momentum to the range 2.4 to 2.7 GeV/c, required a track in the right arm to intersect the target vertically within one inch of center, and required a water counter RATIO suitable for a proton, i.e., -1.2 to -.75. Notice that the proton distribution is becoming broader than in the previous figure.

-37- A plot of the water counter SUM for the right arm. Cuts restricted the momentum to the range 2.7 to 3.0 GeV/c, required a track in the right arm to intersect the target vertically within one inch of center, and required a water counter RATIO suitable for a proton, i.e., -1.2 to -.75.

-38- A plot of the final data points.

-39- Plan view of the spectrometer with the 48D48 magnet and scintillator scanner in the beam line, as used for measuring the beam momentum.

-40- A plot of Hall probe voltage versus magnet current, (given in mV shunt, with 40 Amps/mV), for the 48D48 magnet.

-41- The circuit for the beam scanner read-out.

TABLE CAPTIONS

- 1- Locations of the scintillation counter stations. The center line of the magnet in each arm is the origin, and is 109.5" from the center of the target.
- 2- Locations of the wire chambers in each arm. The center line of the magnet is the origin.
- 3- Active areas of the wire chambers.
- 4- Secondary analysis cuts and rejection rates.
- 5- Summary of particle identification criteria.
- 6- Pion charge asymmetries and data with no corrections; antiproton incident on target.
- 7- Pion charge asymmetries and data for target empty; antiproton incident on target.
- 8- P^+ charge asymmetries and data for antiproton incident on target; with target empty correction.
- 9- Pion charge asymmetries and data for negative pions incident on target; with target empty and proton misidentification corrections.

-10- Pion charge asymmetries and data for antiproton incident on target; with target empty and proton misidentification corrections.

-11- The charge asymmetries extrapolated to 90° CMS; demonstrating the pion incident background subtraction, and summarising the results.

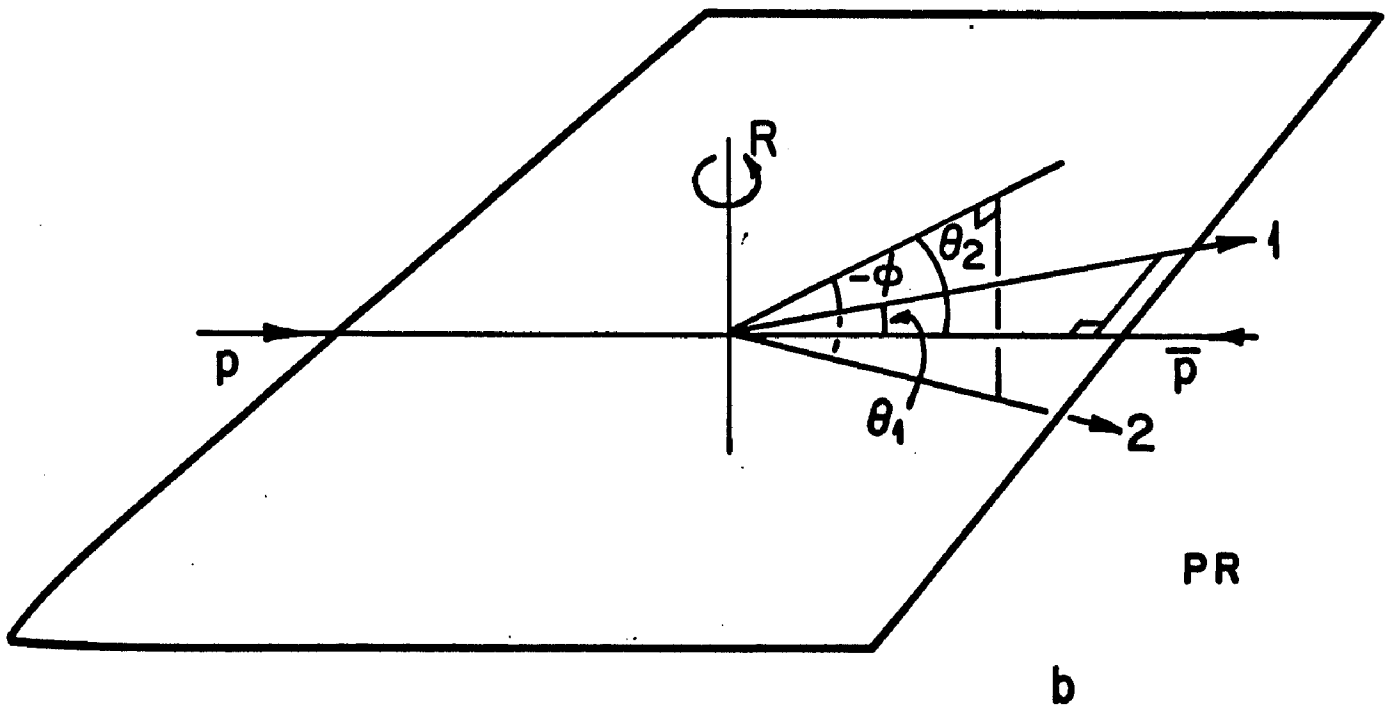
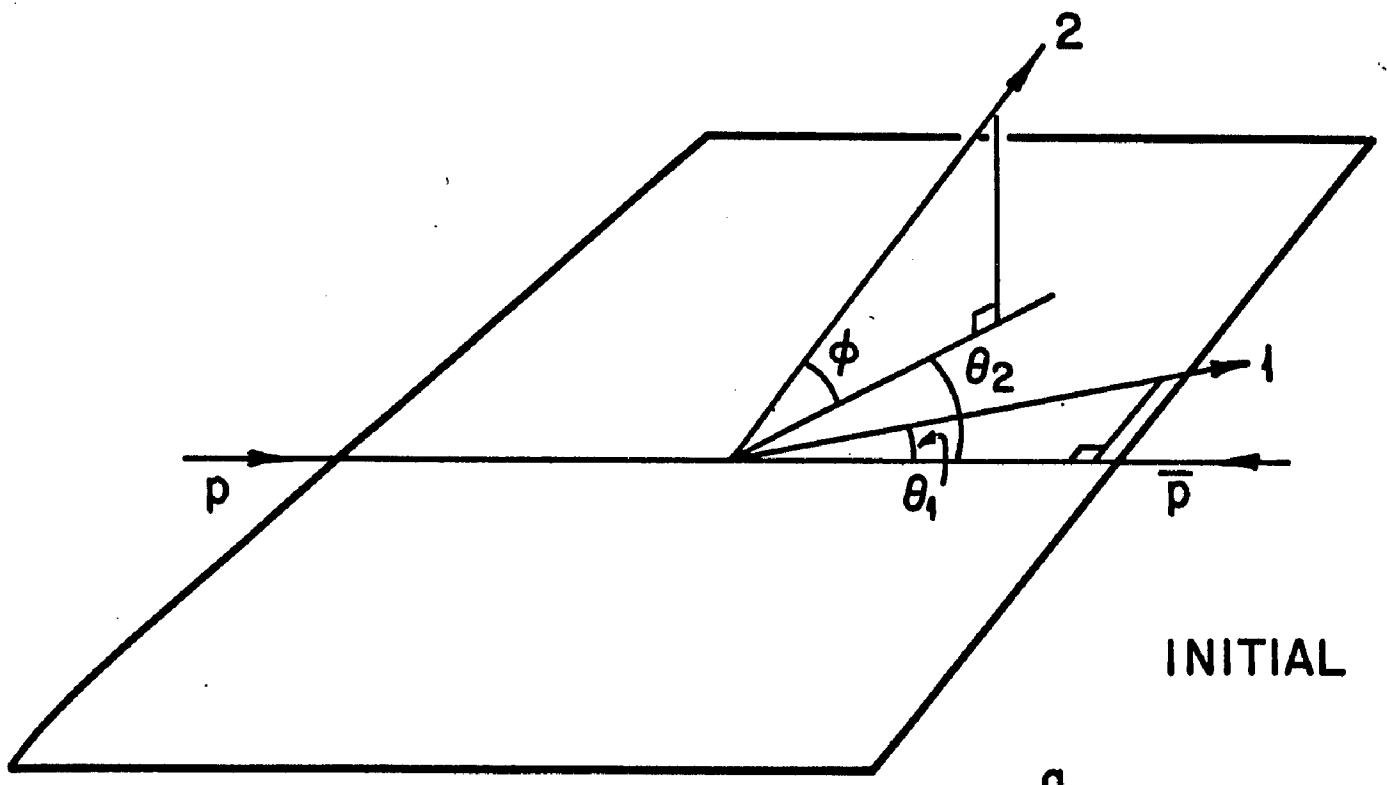


Figure 1

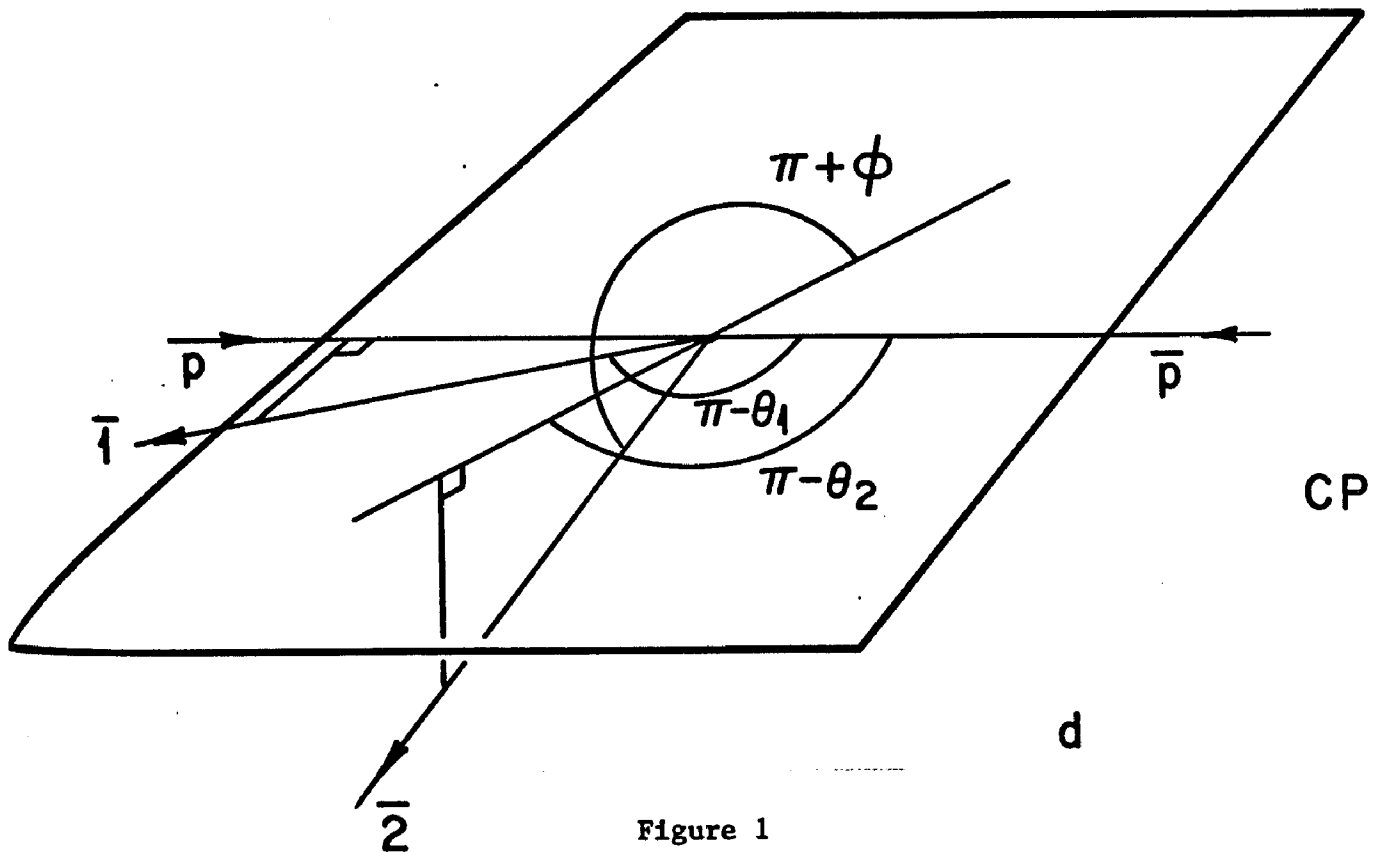
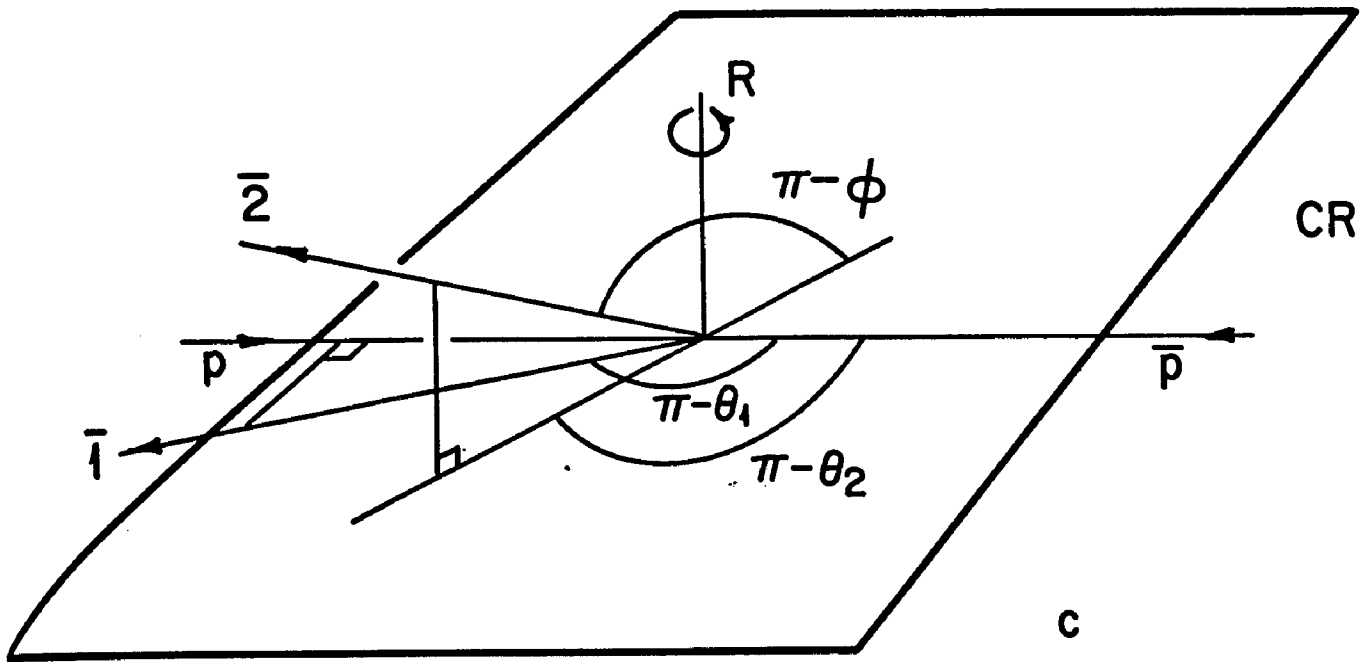


Figure 1

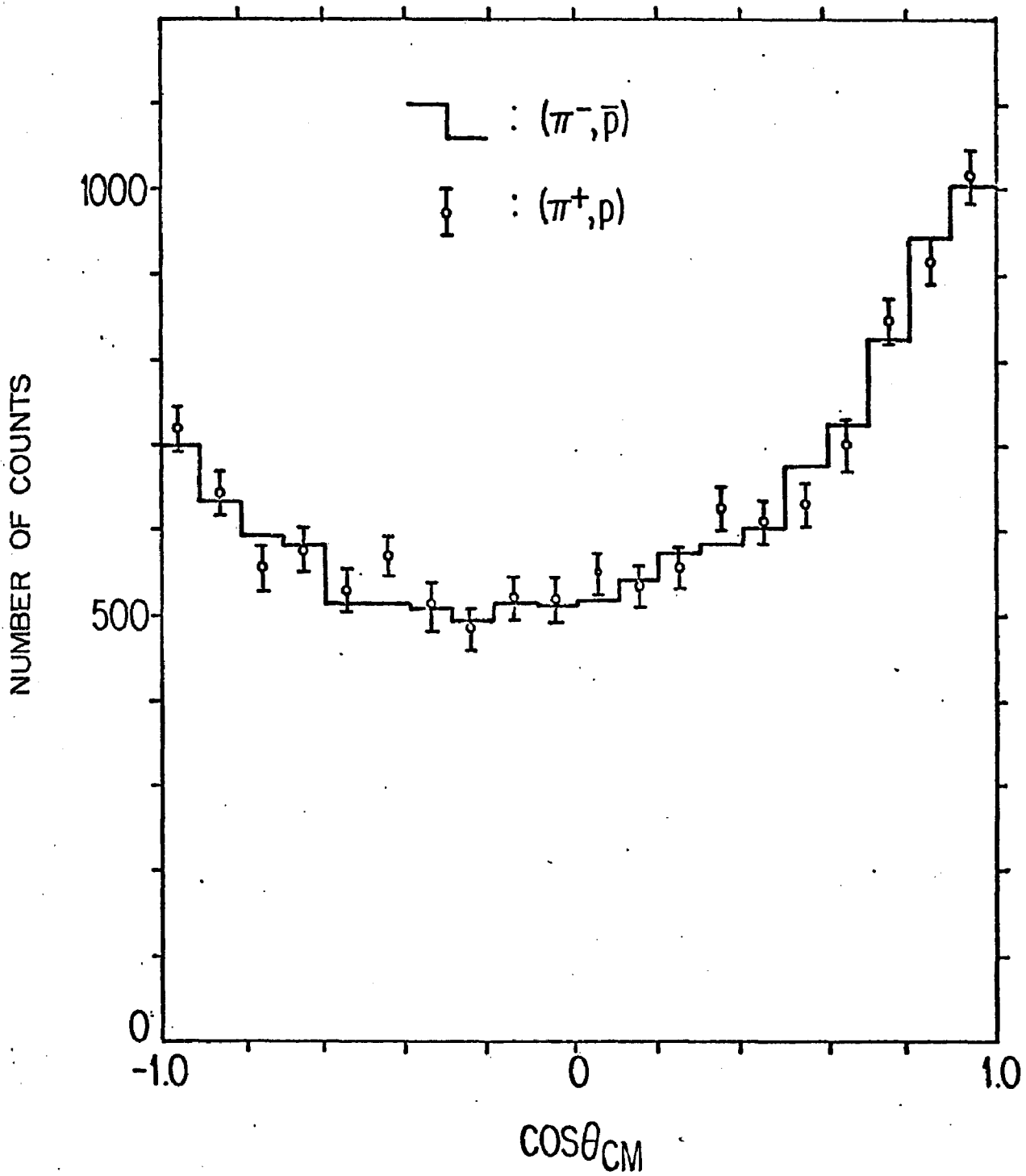


Figure 2

22.4 GeV/c $\bar{P}P \rightarrow X$

P_{\perp} {
• 1.0 GeV/c \rightarrow 1.5 GeV/c
x .5 GeV/c \rightarrow 1.0 GeV/c
○ 0 GeV/c \rightarrow .5 GeV/c

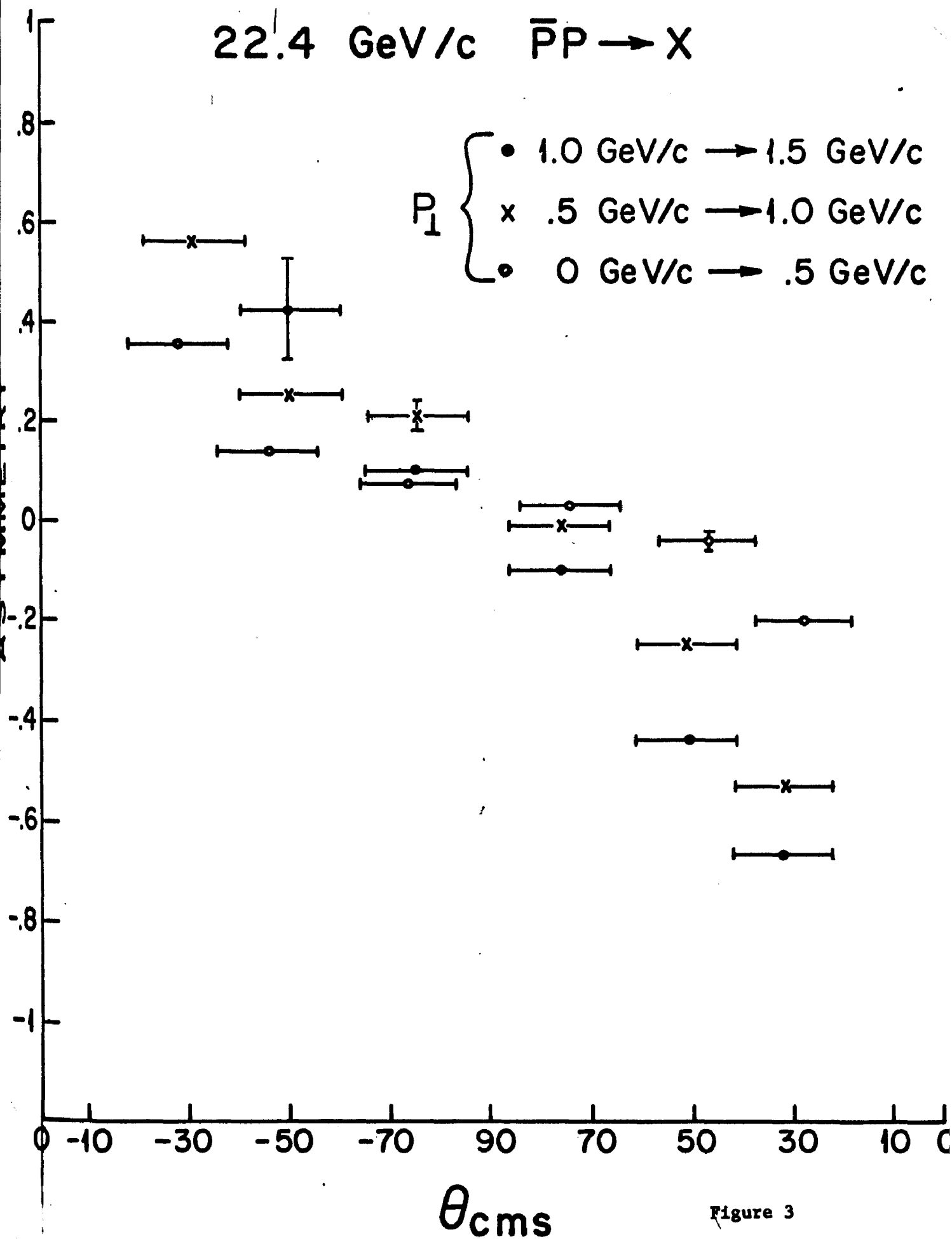


Figure 3

BNL AGS UNSEPARATED BEAM 0° PRODUCTION

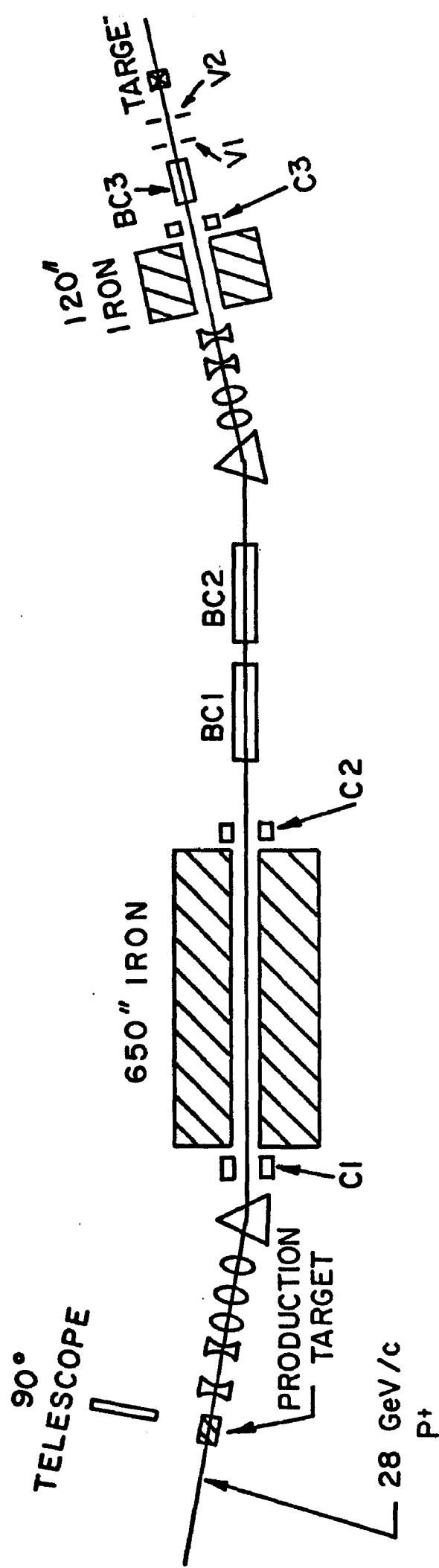


Figure 4

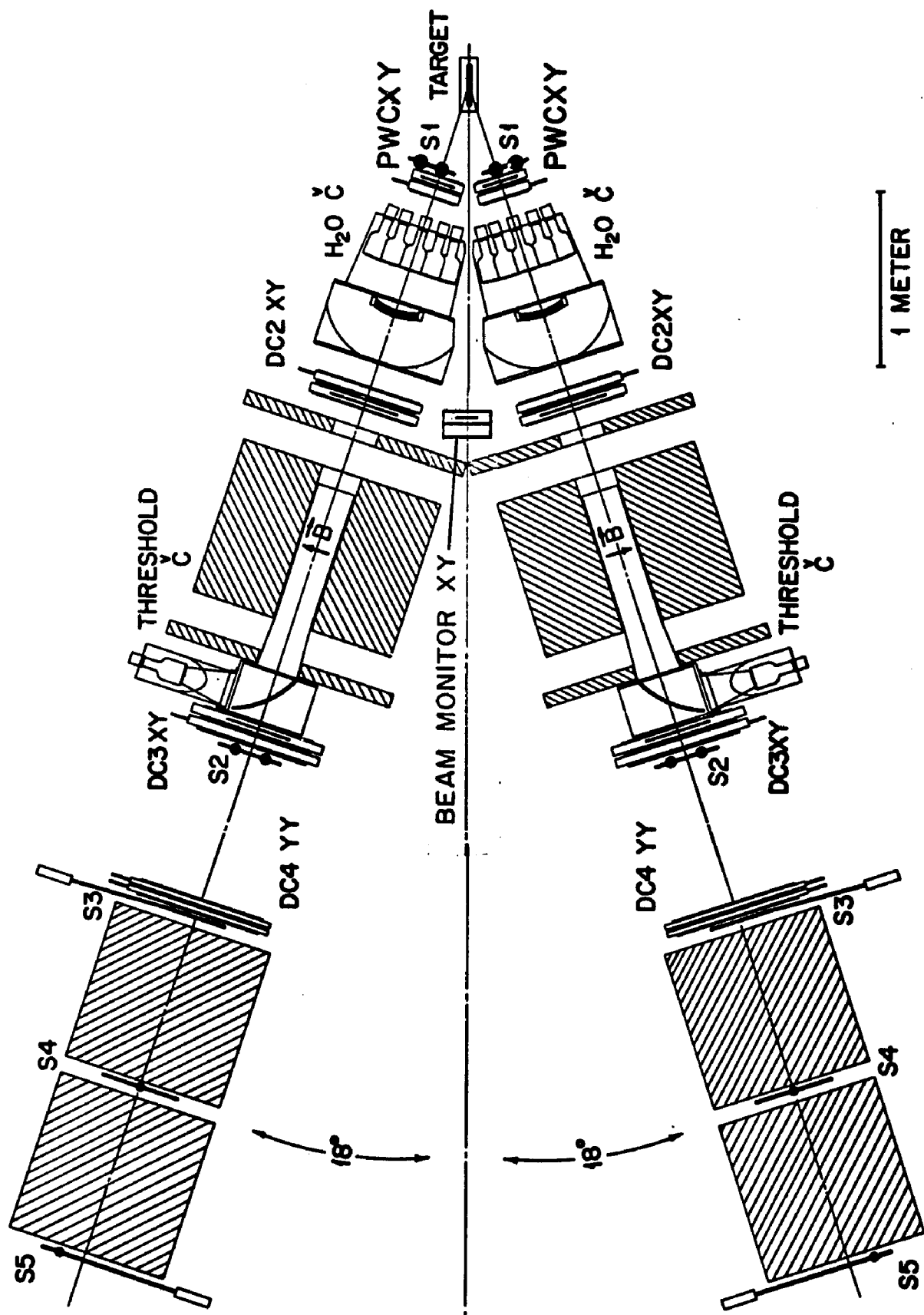


Figure 5

PARTICLE FLUXES
BI (HEUB) BEAM

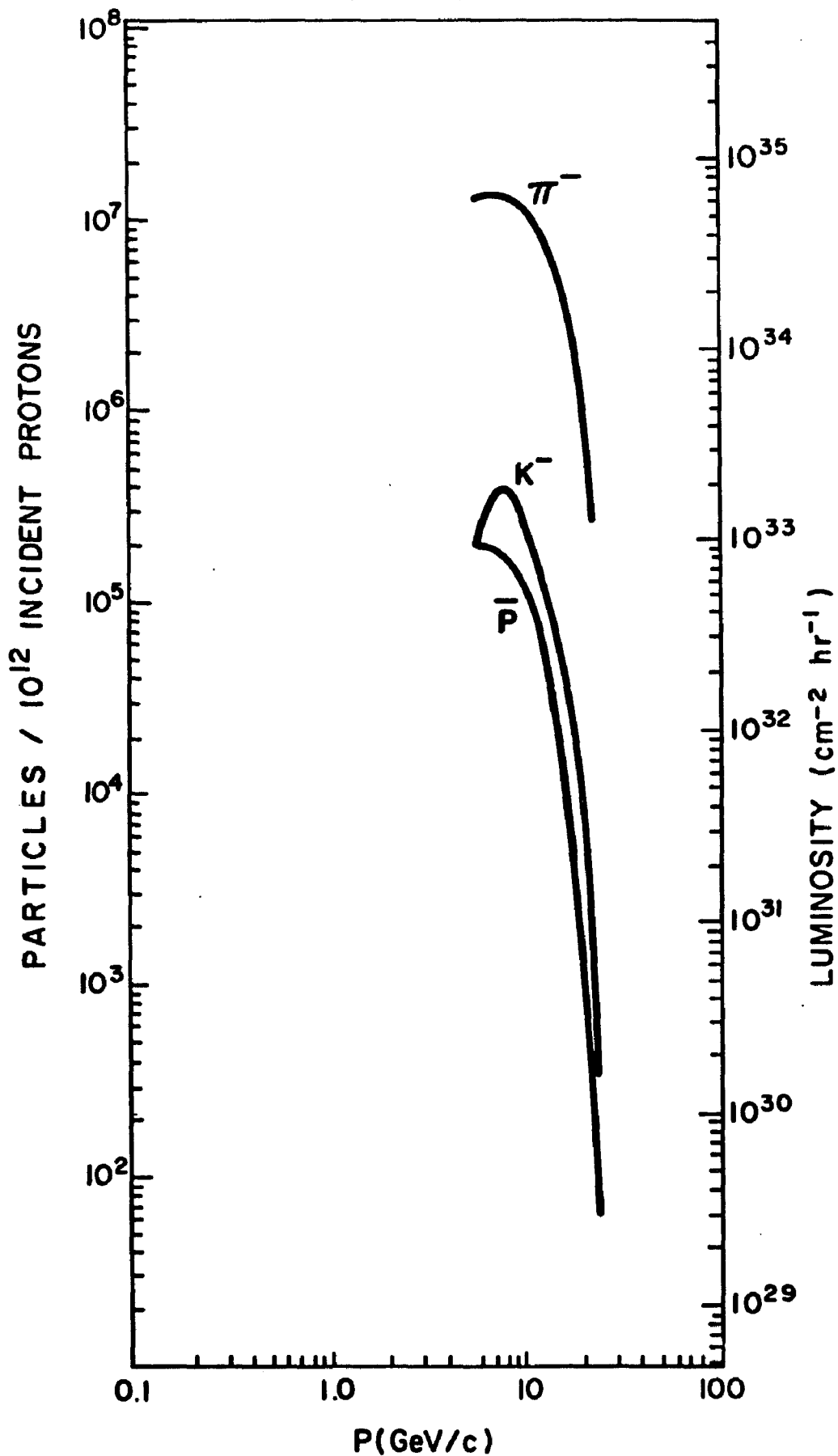
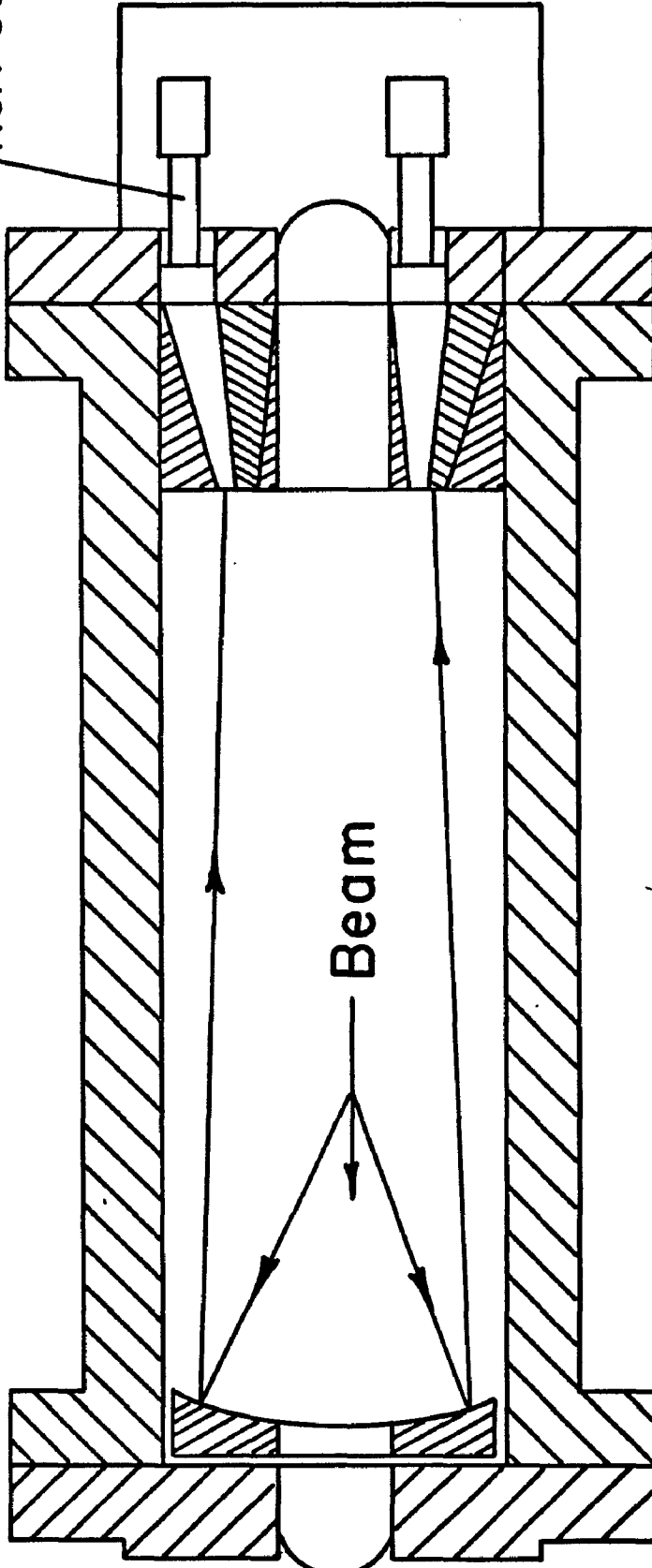


Figure 6

RCA 8575

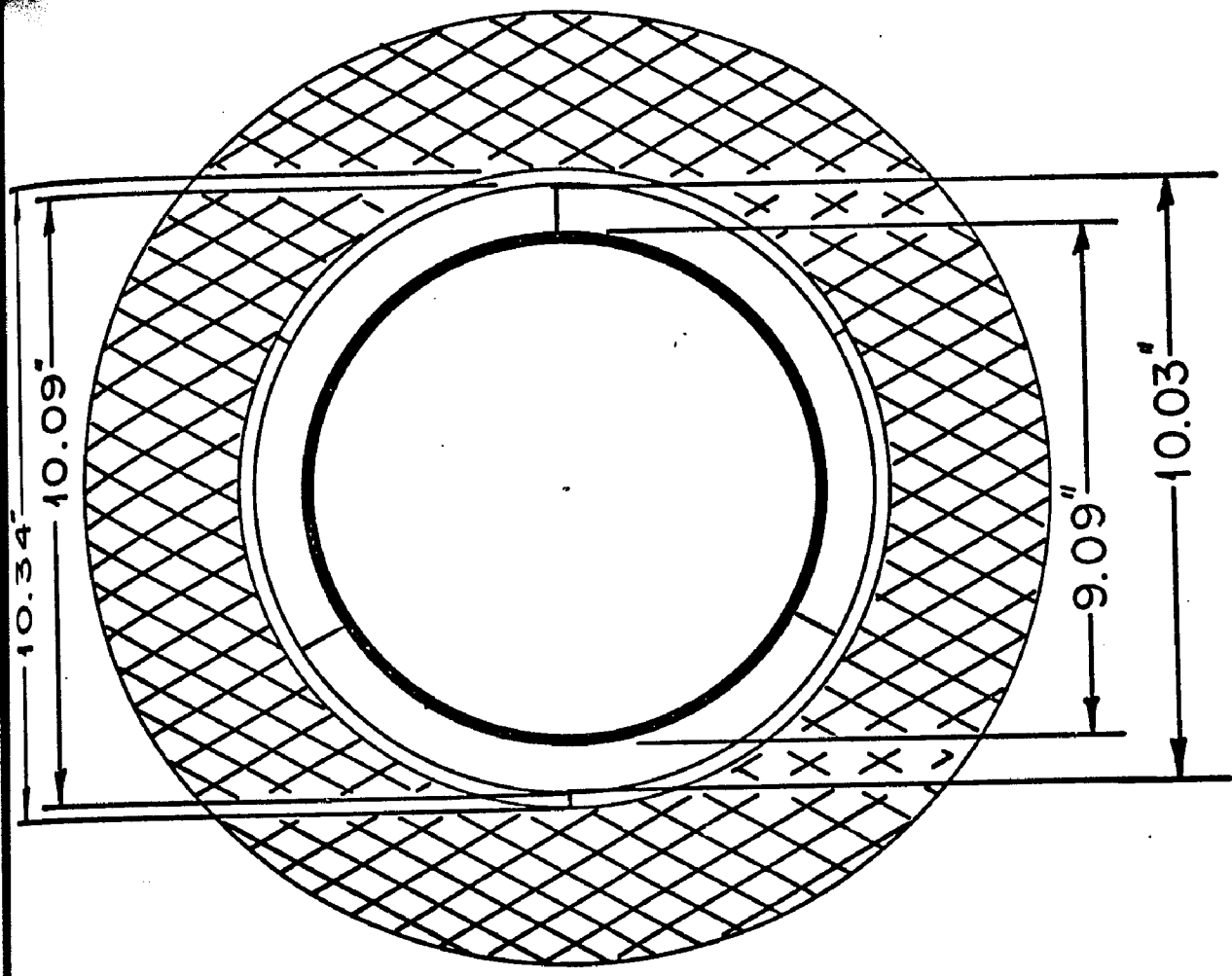


ALUMINUM WINDOW

Beam

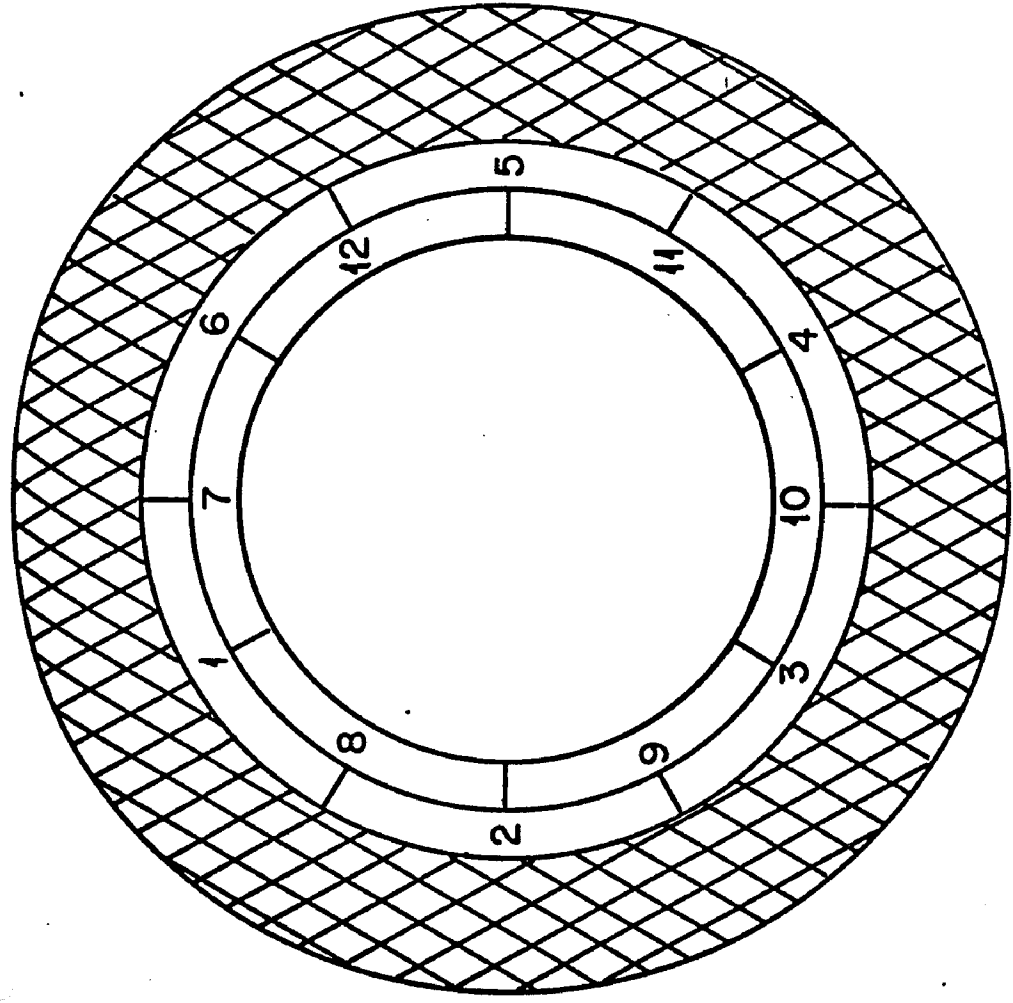
BEAM CHERENKOV COUNTER

Figure 7



Aperture Mask

b



Light Buckets

Front View

a

Figure 8

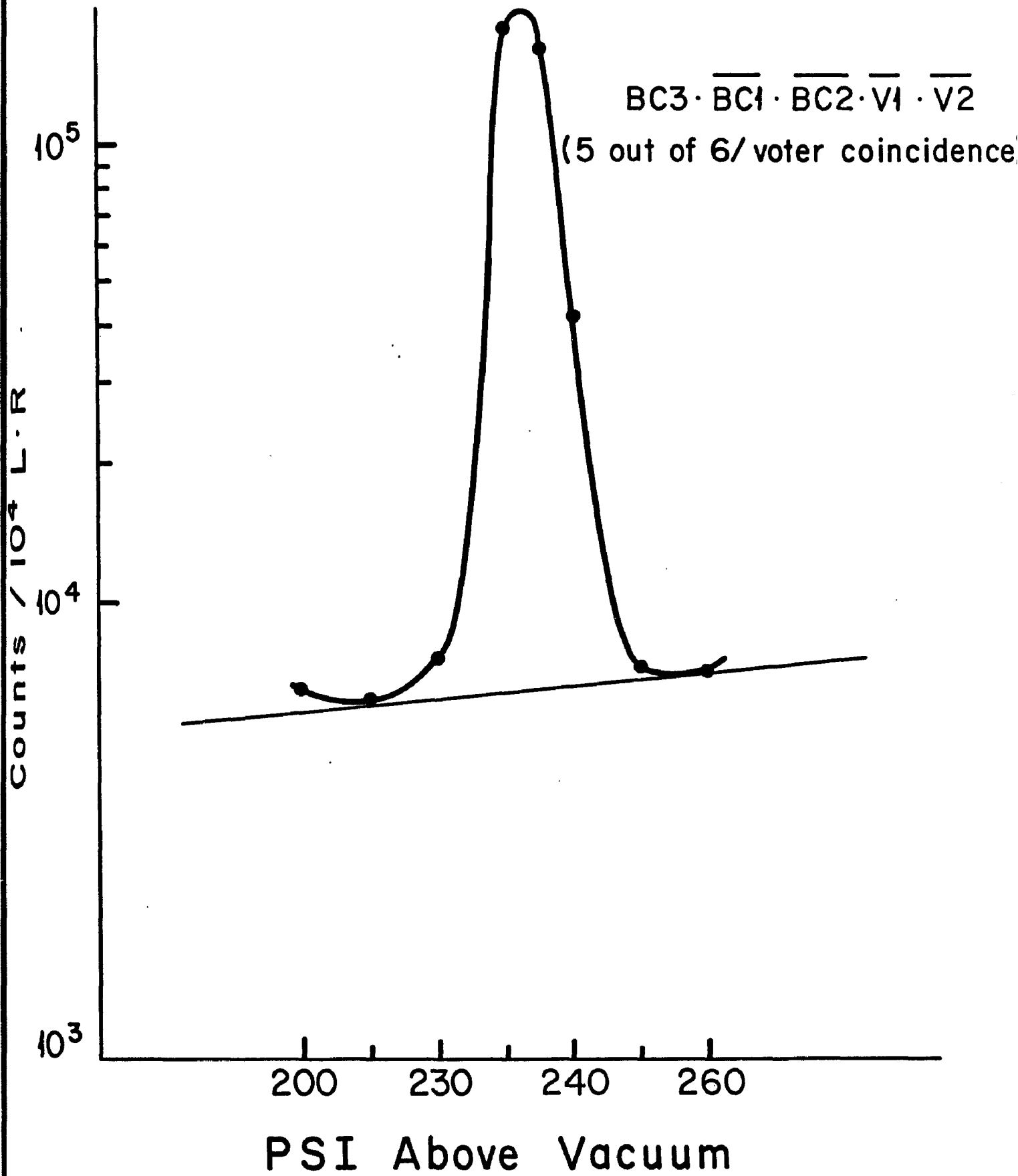


Figure 9

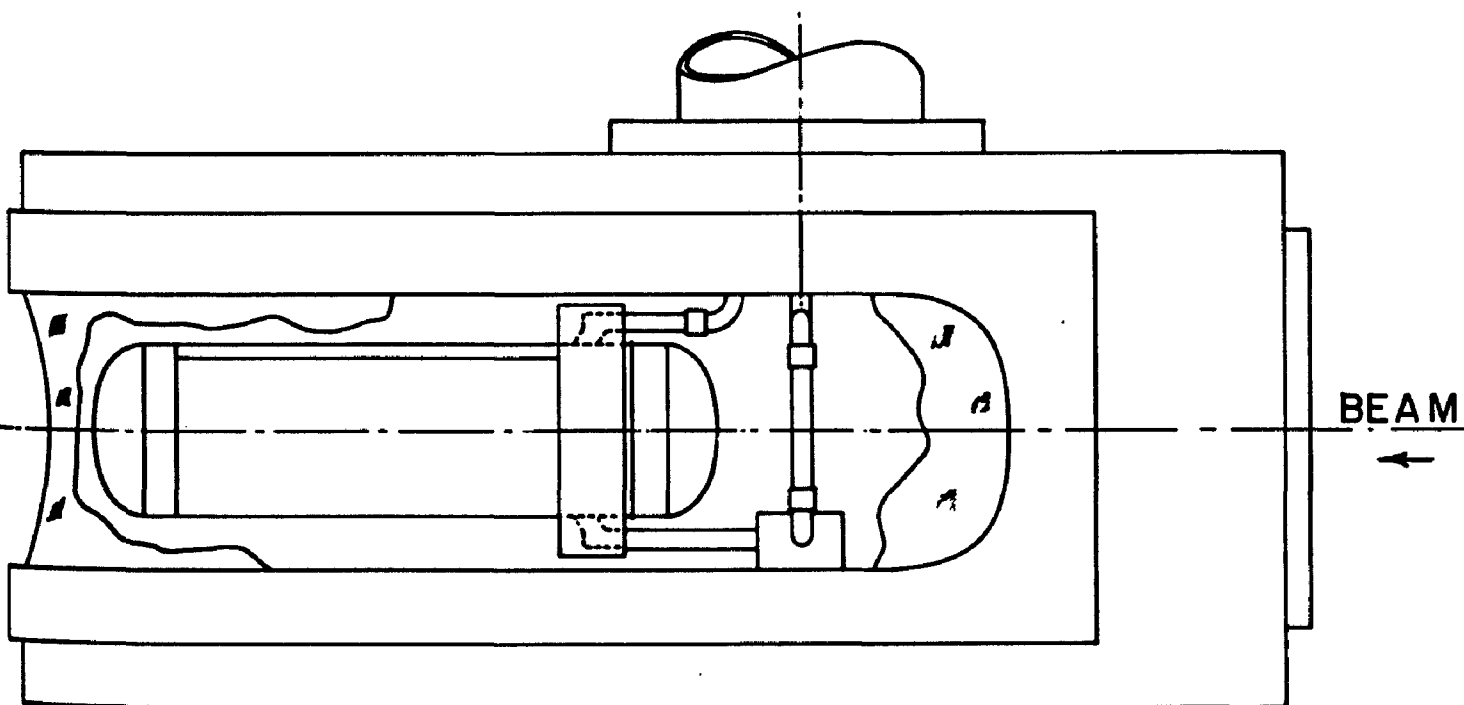
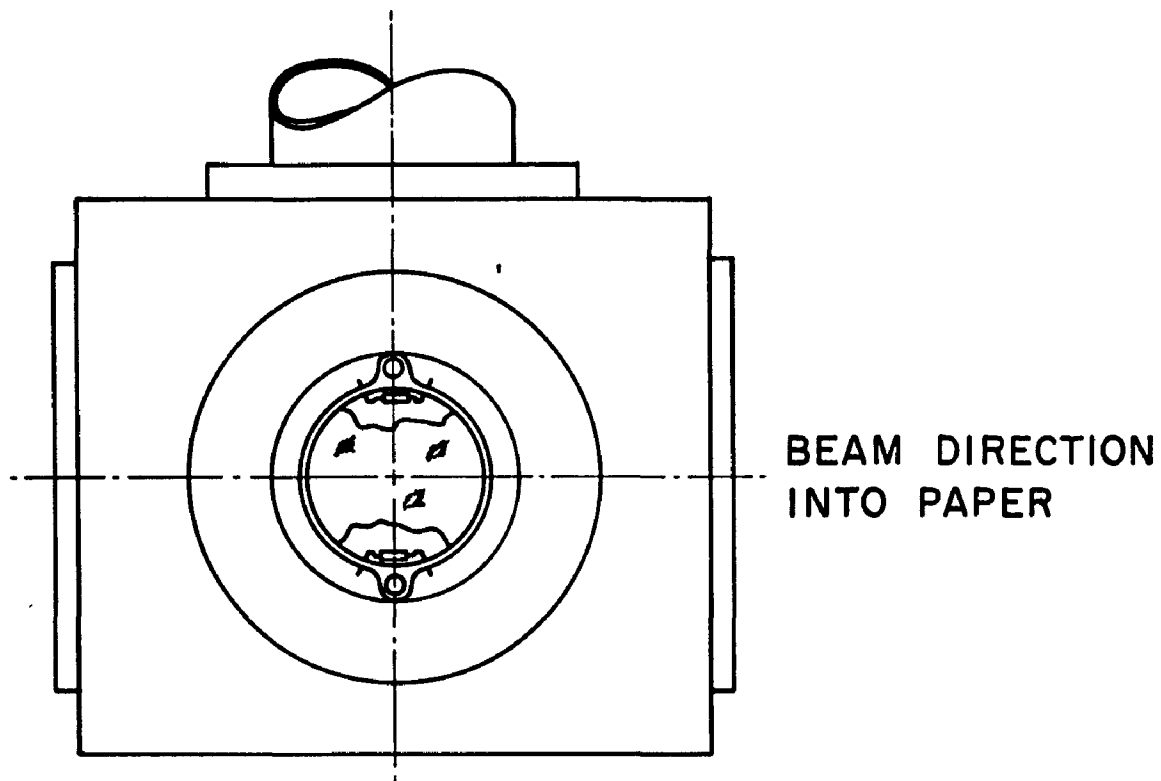
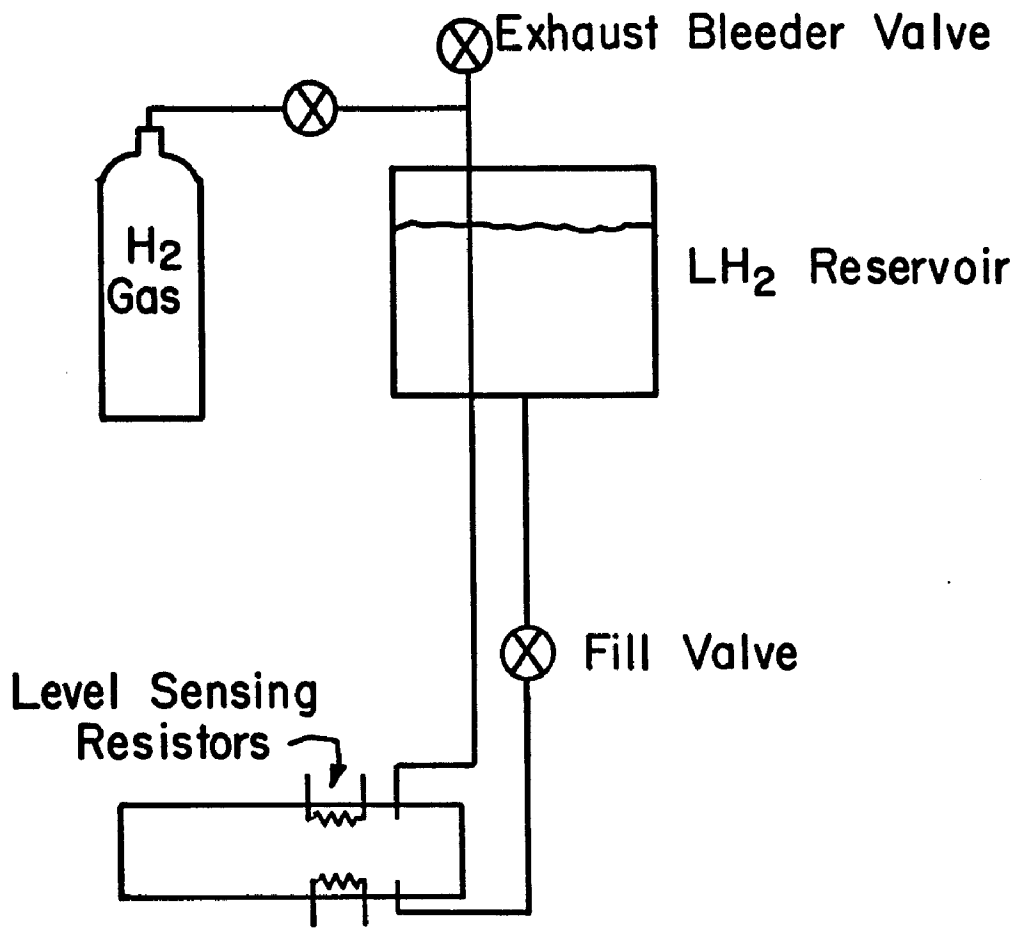
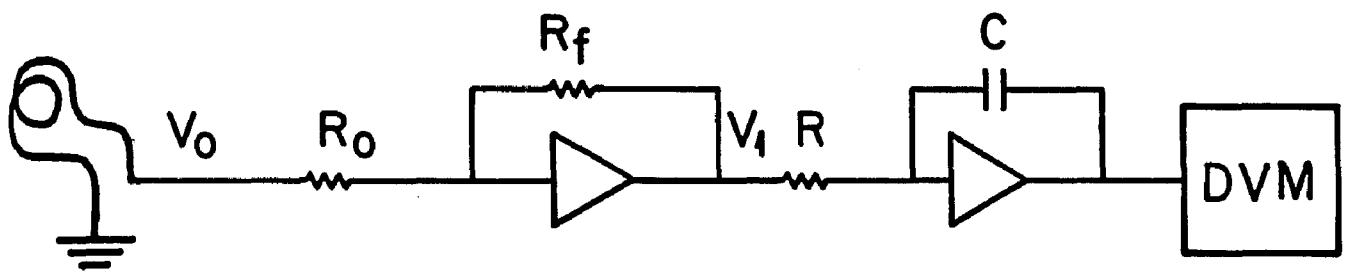


Figure 10



- Figure 11



$$R = 100 \text{ k}\Omega$$
$$C = 8 \mu\text{f}$$

Figure 12

INCHES

INCHES

	-3.5	-3	-2	-1	0	1	2	3	3.5		-3.5	-3	-2	-1	0	1	2	3	3.5
+7.5	24	46	60	10	-31	26	102	102	68	+7.5	78	91	11	-65	7.6	66	65	42	
7	18	29	37	12	-7.6	23	66	68	51	7	22	31	36	2.5	4.3	34	47	44	29
6										6	5.4	6.1	11		12				
5	2.9	4.3		9.4		16		19	16	5	.36	-.72	4.0	4.0	4.0	0.0	0.0	-.72	
4										4									
3	-2.5	-1.8	4.7	6.9	6.1	3.6				3	-1.4	-.36	2.2	1.8	-1.8	-3.2	-4.7		
2										2									
1	-2.9	-2.5	1.8	1.8	.72	1.8				1	-1.4	-2.5	.36	-.36	-4.0	-6.1	-9.0		
0	-4.0	-3.6	-1.8	-.72	0.0	-.36	-2.5	-3.2	-4.7	0									
-1	-4.0	-4.3	-1.1	.36	0.0	-.36	-3.2	-6.1	-9.0	-1	2.5	2.5	4.7	4.0	-2.5	-5.4			
-2	-2.9	-1.8	.36	1.4	1.8	-.36	-3.2	-6.1	-9.0	-2									
-3	-1.1	0.0	1.8	3.2	2.5	2.2	-1.8	-6.1	-9.4	-3	10	11	12	8.7	3.2	.36			
-4	2.5	3.6	6.1	6.9	4.7	3.2	36	-4.7	-7.6	-4									
-5	10	12	14	13	9.7	6.9	5.0	-.72	-4.7	-5	30	44	49	22	1.1	17	34		
-6	21	24	25	19	12	11	11	4.0		-6	99	110	25	-55	18	70			
-7	34	46	49	26	6.1	16	23			-7									
-8	59	95	103	27	-36	15	53			-8									

Left

Right

Figure 13

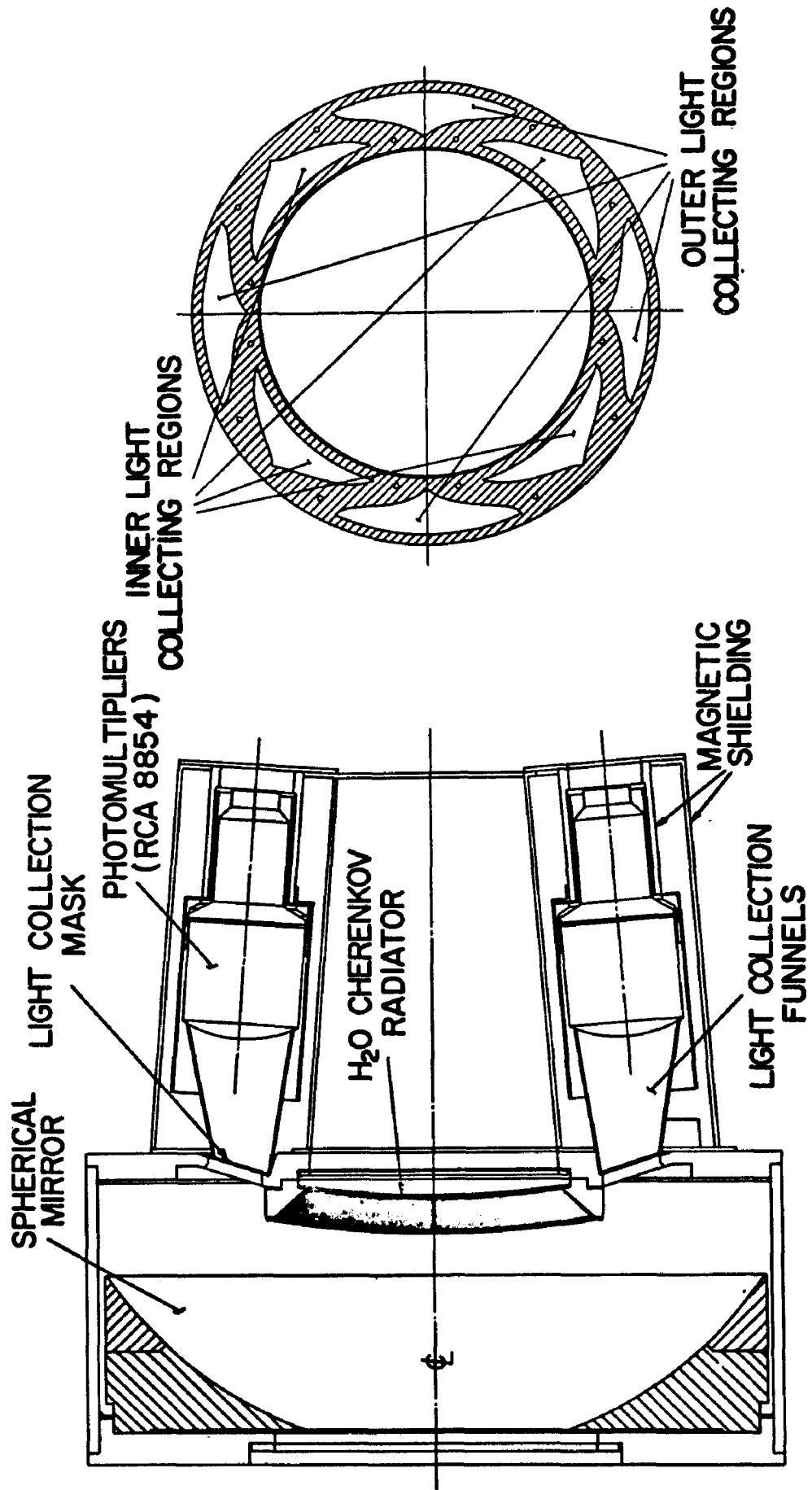


Figure 14

RATIO (Δ) vs. MOMENTUM FOR H₂O ČERENKOV

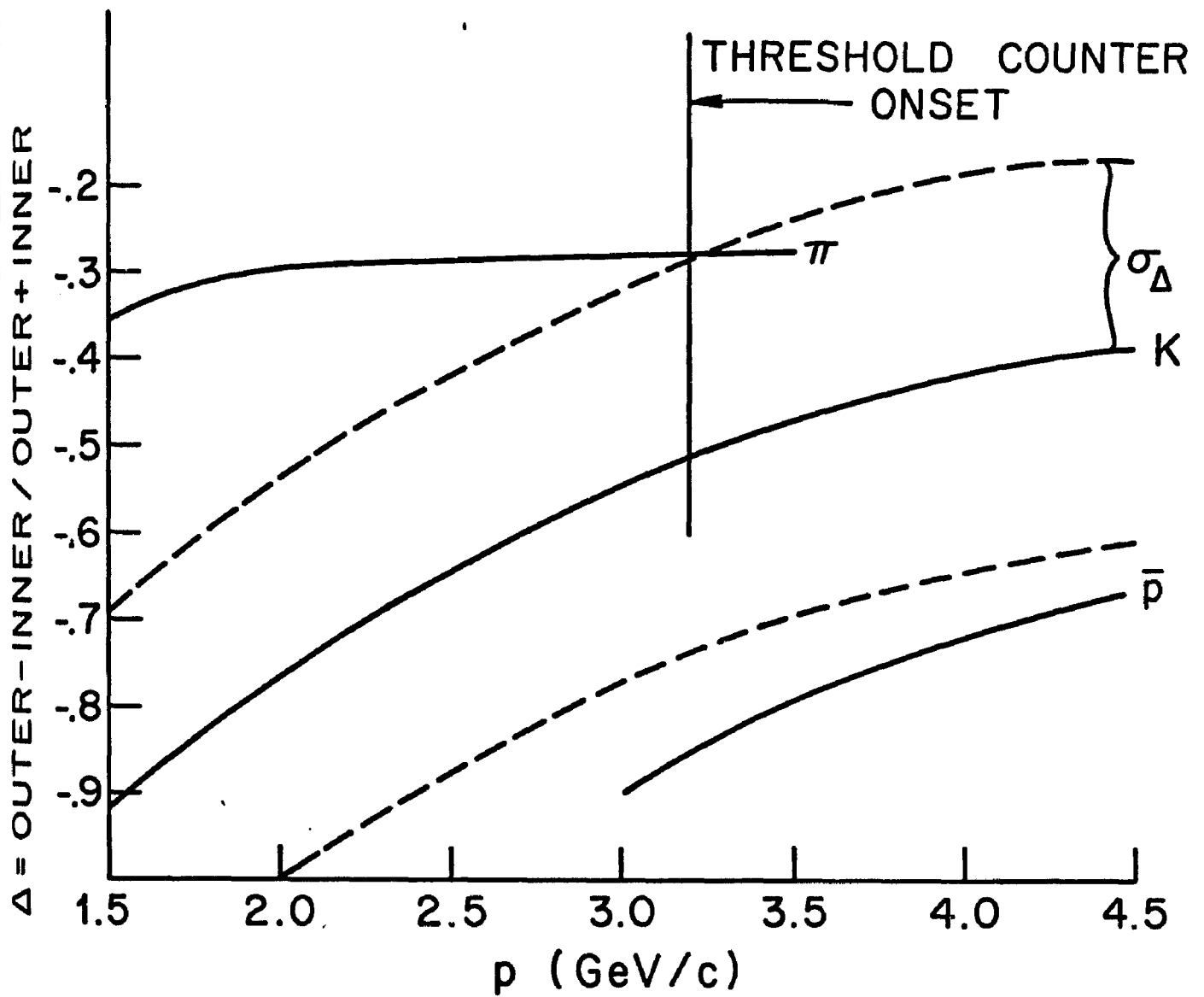
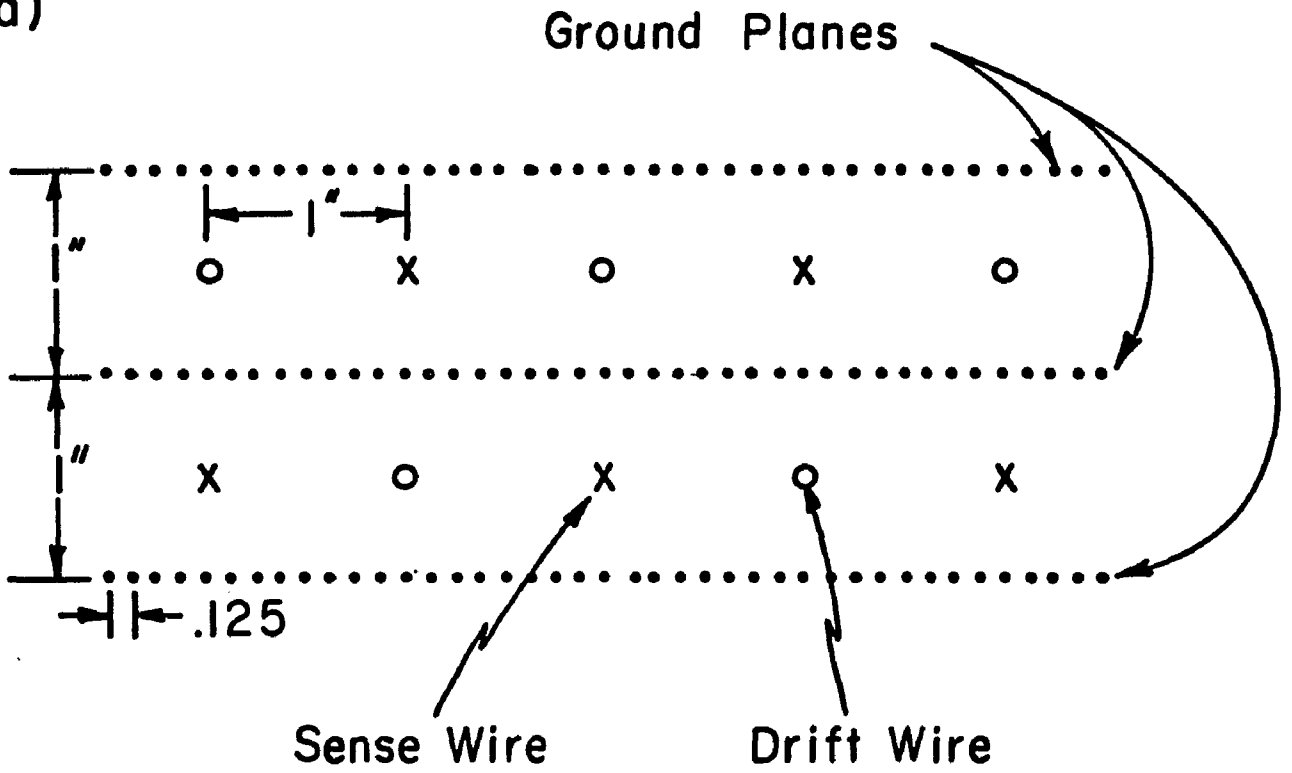


Figure 15

(a)



(b)

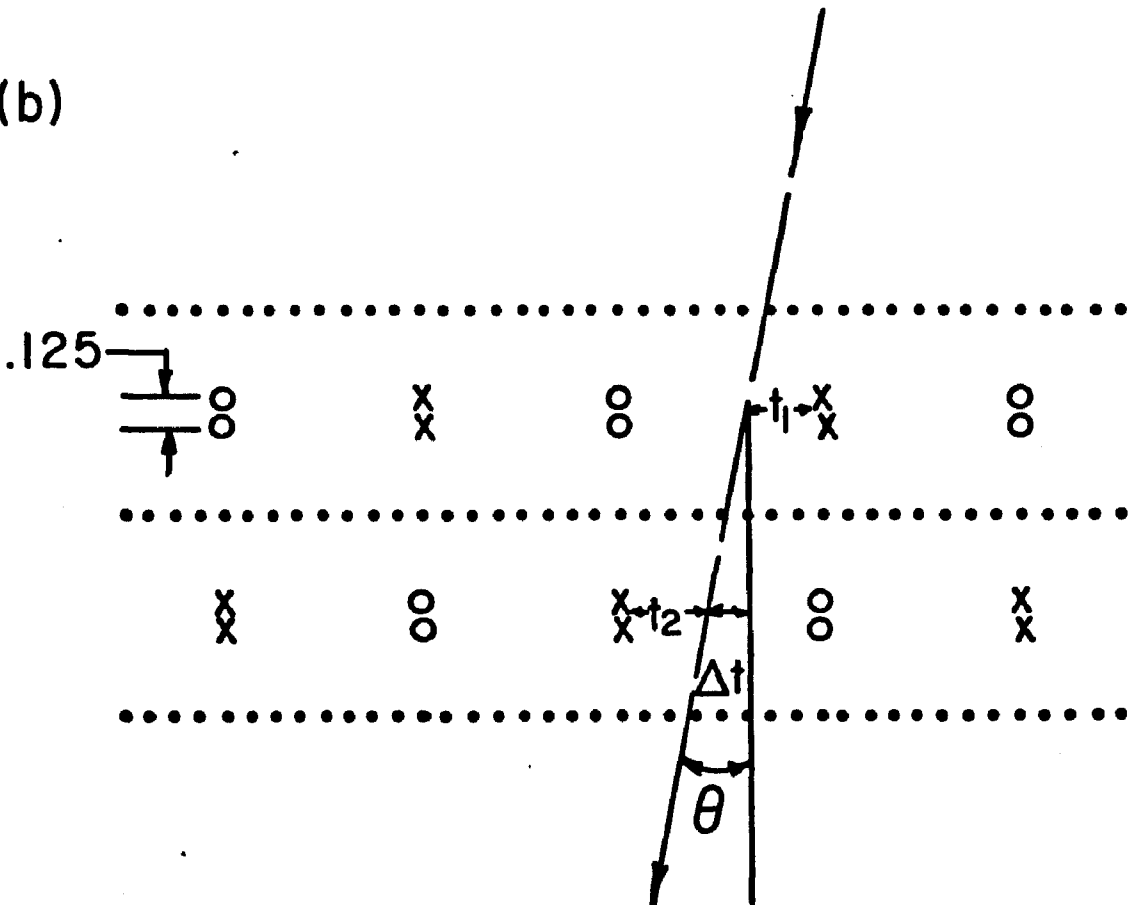
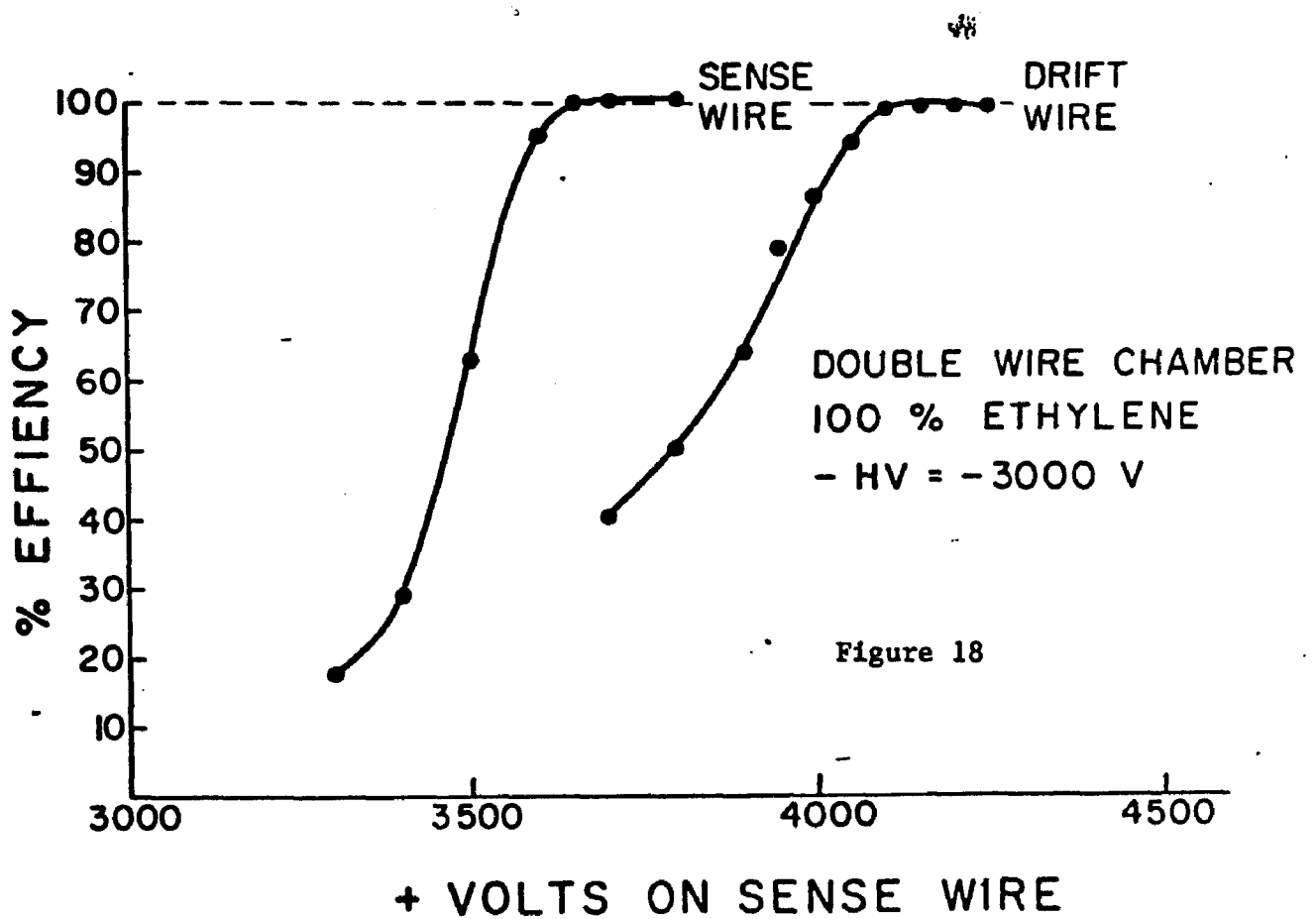
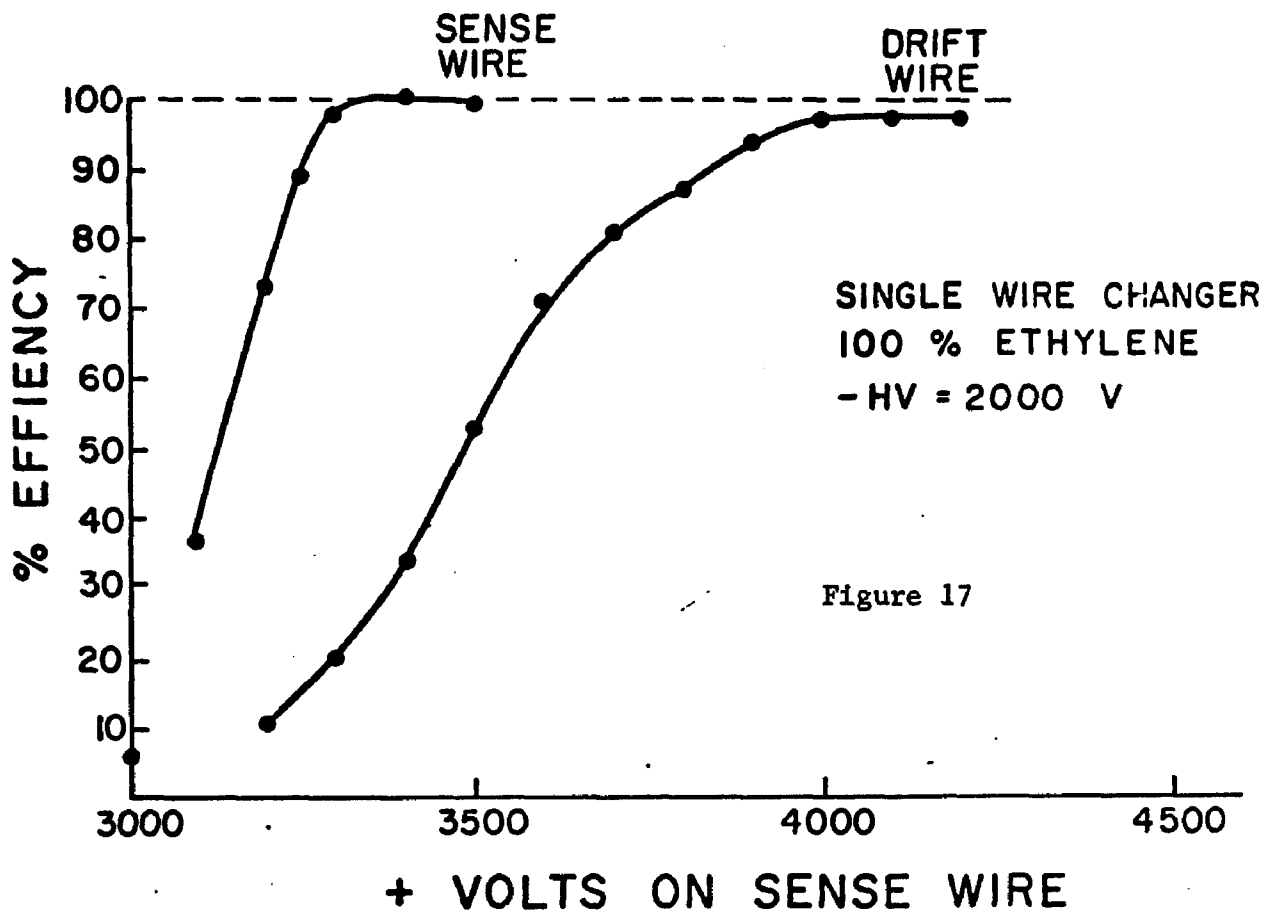


Figure 16



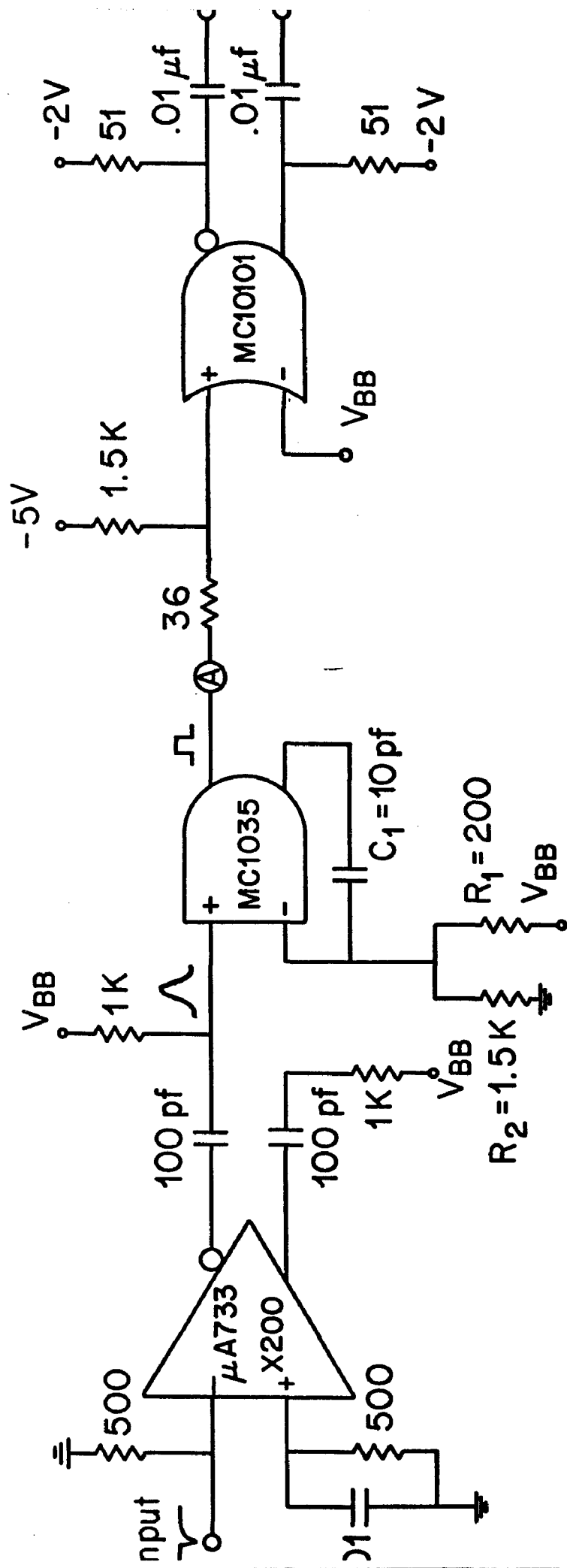


Figure 19

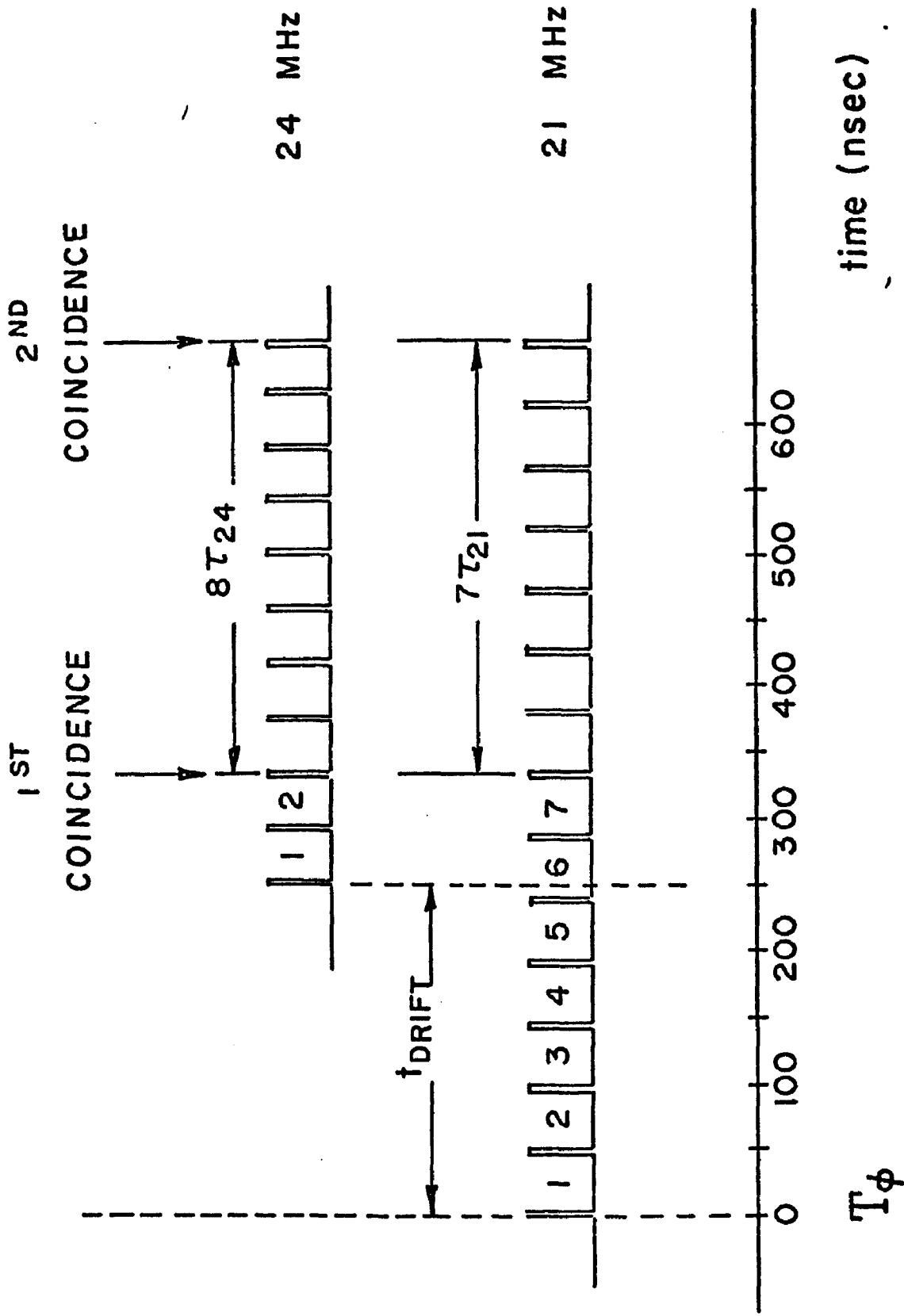


Figure 20

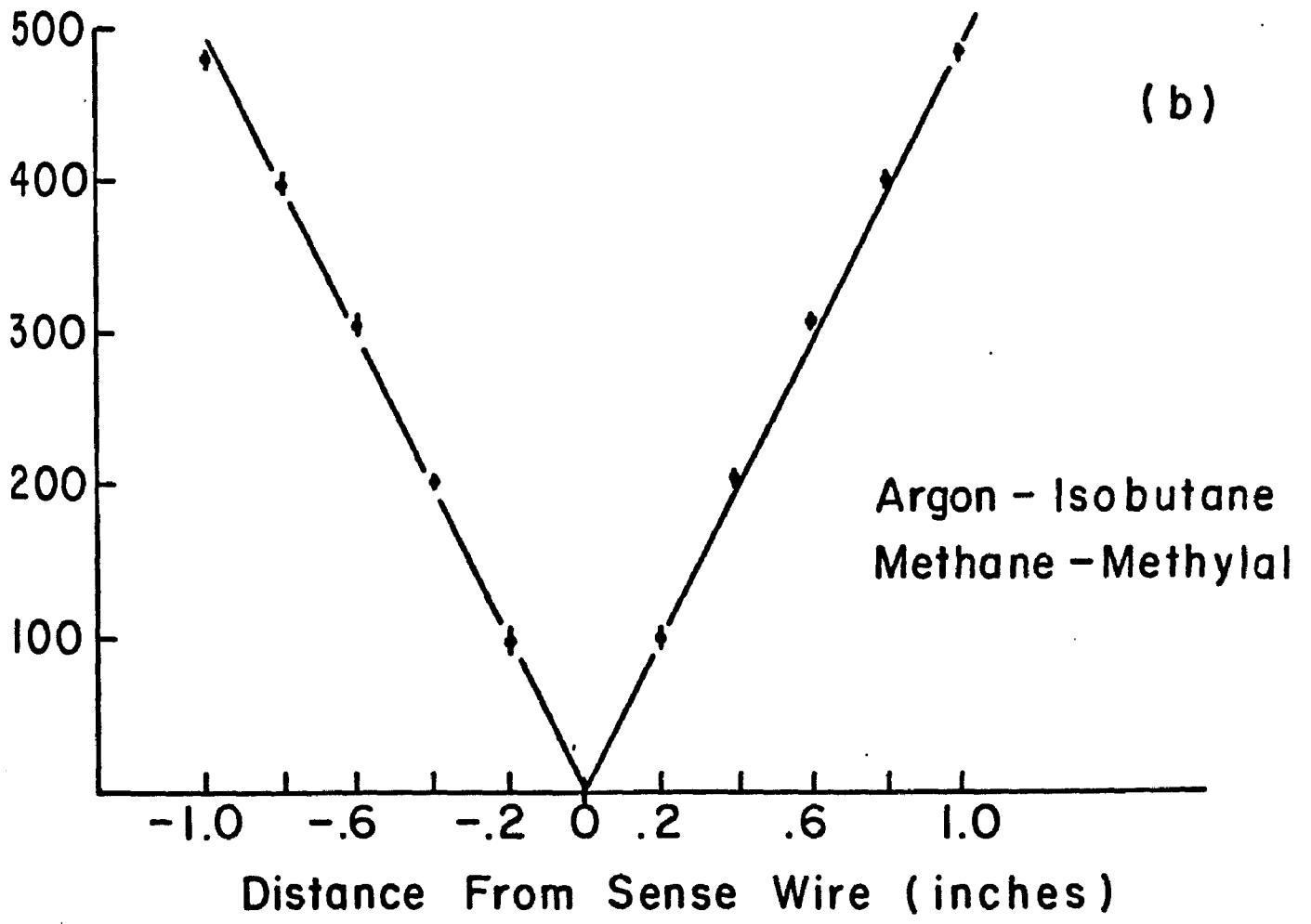
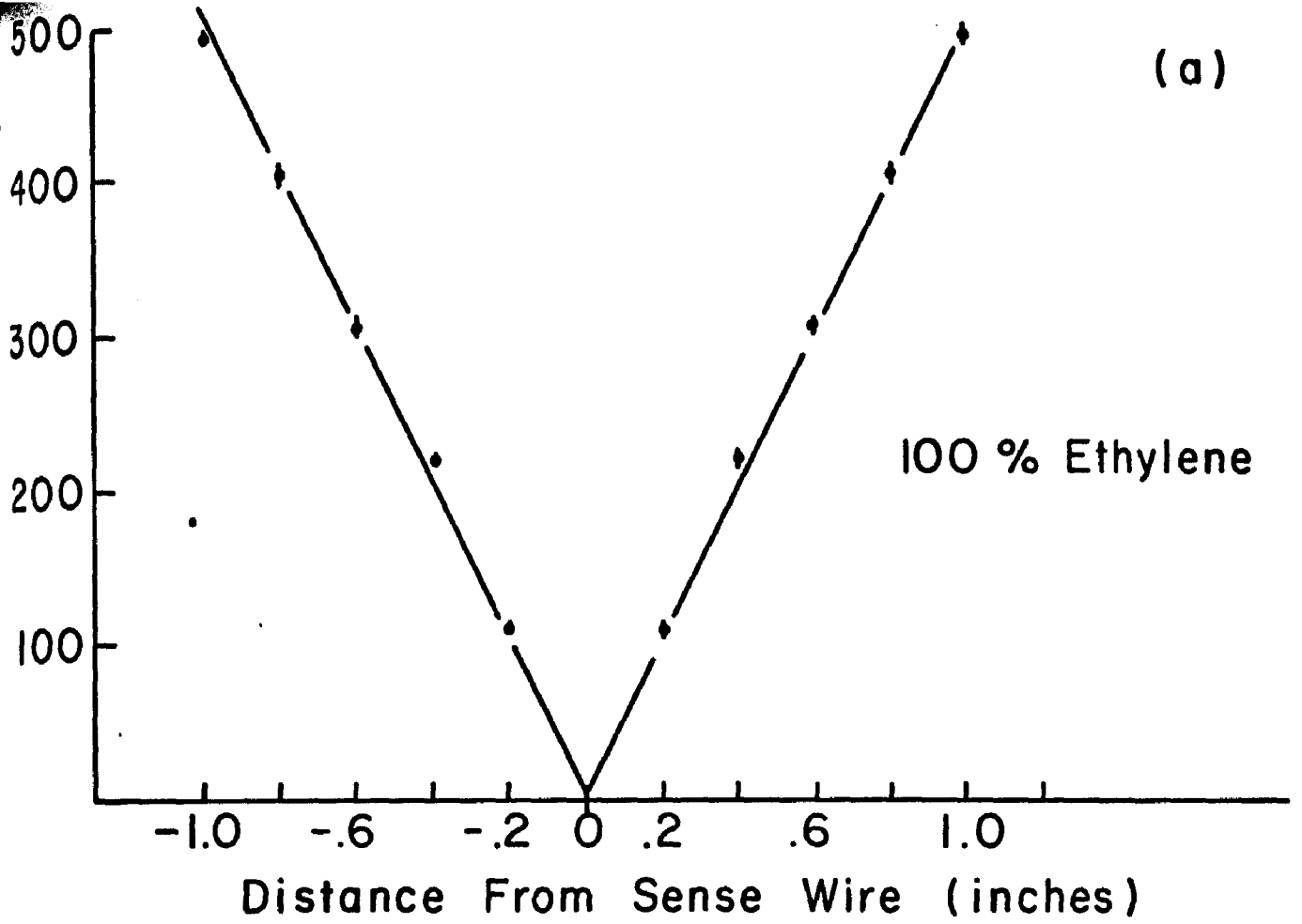


Figure 21

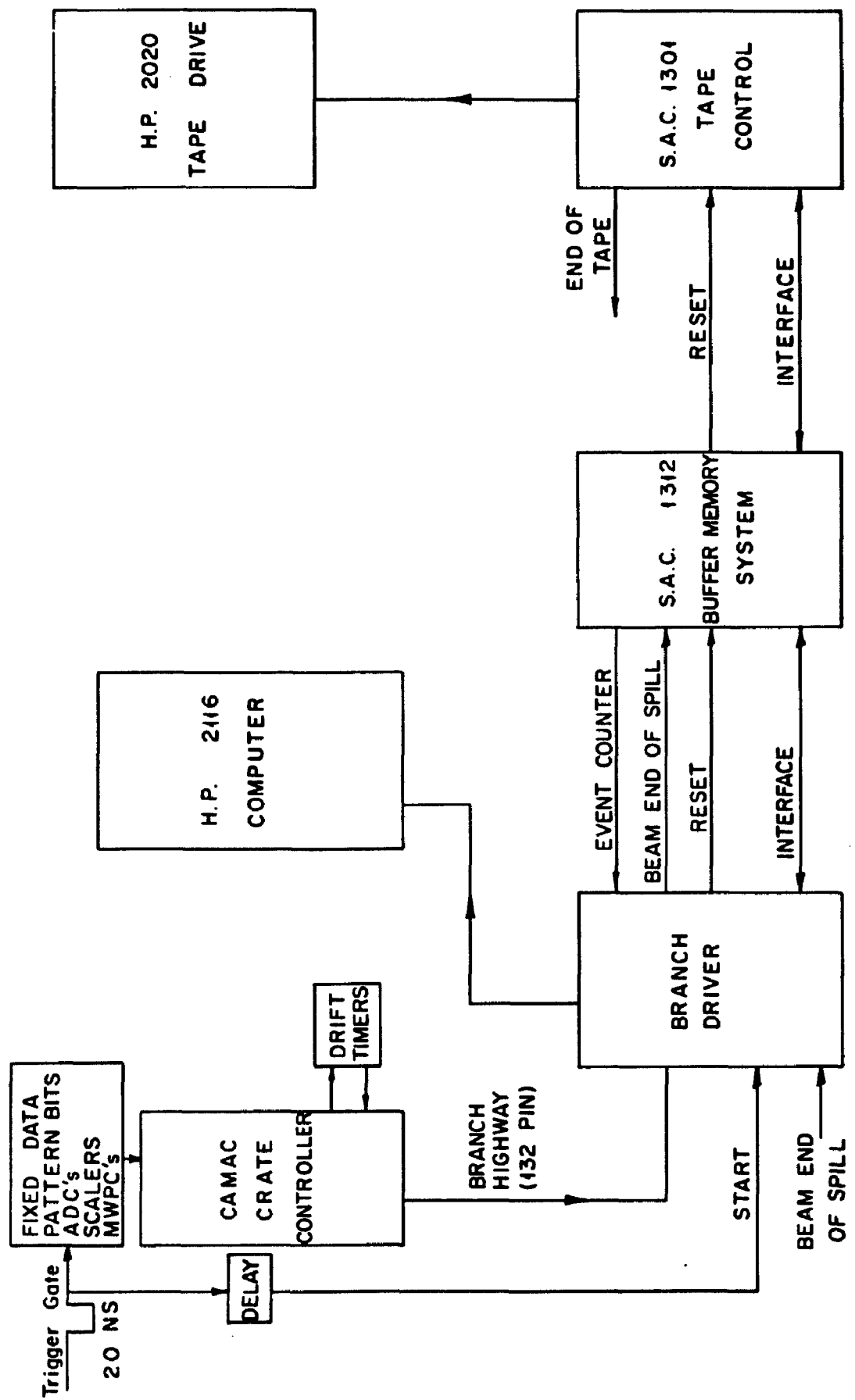
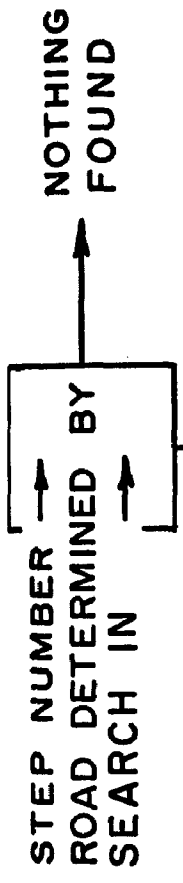


Figure 22



KEY:

- ϕ : MAGNET CENTER LINE
- T : TARGET
- , : ROAD DETERMINED BY T AND / OR LINE IN CHAMBER AND / OR ϕ
- : ROAD DETERMINED BY LINE IN CHAMBER BUT MUST OVERLAP ROAD TO T

Figure 23

Pion Center Determination

Water Counter RATIO

Left Arm

— Cuts —

Theshold Counter > 3.5

Momentum > 3.2 GeV/c

Charge = Minus

200

150

100

50

-1

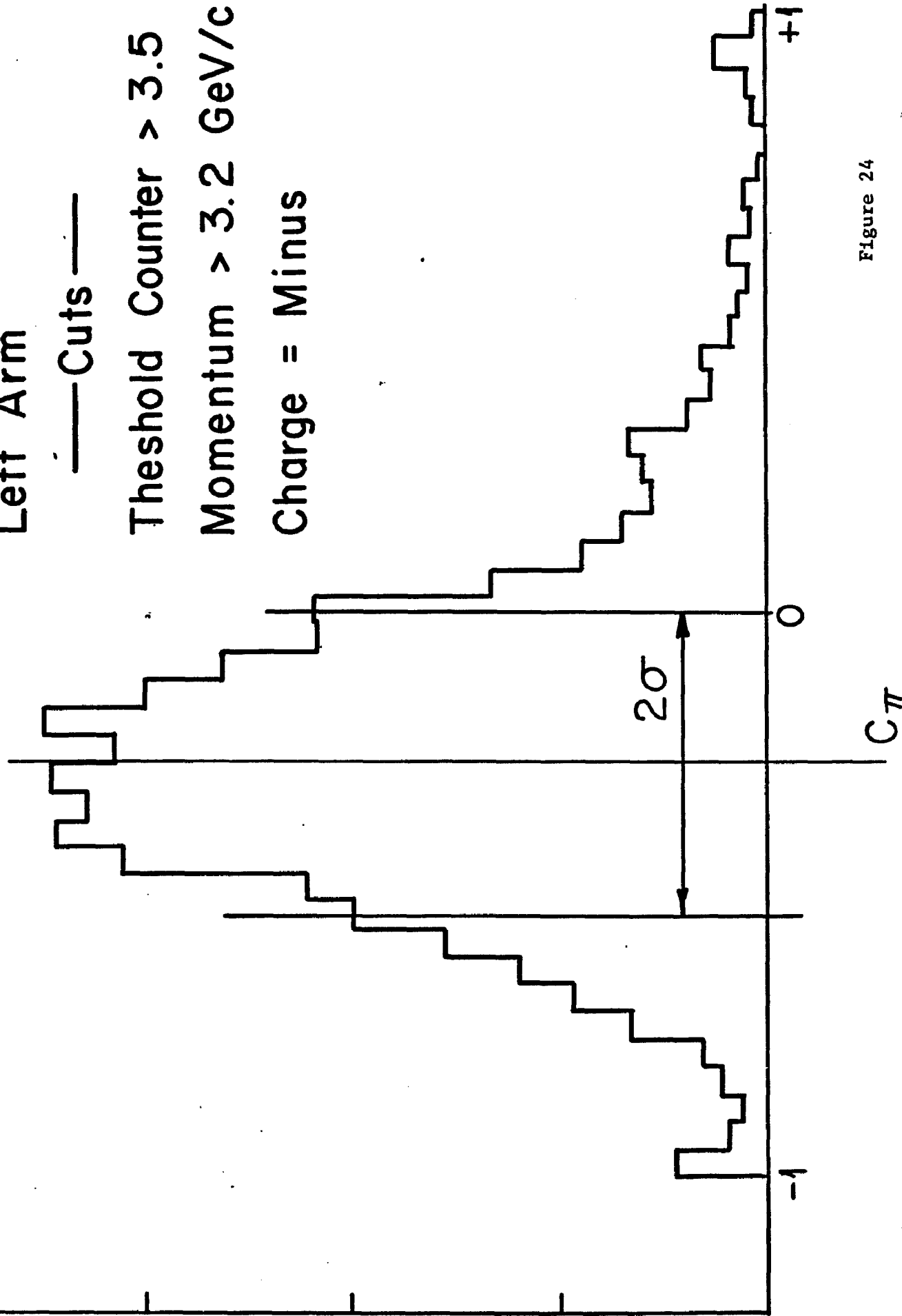
0

+1

2σ

$C\pi$

Figure 24



Sum Cut Determination

Water Counter SUM
Left Arm

—Cuts—

Theshold Counter > 3.5
Momentum > 3.2 GeV/c

300

200

100

0

50

100

150

200

Csum

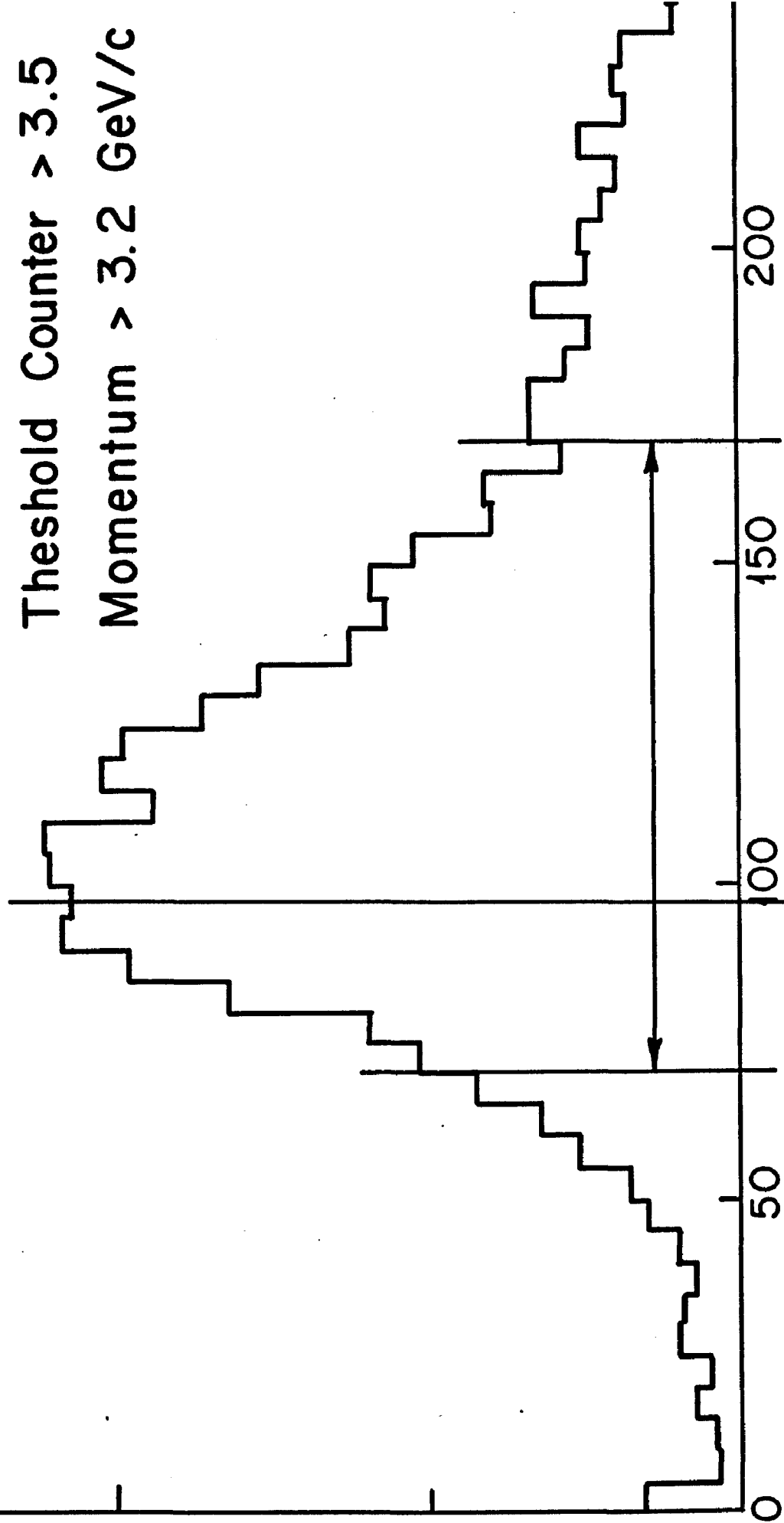


Figure 25

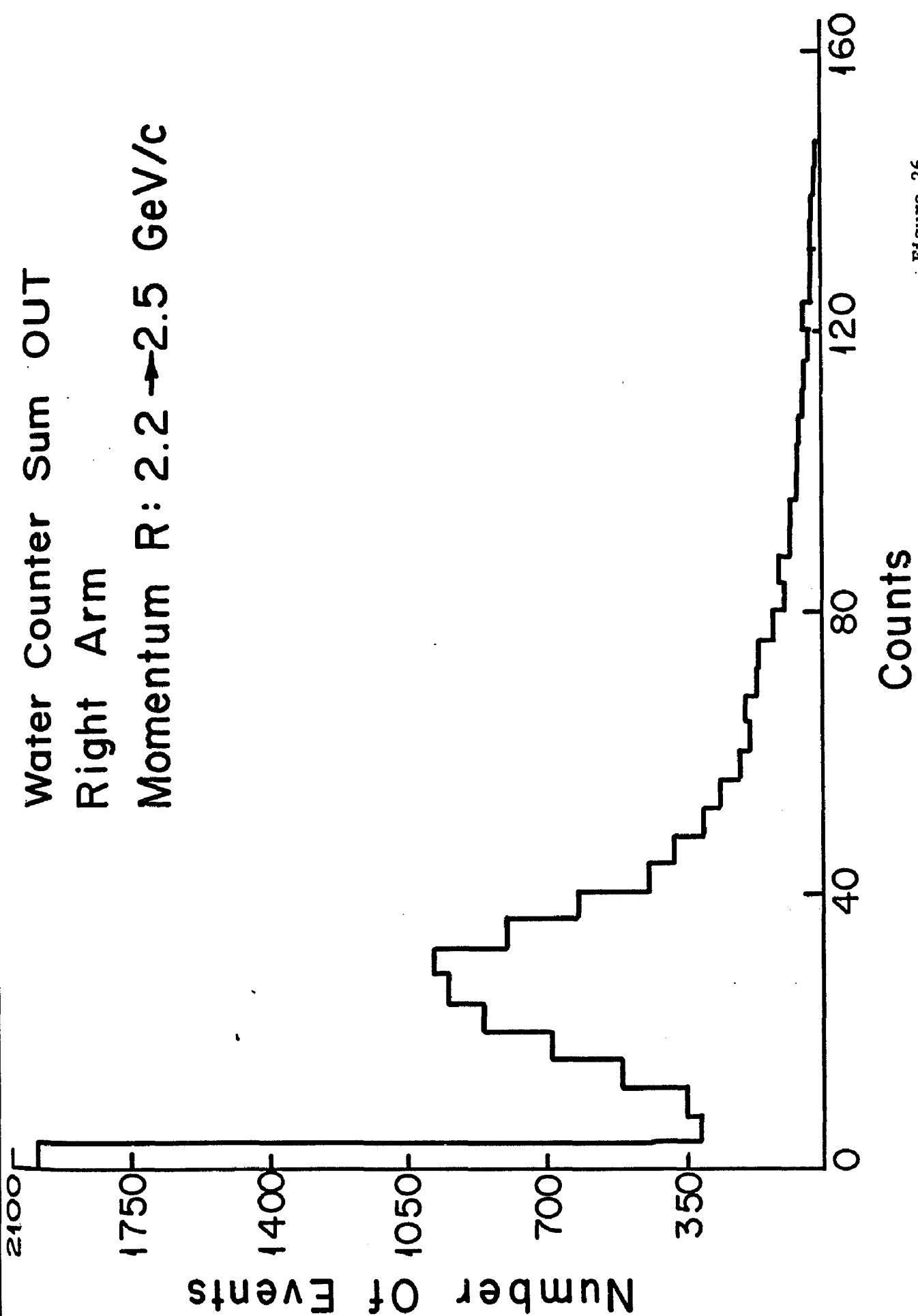
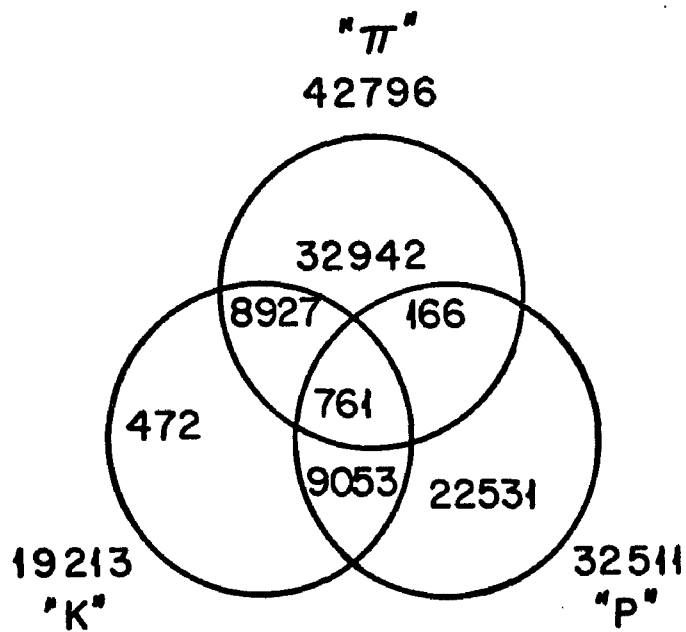


Figure 26



74852 - Total Identified
 Target Full
 Magnet Polarity A, Right Arm
 45345 - Not Identifiable

P_1 - Right Arm

π^+

Vertex $\pm 1''$ Of Target Center

TAN LAB .312 $- .335$

(17.2°) $- 18.8^\circ$)

Central Bin

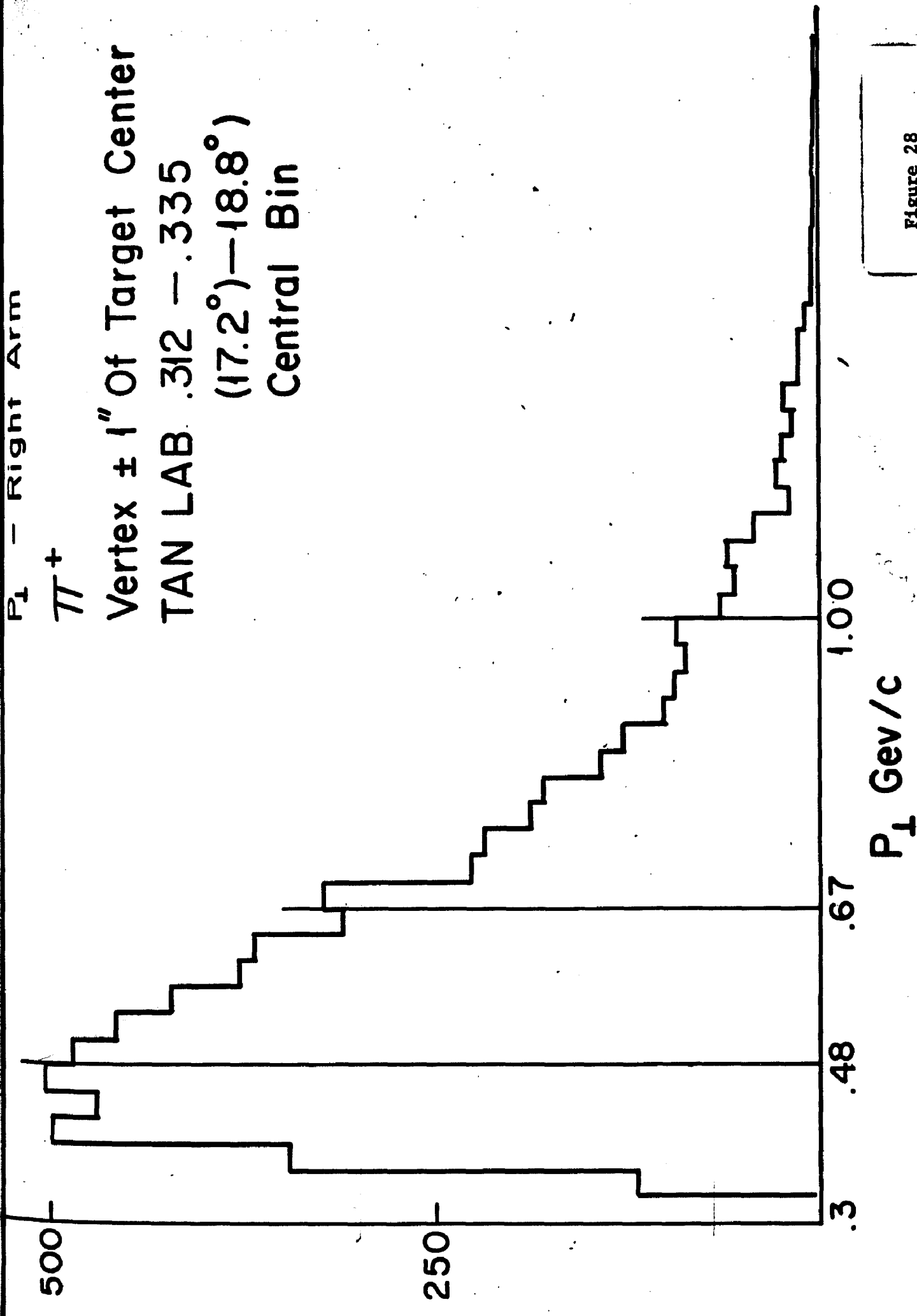


Figure 28

PLEASE NOTE;

Thesis is tightly bound.
Some print lost in spine.
Filmed in the best
possible way.

UNIVERSITY MICROFILMS.

WATER COUNTER SUM RIGHT

Opposite Arm

Vertex LY

RATIO R \rightarrow .7 \rightarrow -.05

From 103676 Left Triggers

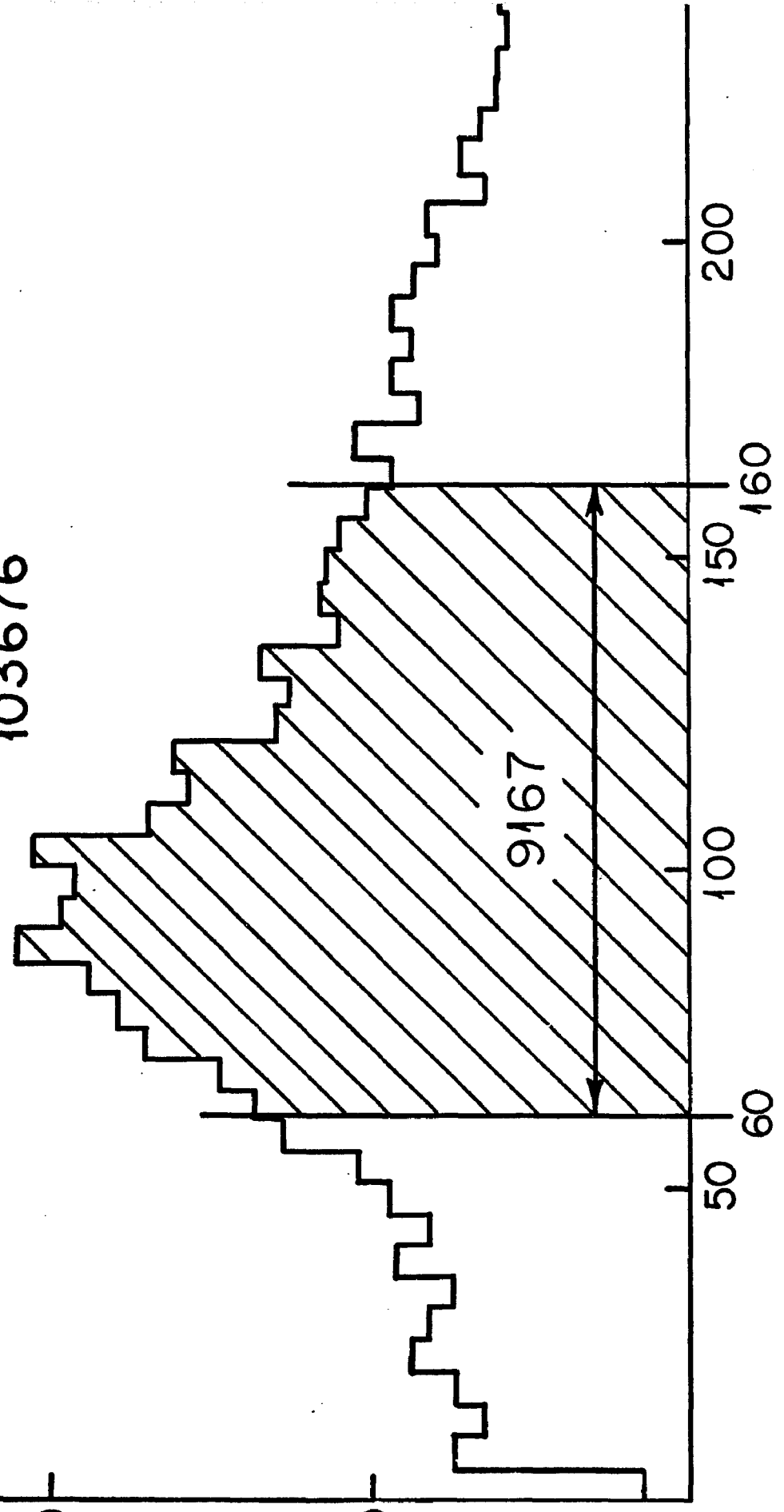
$$\frac{9167}{103676} = .088$$

900

600

600

Number Of Events



Counts

Figure 29

Cuts
Sum Left 70 - 170
Track in R.H. Arm

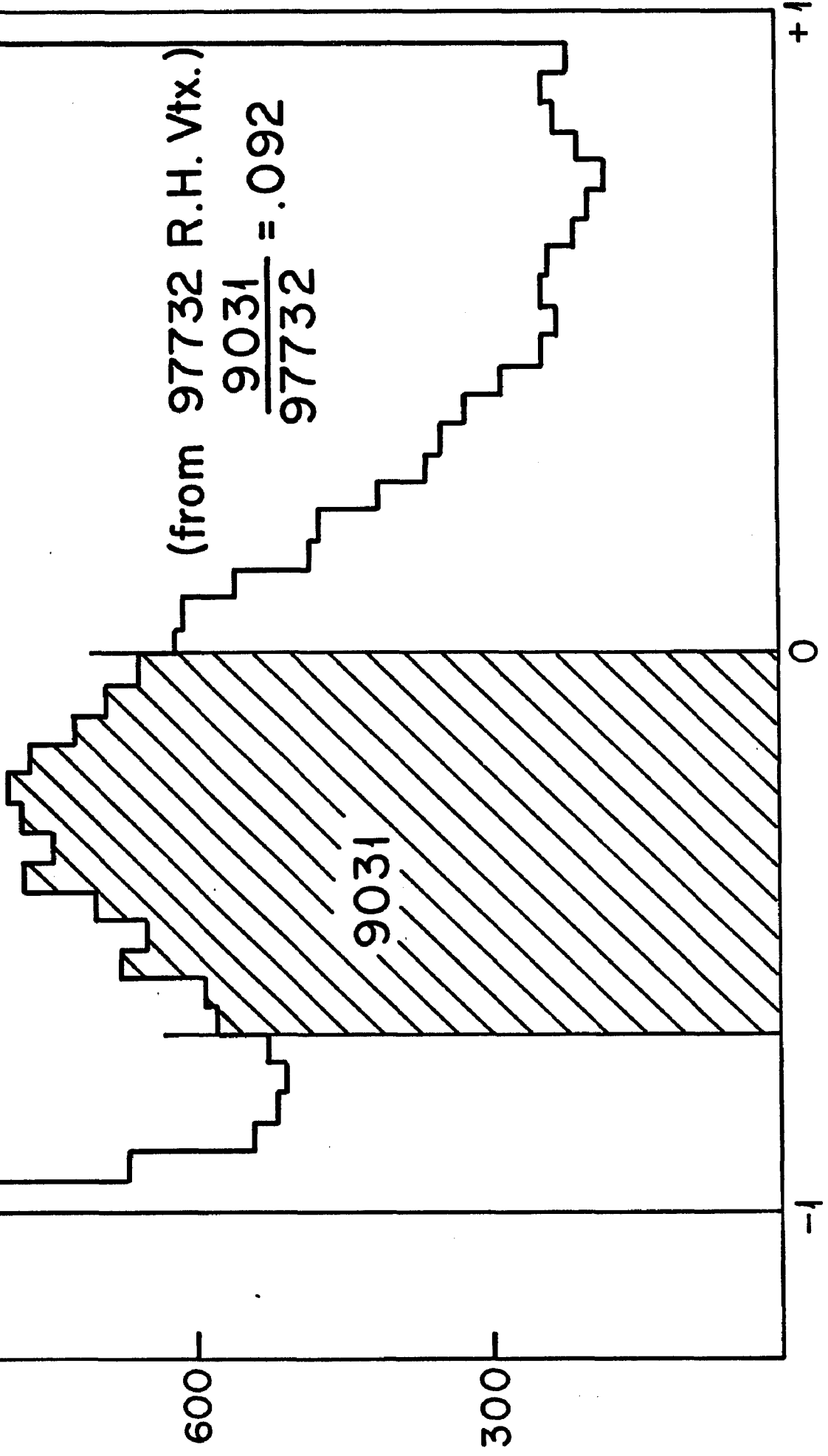


Figure 30

H2O SUM Left

Track in Right Arm
No Cuts

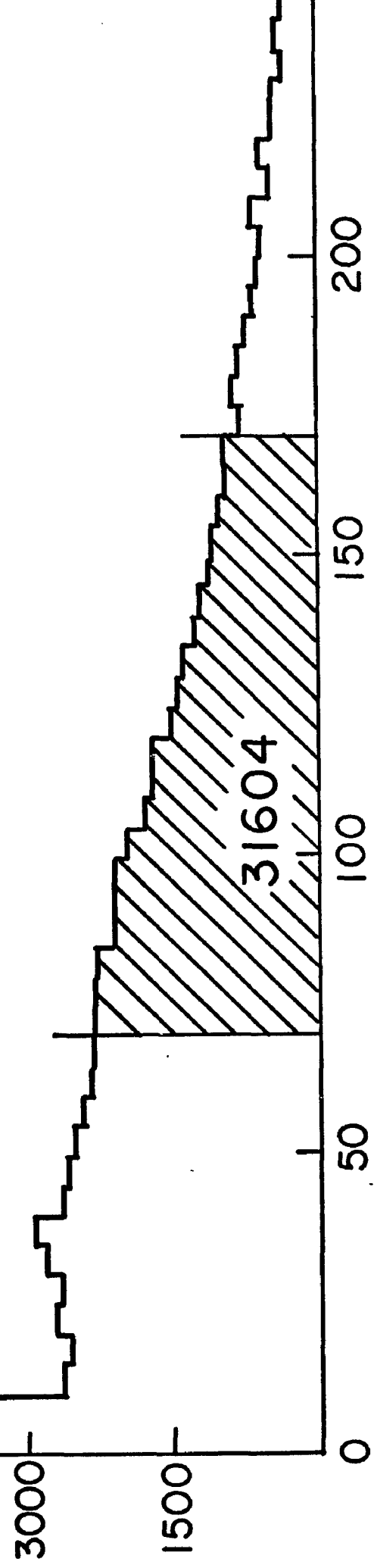
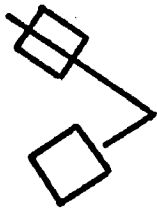


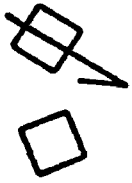
Figure 31

3000

2000

1000

0



H₂O SUM Right

Track in Right Arm
No Cuts

$$\frac{23596}{31604} = .75$$

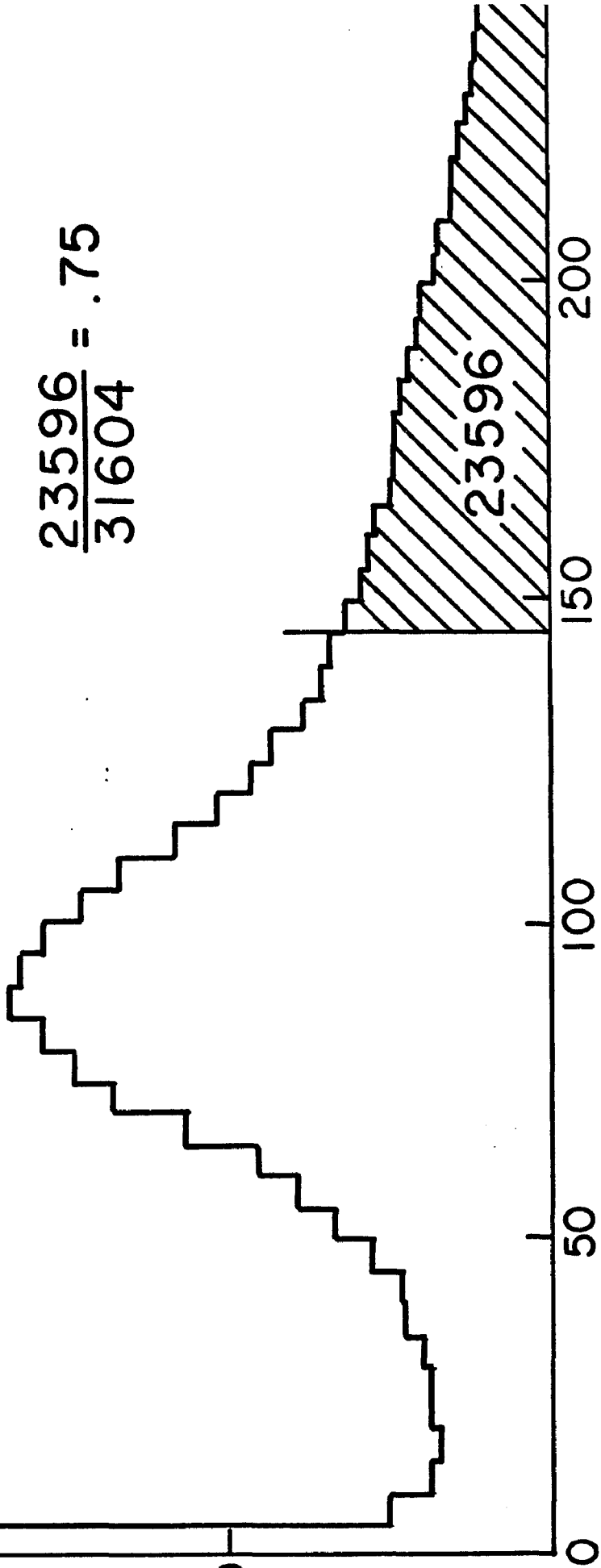


Figure 32

Water Counter SUM
Right Arm
—Cuts—
Momentum R 1.8 → 2.1 GeV/c
Vertex R ± 1" of Target Center
RATIO R -1.2 → .75

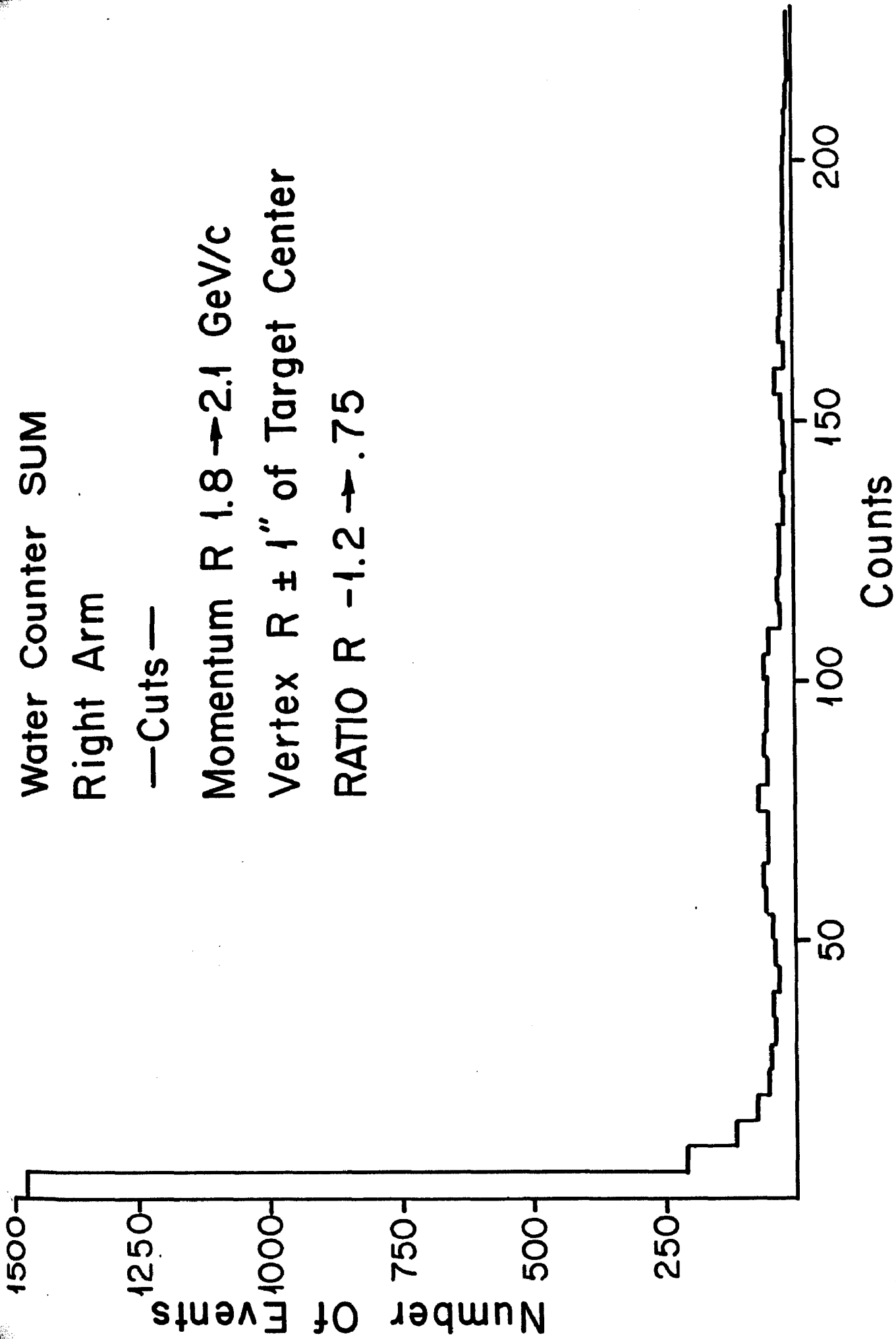


Figure 33

Water Counter SUM

Right Arm

—Cuts—

Track In Left Arm

Vertex Left $\pm 1''$ Of Target Center

RATIO R: $-.7 \rightarrow -.05$

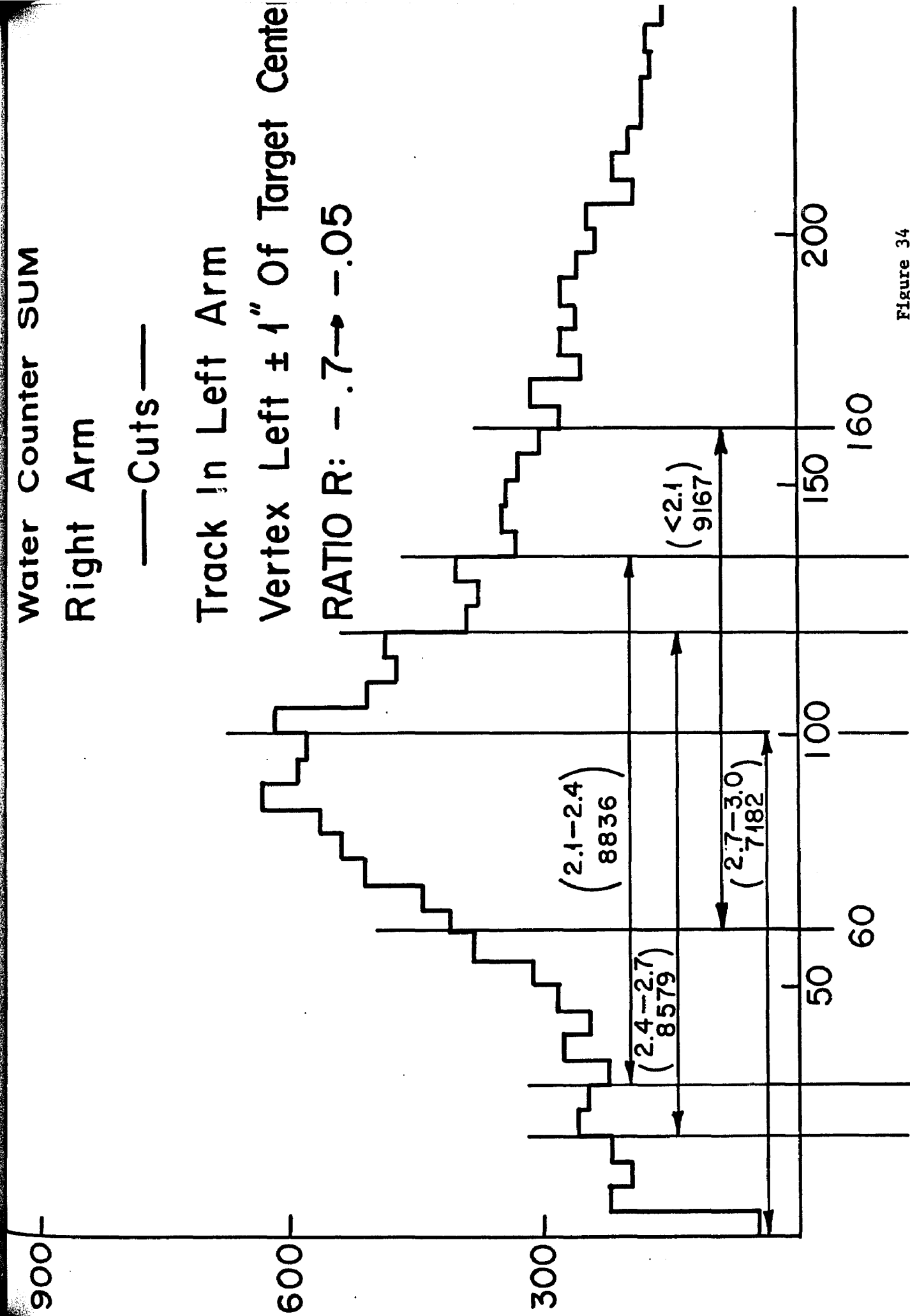


Figure 34

Water Counter SUM

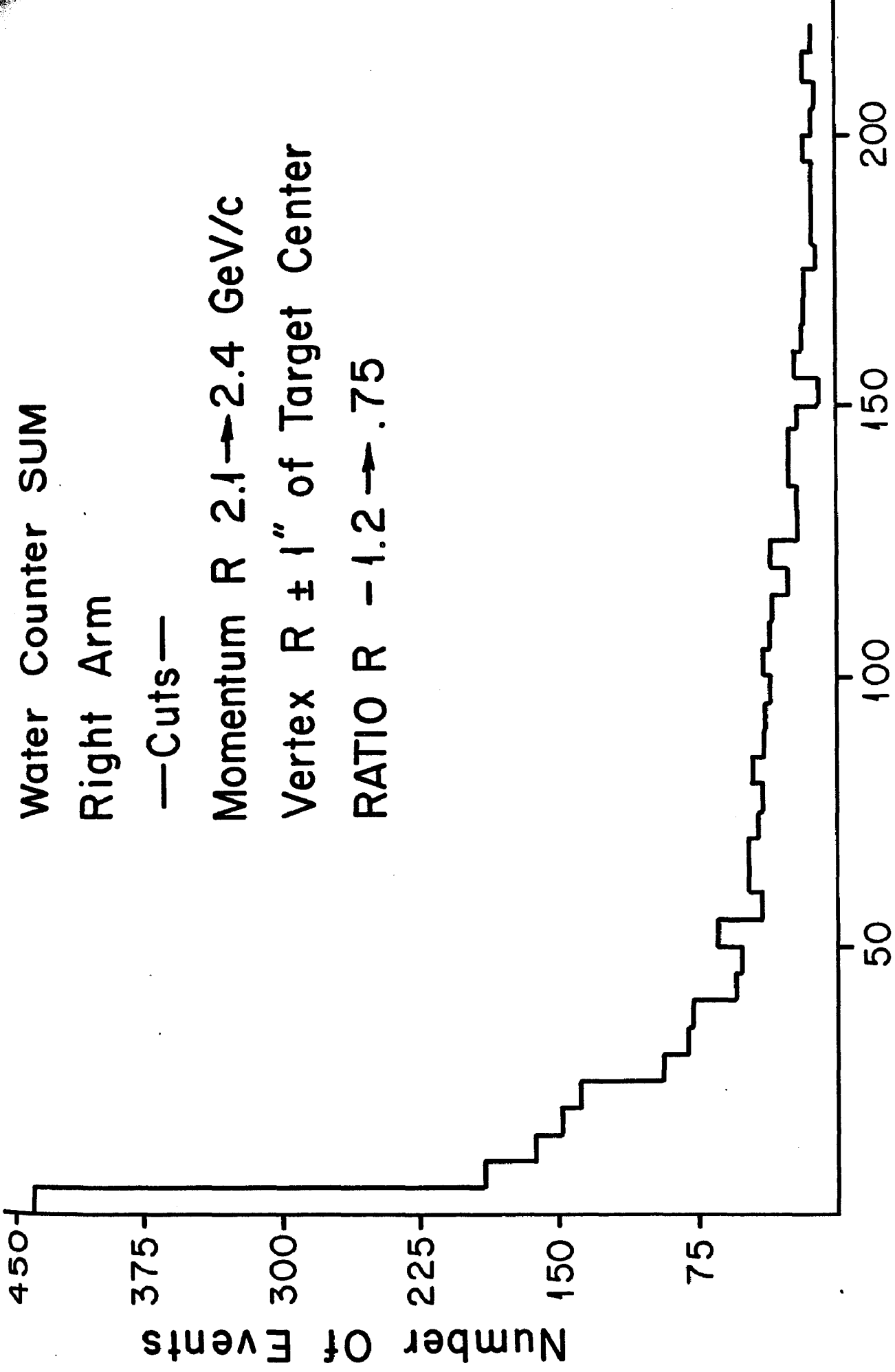
Right Arm

—Cuts—

Momentum R $2.1 \rightarrow 2.4$ GeV/c

Vertex R $\pm 1''$ of Target Center

RATIO R $-1.2 \rightarrow .75$



Counts

Figure 35

Water Counter SUM

Right Arm

—Cuts—

Momentum R $2.4 \rightarrow 2.7$ GeV/c
Vertex $R \pm 1''$ of Target Center
RATIO $R-1.2 \rightarrow -.75$

120

100

Number Of Events

80

60

40

20

50

100

150

200

Counts

Figure 36

Water Counter SUM Right

Same Arm

Vertex RY

Momentum R 2.7 → 3.0 GeV/c

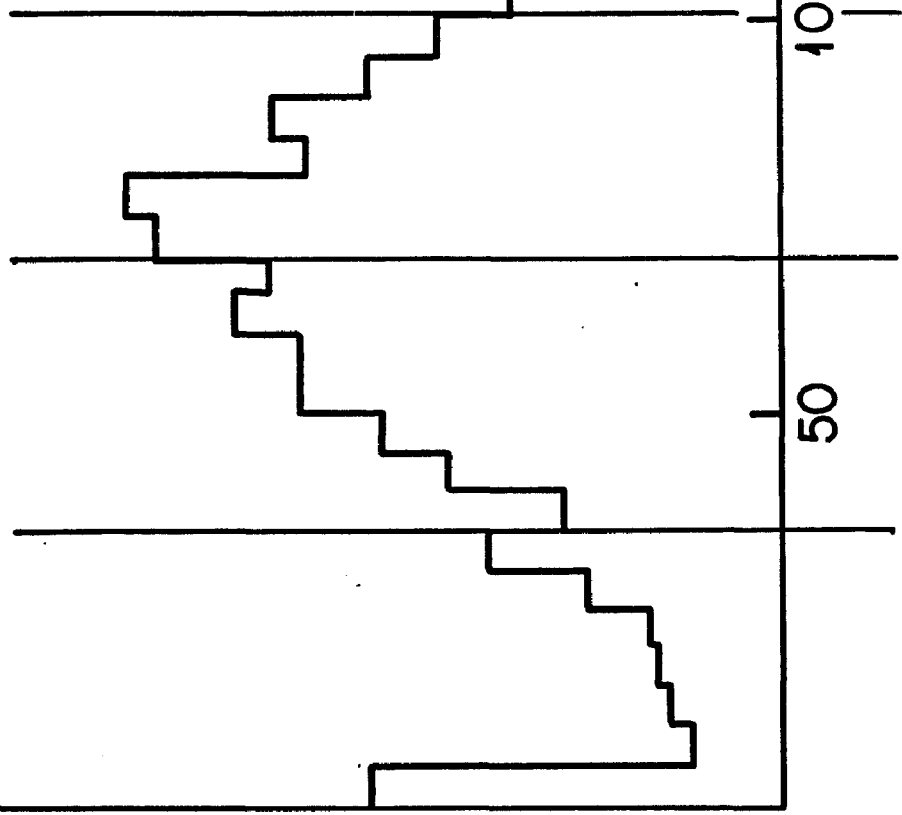
RATIO R-1.2 → -.75

120

Number Of Events

80

40



50

100

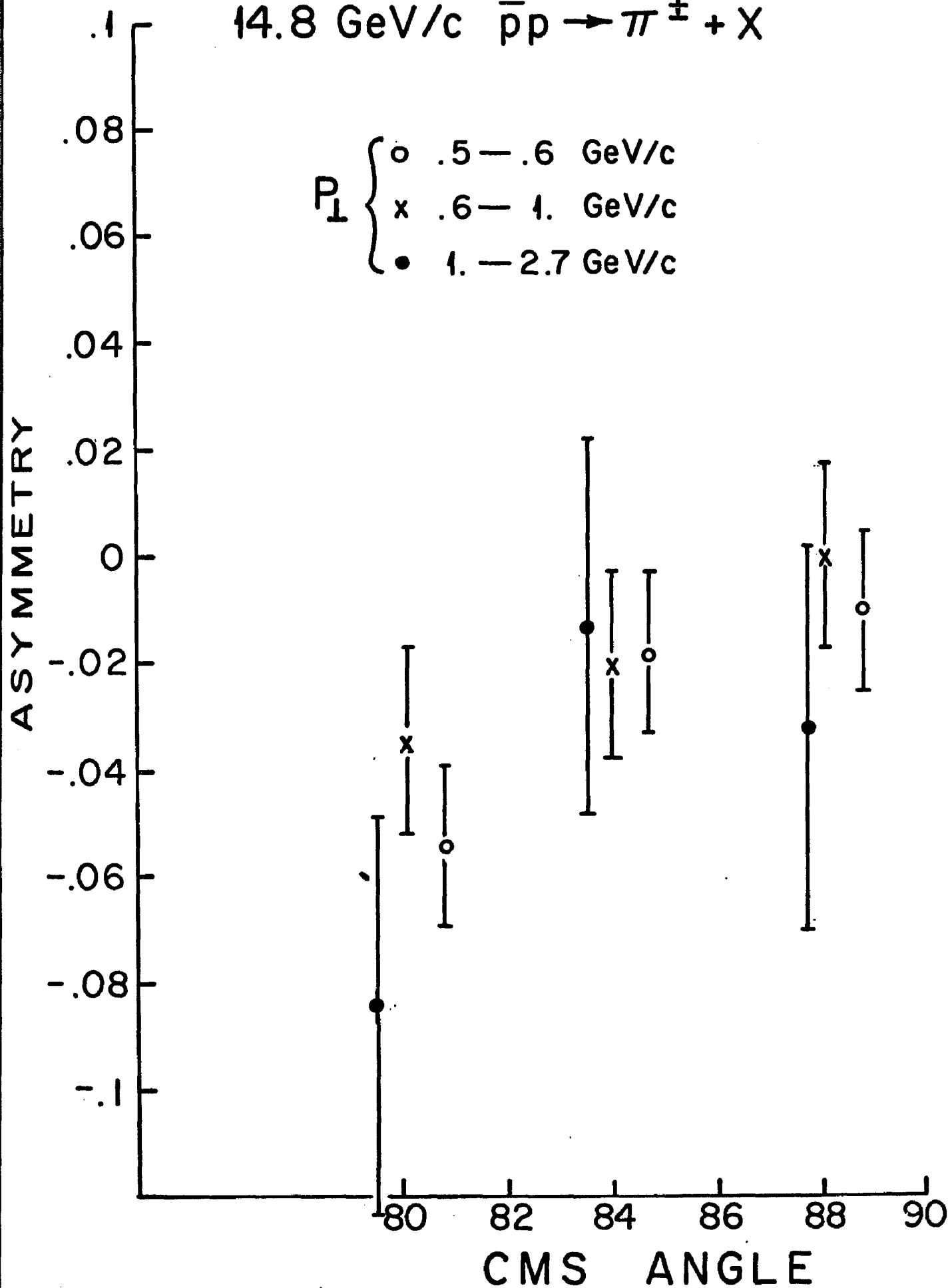
150

500

Counts

Figure 37

14.8 GeV/c $\bar{p}p \rightarrow \pi^\pm + X$



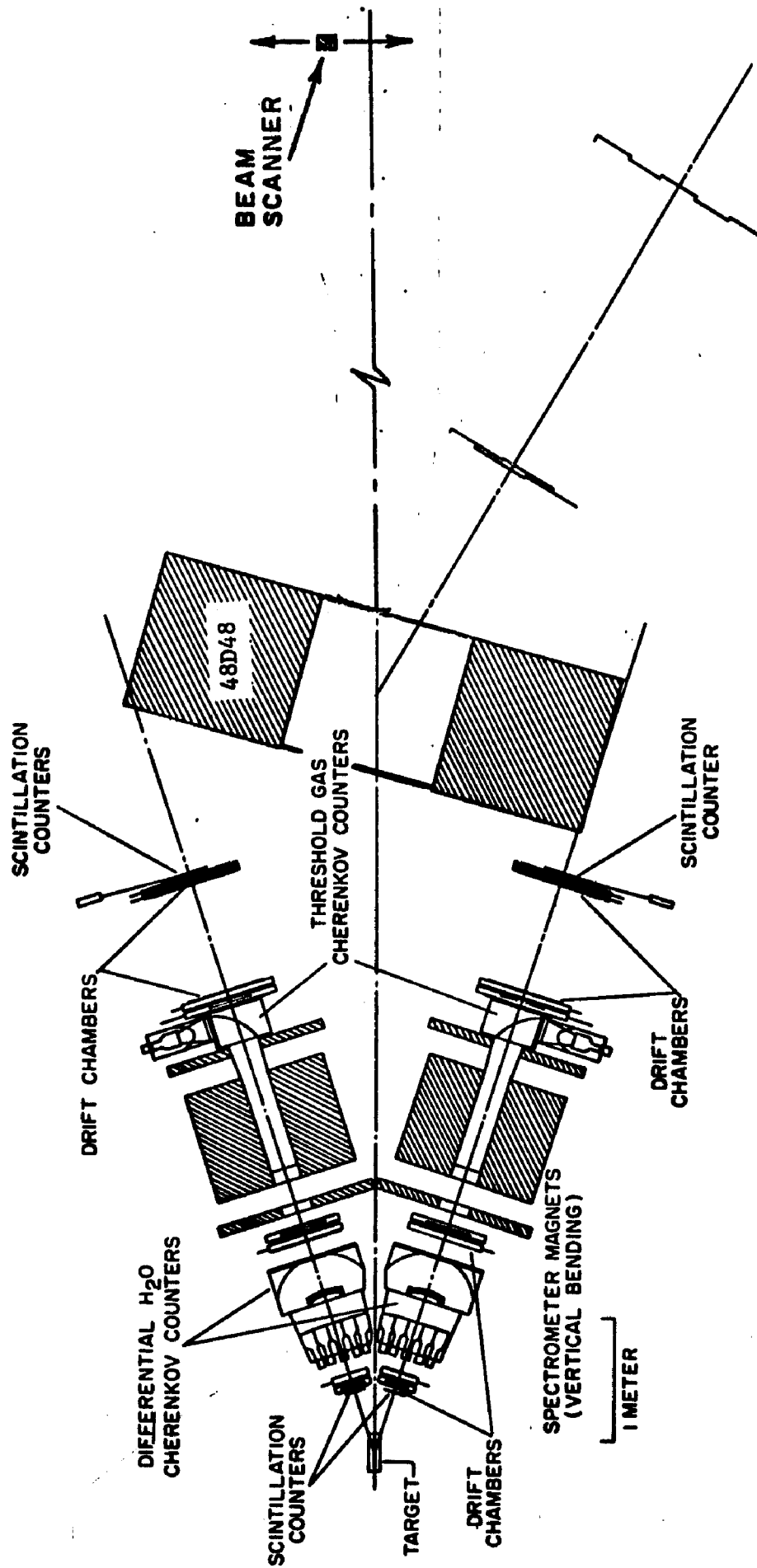


Figure 39

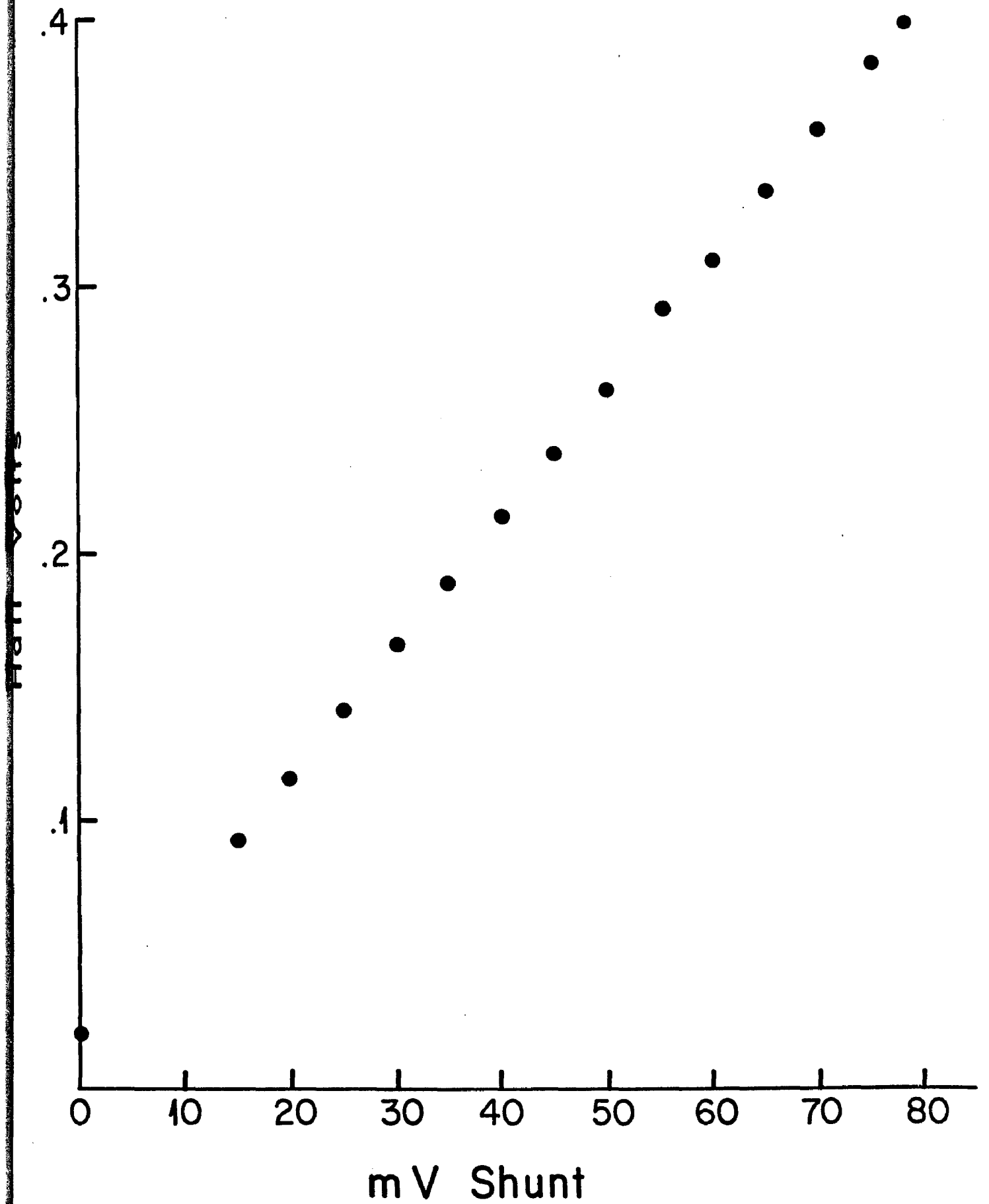


Figure 40

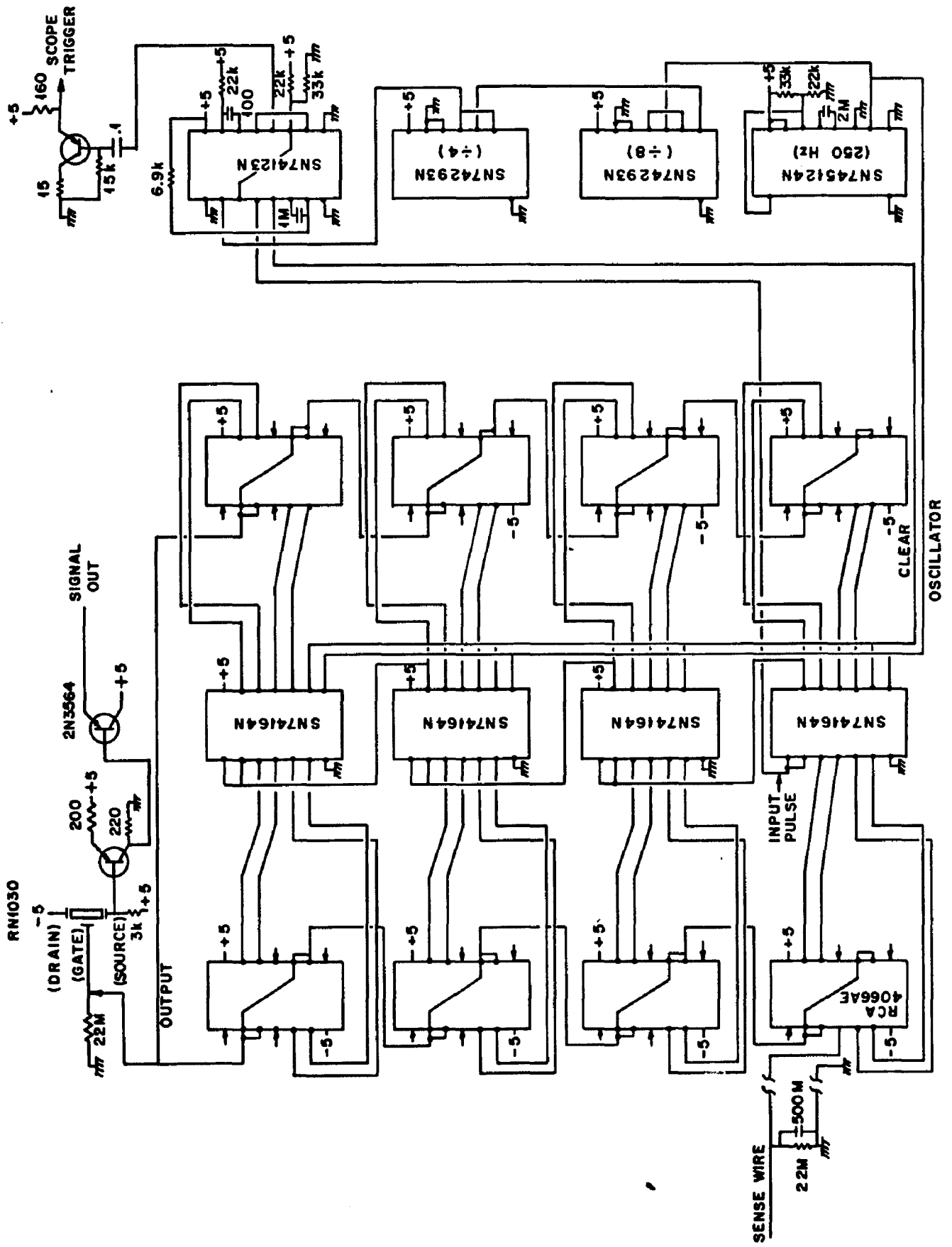


Figure 41

LOCATIONS of WIRE CHAMBERS

Table 2

R				L			
X		Y		X		Y	
1	2	1	2	1	2	1	2
-87.39	-86.28	-84.37	-83.26	-87.56	-86.41	-84.53	-83.33
-80.75	-80.75	-81.25	-81.25	-81.25	-81.25	-81.75	-81.75
-34.57	-33.50	-37.63	-36.54	-35.28	-34.20	-37.53	-36.41
42.84	43.83	46.06	47.02	42.74	43.73	45.95	46.96
		83.69	86.38			83.75	86.37

ACTIVE AREA of WIRE CHAMBERS

Table 3

1	6" X 6"
2	7" X 14"
3	10" X 36"
4	16" X 54"

LOCATIONS of SCINTILATORS

S1	-94"
S2	50"
S3	90"
S4	138"
S5	186"

Table 1

SECONDARY ANALYSIS CUTS

Table 4

	R	L
Counters	3%	.004%
Number of Hits, X 1.5 to 6.5	10.9%	9.6%
Number of Hits, Y 4.5 to 8.5	2.2%	2.3%
Standard Dev. of Track Fit, X 0. to .125	.04%	.2%
Standard Dev. of Track Fit, Y 0. to .150	.4%	.9%
Required Track in Front, Y	6.2%	6.2%
Required Track in Chamber 3X	.9%	1.3%

PARTICLE IDENTIFICATION CRITERIA

Table 5

Proton

- 1) Momentum less than 2.8 GeV/c
OUT less than 15
- 2) Momentum greater than 2.8 GeV/c
Threshold counter less than 3.5 counts
Correct RATIO

Kaon

- 1) SUM greater than 60 (70)
SUM less than 160 (170)
Correct RATIO

Pion

- 1) Threshold counter greater than 3.5 counts
Momentum greater than 2.8 GeV/c
SUM greater than 60 (70)
SUM less than 160 (170)
OUT greater than 15 (17)
- 2) Momentum less than 3.5 GeV/c
SUM greater than 60 (70)
SUM less than 160 (170)
Correct RATIO
OUT greater than 15 (17)

POL	ARM	THT	FULL	FULL	MT	FULL-MT	MT	FULL-MT	FULL-MT	DELTA	(DA+DB)/2	
A	R	1	2335.0	1720.0	0.0	2335.0 ± 48.3	0.0	1720.0 ± 41.5	0.1517 ±	0.0157	-0.0316 ±	
		2	2453.0	1803.0	0.0	2453.0 ± 49.5	0.0	1803.0 ± 42.5	0.1527 ±	0.0154	-0.0027 ±	
		3	2772.0	1962.0	0.0	2772.0 ± 52.6	0.0	1962.0 ± 44.3	0.1711 ±	0.0146	0.0138 ±	
	L	1	2287.0	2423.0	0.0	2287.0 ± 47.8	0.0	2423.0 ± 49.2	-0.0289 ±	0.0144	-0.0228 ±	
		2	1931.0	1983.0	0.0	1931.0 ± 43.9	0.0	1983.0 ± 44.5	-0.0133 ±	0.0158	-0.0006 ±	
		3	1826.0	1688.0	0.0	1826.0 ± 42.7	0.0	1688.0 ± 41.1	0.0393 ±	0.0168	0.0215 ±	
	B	R	1	1569.0	2428.0	0.0	1569.0 ± 39.6	0.0	2428.0 ± 49.3	-0.2149 ±	0.0161	0.0161
			2	1694.0	2279.0	0.0	1694.0 ± 41.2	0.0	2279.0 ± 47.7	-0.1472 ±	0.0160	-0.1472 ±
			3	1992.0	2659.0	0.0	1992.0 ± 44.6	0.0	2659.0 ± 51.6	-0.1434 ±	0.0148	-0.1434 ±
L		1	2305.0	2343.0	0.0	2305.0 ± 48.0	0.0	2343.0 ± 48.8	-0.0166 ±	0.0145	-0.0166 ±	
		2	1966.0	1919.0	0.0	1966.0 ± 44.3	0.0	1919.0 ± 43.8	0.0121 ±	0.0160	0.0121 ±	
		3	1735.0	1722.0	0.0	1735.0 ± 41.7	0.0	1722.0 ± 41.5	0.0038 ±	0.0168	0.0038 ±	
A		R	1	1709.0	1449.0	0.0	1709.0 ± 41.3	0.0	1449.0 ± 38.1	0.0823 ±	0.0178	-0.0194 ±
			2	1797.0	1477.0	0.0	1797.0 ± 42.4	0.0	1477.0 ± 38.4	0.0977 ±	0.0175	0.0050 ±
			3	2041.0	1531.0	0.0	2041.0 ± 45.2	0.0	1531.0 ± 39.1	0.1428 ±	0.0167	0.0359 ±
	L	1	1806.0	1833.0	0.0	1806.0 ± 42.5	0.0	1833.0 ± 42.8	-0.0074 ±	0.0165	-0.0168 ±	
		2	1423.0	1459.0	0.0	1423.0 ± 37.7	0.0	1459.0 ± 38.2	-0.0125 ±	0.0184	-0.0036 ±	
		3	1291.0	1239.0	0.0	1291.0 ± 35.9	0.0	1239.0 ± 35.2	0.0206 ±	0.0198	0.0018 ±	
	B	R	1	1309.0	1670.0	0.0	1309.0 ± 36.2	0.0	1670.0 ± 40.9	-0.1212 ±	0.0183	-0.1212 ±
			2	1415.0	1687.0	0.0	1415.0 ± 37.6	0.0	1687.0 ± 41.1	-0.0877 ±	0.0178	-0.0877 ±
			3	1650.0	1902.0	0.0	1650.0 ± 40.6	0.0	1902.0 ± 43.6	-0.0709 ±	0.0167	-0.0709 ±
L		1	1716.0	1808.0	0.0	1716.0 ± 41.4	0.0	1808.0 ± 42.5	-0.0261 ±	0.0167	-0.0261 ±	
		2	1436.0	1421.0	0.0	1436.0 ± 37.9	0.0	1421.0 ± 37.7	0.0053 ±	0.0186	0.0053 ±	
		3	1218.0	1260.0	0.0	1218.0 ± 34.9	0.0	1260.0 ± 35.5	-0.0169 ±	0.0198	-0.0169 ±	
A		R	1	344.0	365.0	0.0	344.0 ± 18.5	0.0	365.0 ± 19.1	-0.0296 ±	0.0367	-0.1020 ±
			2	419.0	359.0	0.0	419.0 ± 20.5	0.0	359.0 ± 18.9	0.0771 ±	0.0348	-0.0597 ±
			3	524.0	425.0	0.0	524.0 ± 22.9	0.0	425.0 ± 20.6	0.1043 ±	0.0318	-0.0006 ±
	L	1	367.0	456.0	0.0	367.0 ± 19.2	0.0	456.0 ± 21.4	-0.1081 ±	0.0342	-0.1039 ±	
		2	373.0	359.0	0.0	373.0 ± 19.3	0.0	359.0 ± 18.9	0.0191 ±	0.0369	-0.0273 ±	
		3	305.0	329.0	0.0	305.0 ± 17.5	0.0	329.0 ± 18.1	-0.0379 ±	0.0395	-0.0289 ±	
	B	R	1	289.0	411.0	0.0	289.0 ± 17.0	0.0	411.0 ± 20.3	-0.1743 ±	0.0377	-0.1743 ±
			2	317.0	472.0	0.0	317.0 ± 17.8	0.0	472.0 ± 21.7	-0.1965 ±	0.0362	-0.1965 ±
			3	420.0	519.0	0.0	420.0 ± 20.5	0.0	519.0 ± 22.8	-0.1054 ±	0.0321	-0.1054 ±
L		1	343.0	419.0	0.0	343.0 ± 18.5	0.0	419.0 ± 20.5	-0.0997 ±	0.0356	-0.0997 ±	
		2	320.0	371.0	0.0	320.0 ± 17.9	0.0	371.0 ± 19.3	-0.0738 ±	0.0377	-0.0738 ±	
		3	318.0	331.0	0.0	318.0 ± 17.8	0.0	331.0 ± 18.2	-0.0200 ±	0.0385	-0.0200 ±	

Table 6

POL	ARM	THT	MT +	MT -	FULL +	FULL -	FULL-MT +	FULL-MT -	DELTA	(DA+DB)/2	
A	R	1	242.0	172.0	0.0	0.0	242.0 ± 15.6	172.0 ± 13.1	0.490	0.287 ± 0.346	
		2	213.0	175.0	0.0	0.0	213.0 ± 14.6	175.0 ± 13.2	0.492	-0.240 ± 0.358	
		3	200.0	172.0	0.0	0.0	200.0 ± 14.1	172.0 ± 13.1	0.512	-0.267 ± 0.367	
	L	1	280.0	293.0	0.0	0.0	280.0 ± 16.7	293.0 ± 17.1	0.401	-0.241 ± 0.300	
		2	220.0	219.0	0.0	0.0	220.0 ± 14.8	219.0 ± 14.8	0.456	-0.312 ± 0.338	
		3	175.0	149.0	0.0	0.0	175.0 ± 13.2	149.0 ± 12.2	0.557	0.027 ± 0.374	
	B	R	1	143.0	229.0	0.0	0.0	183.0 ± 13.5	229.0 ± 15.1	0.488	0.117 ± 0.488
			2	158.0	212.0	0.0	0.0	158.0 ± 12.6	212.0 ± 14.6	0.519	-0.1459 ± 0.519
			3	159.0	206.0	0.0	0.0	159.0 ± 12.6	206.0 ± 14.4	0.525	-0.1288 ± 0.525
L		1	230.0	242.0	0.0	0.0	230.0 ± 15.2	242.0 ± 15.6	0.445	-0.254 ± 0.445	
		2	188.0	214.0	0.0	0.0	188.0 ± 13.7	214.0 ± 14.6	0.499	-0.0647 ± 0.499	
		3	167.0	194.0	0.0	0.0	167.0 ± 12.9	194.0 ± 13.9	0.500	-0.0748 ± 0.500	
A		R	1	172.0	146.0	0.0	0.0	172.0 ± 13.1	146.0 ± 12.1	0.536	0.287 ± 0.384
			2	177.0	131.0	0.0	0.0	177.0 ± 13.3	131.0 ± 11.4	0.558	0.597 ± 0.397
			3	179.0	154.0	0.0	0.0	179.0 ± 13.4	154.0 ± 12.4	0.542	-0.0019 ± 0.390
	L	1	215.0	231.0	0.0	0.0	215.0 ± 14.7	231.0 ± 15.2	0.471	-0.203 ± 0.332	
		2	167.0	168.0	0.0	0.0	167.0 ± 12.9	168.0 ± 13.0	0.537	-0.0045 ± 0.378	
		3	137.0	121.0	0.0	0.0	137.0 ± 11.7	121.0 ± 11.0	0.621	-0.266 ± 0.449	
	B	R	1	160.0	168.0	0.0	0.0	160.0 ± 12.6	168.0 ± 13.0	0.549	0.244 ± 0.549
			2	146.0	155.0	0.0	0.0	146.0 ± 12.1	155.0 ± 12.4	0.565	-0.299 ± 0.565
			3	140.0	164.0	0.0	0.0	140.0 ± 11.8	164.0 ± 12.8	0.561	-0.0789 ± 0.561
L		1	213.0	215.0	0.0	0.0	213.0 ± 14.6	215.0 ± 14.7	0.467	0.0047 ± 0.467	
		2	168.0	170.0	0.0	0.0	168.0 ± 13.0	170.0 ± 13.0	0.533	-0.0059 ± 0.533	
		3	96.0	121.0	0.0	0.0	96.0 ± 9.8	121.0 ± 11.0	0.649	-0.1152 ± 0.649	
A		R	1	34.0	59.0	0.0	0.0	34.0 ± 5.8	59.0 ± 7.7	0.1002	-0.2058 ± 0.737
			2	32.0	56.0	0.0	0.0	32.0 ± 5.7	56.0 ± 7.5	0.1060	-0.2153 ± 0.715
			3	52.0	45.0	0.0	0.0	52.0 ± 7.2	45.0 ± 6.7	0.0930	-0.0225 ± 0.650
	L	1	50.0	57.0	0.0	0.0	50.0 ± 7.1	57.0 ± 7.5	0.0937	-0.1308 ± 0.668	
		2	43.0	59.0	0.0	0.0	43.0 ± 6.6	59.0 ± 7.7	0.0992	-0.0942 ± 0.686	
		3	46.0	36.0	0.0	0.0	46.0 ± 6.8	36.0 ± 6.0	0.1106	0.1165 ± 0.786	
	B	R	1	36.0	48.0	0.0	0.0	36.0 ± 6.0	48.0 ± 6.9	0.1082	0.1429 ± 1.082
			2	40.0	55.0	0.0	0.0	40.0 ± 6.3	55.0 ± 7.4	0.0959	-0.1579 ± 0.959
			3	44.0	62.0	0.0	0.0	44.0 ± 7.0	62.0 ± 7.9	0.0907	-0.1171 ± 0.907
L		1	43.0	64.0	0.0	0.0	43.0 ± 6.6	64.0 ± 8.0	0.0952	-0.1463 ± 0.952	
		2	46.0	49.0	0.0	0.0	46.0 ± 6.8	49.0 ± 7.0	0.0948	-0.0316 ± 0.948	
		3	45.0	36.0	0.0	0.0	45.0 ± 6.7	36.0 ± 6.0	0.1118	0.1111 ± 1.118	

Table 7

POL	ARM	THT	FULL +	FULL -	MT +	MT -	FULL-MT +	FULL-MT -	DELTA	(DA+DB)/2	
A	R	1	2160.0	475.0	255.0	67.0	1713.8 ± 72.2	357.8 ± 34.4	.6546 ±	.4956 ±	
		2	2576.0	540.0	279.0	71.0	2087.8 ± 78.3	415.8 ± 36.4	.6679 ±	.5477 ±	
		3	3414.0	597.0	331.0	73.0	2834.8 ± 89.4	469.3 ± 38.1	.7160 ±	.6337 ±	
	L	1	1772.0	537.0	263.0	92.0	1311.8 ± 66.8	376.0 ± 37.4	.5544 ±	.5837 ±	
		2	1762.0	486.0	293.0	80.0	1249.3 ± 67.4	346.0 ± 35.4	.5662 ±	.6025 ±	
		3	1852.0	388.0	219.0	56.0	1468.8 ± 66.9	290.0 ± 31.2	.6702 ±	.6883 ±	
	B	R	1	1477.0	673.0	208.0	63.0	1167.1 ± 59.8	579.1 ± 39.2	.3367 ±	.0429
			2	1828.0	703.0	235.0	74.0	1477.9 ± 66.0	592.7 ± 40.3	.4275 ±	.0404
			3	2625.0	774.0	266.0	87.0	2228.7 ± 77.7	644.4 ± 42.5	.5514 ±	.0350
L		1	1874.0	468.0	228.0	67.0	1534.3 ± 66.5	368.2 ± 33.7	.6130 ±	.0456	
		2	1733.0	412.0	231.0	71.0	1388.8 ± 64.5	306.2 ± 32.2	.6387 ±	.0504	
		3	1977.0	362.0	217.0	52.0	1653.7 ± 67.8	284.5 ± 29.6	.7064 ±	.0467	
A		R	1	1329.0	423.0	193.0	60.0	991.3 ± 57.7	318.0 ± 32.5	.5142 ±	.0567
			2	1552.0	451.0	183.0	55.0	1231.8 ± 61.2	354.8 ± 33.1	.5528 ±	.0497
			3	2186.0	517.0	236.0	66.0	1773.0 ± 72.1	401.5 ± 35.6	.6307 ±	.0435
	L	1	1349.0	533.0	205.0	63.0	990.3 ± 58.4	422.8 ± 35.9	.4016 ±	.0519	
		2	1227.0	424.0	172.0	69.0	926.0 ± 55.3	303.3 ± 33.0	.5066 ±	.0584	
		3	1248.0	338.0	196.0	53.0	905.0 ± 56.4	245.3 ± 29.4	.5736 ±	.0631	
	B	R	1	1072.0	568.0	150.0	60.0	848.5 ± 50.9	478.6 ± 36.3	.2787 ±	.0485
			2	1231.0	538.0	181.0	77.0	961.3 ± 54.8	423.3 ± 36.1	.3886 ±	.0504
			3	1862.0	582.0	221.0	79.0	1532.7 ± 66.2	464.3 ± 37.4	.5350 ±	.0432
L		1	1282.0	494.0	192.0	58.0	995.9 ± 56.0	407.6 ± 34.1	.4192 ±	.0502	
		2	1205.0	376.0	156.0	58.0	972.6 ± 53.6	249.6 ± 30.4	.5411 ±	.0550	
		3	1287.0	318.0	152.0	37.0	1060.5 ± 55.0	262.9 ± 27.3	.6027 ±	.0538	
A		R	1	324.0	170.0	86.0	42.0	173.5 ± 30.8	96.5 ± 22.1	.2852 ±	.1425
			2	446.0	212.0	82.0	49.0	302.5 ± 34.3	126.3 ± 24.4	.4111 ±	.1059
			3	556.0	247.0	93.0	51.0	393.3 ± 37.9	157.8 ± 25.9	.4274 ±	.0888
	L	1	413.0	248.0	108.0	50.0	224.0 ± 34.7	160.5 ± 25.9	.1651 ±	.1133	
		2	416.0	224.0	69.0	37.0	295.3 ± 32.8	154.3 ± 24.0	.2992 ±	.0919	
		3	374.0	192.0	85.0	37.0	225.3 ± 32.3	127.3 ± 22.7	.2780 ±	.1148	
	B	R	1	319.0	223.0	72.0	36.0	211.7 ± 29.2	169.4 ± 23.5	.1112 ±	.0977
			2	351.0	225.0	85.0	45.0	224.4 ± 30.9	158.0 ± 24.2	.1737 ±	.1035
			3	492.0	216.0	81.0	46.0	371.3 ± 35.0	147.5 ± 23.9	.4315 ±	.0882
L		1	412.0	266.0	82.0	50.0	289.8 ± 32.7	141.5 ± 26.1	.2043 ±	.0869	
		2	398.0	200.0	74.0	50.0	287.7 ± 31.9	125.5 ± 23.4	.3926 ±	.1014	
		3	324.0	169.0	69.0	38.0	221.2 ± 29.2	112.4 ± 21.2	.3262 ±	.1135	

Table 8

PUL	ARM	THT	FULL \blacktriangleright	FULL -	MT \blacktriangleright	MT -	FULL-MT \blacktriangleright	FULL-MT -	DELTA	(DA*DB)/2
A	R	1	135.8	156.8	24.3	28.3	93.3 \pm 13.8	107.2 \pm 14.5	-.0692 \pm	.1000
		2	139.4	113.1	24.3	34.7	96.8 \pm 13.9	52.4 \pm 13.3	.2975 \pm	.1328
		3	107.5	90.3	14.8	21.5	81.7 \pm 12.1	52.7 \pm 11.4	.2159 \pm	.1219
A	L	1	100.0	119.1	26.0	28.7	54.5 \pm 12.3	68.9 \pm 13.1	-.1170 \pm	.1388
		2	85.8	96.0	23.7	19.6	44.3 \pm 11.7	61.6 \pm 11.5	-.1637 \pm	.1531
		3	85.8	101.0	17.4	10.8	55.3 \pm 11.2	82.1 \pm 11.0	-.1951 \pm	.1112
B	R	1	115.8	178.5	31.6	43.1	73.4 \pm 12.9	120.7 \pm 15.5	-.2438 \pm	.1060
		2	75.3	132.8	29.5	30.1	35.8 \pm 11.2	92.5 \pm 13.3	-.4422 \pm	.1449
		3	97.6	138.2	19.4	28.1	71.6 \pm 11.7	100.5 \pm 13.4	-.1680 \pm	.1001
B	L	1	106.0	146.8	22.0	43.4	76.5 \pm 11.9	88.6 \pm 14.4	-.0736 \pm	.1093
		2	64.6	100.2	16.6	22.6	42.3 \pm 9.6	69.9 \pm 11.5	-.2461 \pm	.1285
		3	73.7	102.2	16.7	20.7	51.3 \pm 10.2	74.5 \pm 11.5	-.1844 \pm	.1213
A	R	1	100.5	109.9	28.7	29.8	50.2 \pm 12.5	57.7 \pm 12.8	-.0689 \pm	.1579
		2	77.6	104.4	20.2	22.5	42.3 \pm 10.9	65.0 \pm 12.1	-.2115 \pm	.1525
		3	77.1	88.9	12.3	10.6	55.6 \pm 10.3	70.3 \pm 10.5	-.1164 \pm	.1120
A	L	1	100.9	126.1	26.0	21.5	55.3 \pm 12.3	88.5 \pm 12.9	-.2306 \pm	.1213
		2	73.0	80.5	10.8	10.7	54.1 \pm 9.8	61.8 \pm 10.0	-.0668 \pm	.1211
		3	51.2	74.6	12.1	6.8	30.0 \pm 8.8	62.7 \pm 9.3	-.3530 \pm	.1373
B	R	1	87.1	121.8	23.5	31.7	55.7 \pm 11.2	79.3 \pm 12.9	-.1751 \pm	.1279
		2	61.1	115.5	32.6	18.6	17.3 \pm 10.5	90.6 \pm 11.9	-.6786 \pm	.1680
		3	71.5	109.7	13.6	24.8	53.2 \pm 9.8	76.4 \pm 12.0	-.1791 \pm	.1175
B	L	1	81.0	94.5	17.3	27.6	57.9 \pm 10.4	57.6 \pm 11.5	.0028 \pm	.1299
		2	66.9	69.2	11.2	22.8	52.0 \pm 9.3	38.7 \pm 10.0	.1462 \pm	.1449
		3	57.9	79.2	10.3	14.8	44.1 \pm 8.7	59.4 \pm 10.0	-.1476 \pm	.1270
A	R	1	19.0	32.0	6.0	13.0	8.5 \pm 5.4	9.3 \pm 7.4	-.0423 \pm	.5075
		2	19.0	26.0	7.0	8.0	6.8 \pm 5.6	12.0 \pm 6.3	-.2800 \pm	.4431
		3	20.0	33.0	3.0	7.0	14.8 \pm 5.0	20.8 \pm 6.7	-.1690 \pm	.2285
A	L	1	16.0	27.0	6.0	8.0	5.5 \pm 5.1	13.0 \pm 6.4	-.4054 \pm	.4666
		2	15.0	15.0	2.0	3.0	11.5 \pm 4.3	9.8 \pm 4.5	.0824 \pm	.2833
		3	21.0	18.0	5.0	1.0	12.3 \pm 5.5	16.3 \pm 4.4	-.1404 \pm	.2480
B	R	1	12.0	35.0	11.0	7.0	-2.7 \pm 5.2	25.6 \pm 6.7	-1.2395 \pm	.5569
		2	25.0	23.0	7.0	13.0	15.6 \pm 5.9	5.6 \pm 6.4	.4736 \pm	.4175
		3	28.0	30.0	7.0	7.0	18.6 \pm 6.1	20.6 \pm 6.3	-.0510 \pm	.2041
B	L	1	14.0	28.0	5.0	5.0	7.3 \pm 4.5	21.3 \pm 5.9	-.4895 \pm	.2725
		2	23.0	24.0	5.0	5.0	16.3 \pm 5.4	17.3 \pm 5.5	-.0298 \pm	.2084
		3	9.0	15.0	4.0	5.0	3.6 \pm 3.8	8.3 \pm 4.7	-.3903 \pm	.5394

Table 9

POL	ARM	THT	FULL	FULL	MT	FULL-MT	MT -	FULL-MT	FULL-MT -	DELTA	(DA+DB)/2
A	R	1	2183.8	1686.8	224.2	167.3	1791.5 ± 52.5	1394.0 ± 45.0	.1248 ±	.0218	-.0651 ±
		2	2272.7	1765.2	193.5	170.0	1934.1 ± 53.2	1467.6 ± 45.9	.1371 ±	.0208	-.0179 ±
		3	2533.0	1920.2	176.8	166.9	2223.6 ± 55.9	1628.2 ± 47.6	.1546 ±	.0192	-.0133 ±
	L	1	2163.0	2385.4	261.6	286.6	1705.2 ± 52.7	1883.9 ± 54.2	-.0498 ±	.0209	-.0433 ±
		2	1807.7	1949.0	199.5	213.4	1458.6 ± 48.1	1575.5 ± 48.6	-.0386 ±	.0224	-.0177 ±
		3	1696.4	1660.8	159.7	145.1	1416.9 ± 46.2	1407.0 ± 44.1	.0035 ±	.0223	-.0059 ±
	R	1	1465.6	2380.9	168.4	224.6	1214.6 ± 42.9	2046.3 ± 52.6	-.2550 ±	.0212	.0250 ±
		2	1566.0	2229.8	141.6	206.8	1355.1 ± 43.9	1921.6 ± 50.9	-.1729 ±	.0208	.0208 ±
		3	1808.3	2604.8	140.4	199.9	1599.1 ± 47.2	2307.0 ± 54.5	-.1812 ±	.0187	.0187 ±
L	1	2173.8	2350.2	214.0	237.3	1854.9 ± 51.5	1996.6 ± 52.4	-.0368 ±	.0190	.0190 ±	
	2	1844.7	1890.2	171.8	209.0	1588.7 ± 47.4	1578.7 ± 47.3	.0031 ±	.0208	.0208 ±	
	3	1596.6	1696.7	151.8	190.4	1370.4 ± 44.5	1413.0 ± 44.8	-.0153 ±	.0226	.0226 ±	
A	R	1	1638.0	1427.5	161.6	142.4	1355.3 ± 44.8	1178.4 ± 41.3	.0698 ±	.0237	-.0415 ±
		2	1714.9	1453.6	167.7	128.2	1421.4 ± 45.9	1229.3 ± 41.3	.0725 ±	.0231	-.0198 ±
		3	1923.2	1503.9	166.6	150.5	1631.7 ± 48.5	1240.5 ± 42.4	.1362 ±	.0225	.0219 ±
	L	1	1736.2	1807.7	204.5	228.0	1378.3 ± 46.7	1408.7 ± 47.3	-.0109 ±	.0237	-.0272 ±
		2	1359.2	1438.8	158.3	164.3	1082.2 ± 41.4	1151.3 ± 41.9	-.0309 ±	.0260	-.0196 ±
		3	1224.5	1223.1	126.8	118.4	1002.7 ± 39.1	1015.9 ± 38.1	-.0066 ±	.0268	-.0146 ±
	R	1	1252.1	1640.6	152.4	165.1	1025.0 ± 39.3	1394.6 ± 43.8	-.1528 ±	.0242	.0242 ±
		2	1348.6	1659.5	136.6	151.0	1145.1 ± 40.4	1434.4 ± 43.8	-.1122 ±	.0230	.0230 ±
		3	1549.5	1872.6	128.6	160.0	1357.9 ± 43.1	1634.3 ± 46.3	-.0924 ±	.0211	.0211 ±
L	1	1650.7	1785.3	203.6	211.9	1347.3 ± 45.1	1469.5 ± 46.1	-.0434 ±	.0227	.0227 ±	
	2	1373.3	1402.7	159.9	167.0	1135.0 ± 41.1	1153.9 ± 40.9	-.0082 ±	.0249	.0249 ±	
	3	1151.3	1244.1	88.8	119.4	1019.0 ± 36.9	1066.2 ± 38.0	-.0226 ±	.0249	.0249 ±	
A	R	1	344.0	365.0	34.0	59.0	284.5 ± 20.1	261.8 ± 21.6	.0416 ±	.0531	-.0697 ±
		2	419.0	359.0	32.0	56.0	363.0 ± 21.8	261.0 ± 21.4	.1635 ±	.0487	-.0207 ±
		3	524.0	425.0	52.0	45.0	433.0 ± 24.8	346.3 ± 22.4	.1113 ±	.0426	.0042 ±
	L	1	367.0	456.0	50.0	57.0	279.5 ± 21.3	356.3 ± 23.6	-.1207 ±	.0491	-.0975 ±
		2	373.0	359.0	43.0	59.0	297.8 ± 21.2	255.8 ± 21.5	.0759 ±	.0544	-.0044 ±
		3	305.0	329.0	46.0	36.0	224.5 ± 19.6	266.0 ± 19.8	-.0846 ±	.0552	-.0673 ±
	R	1	289.0	411.0	36.0	48.0	235.4 ± 18.5	339.5 ± 22.0	-.1811 ±	.0495	.0495 ±
		2	317.0	472.0	40.0	55.0	257.4 ± 19.4	340.1 ± 23.5	-.2049 ±	.0473	.0473 ±
		3	420.0	519.0	49.0	62.0	347.0 ± 22.2	426.6 ± 24.7	-.1029 ±	.0429	.0429 ±
L	1	343.0	419.0	43.0	64.0	278.9 ± 20.2	323.6 ± 22.7	-.0742 ±	.0499	.0499 ±	
	2	320.0	371.0	46.0	49.0	251.5 ± 19.7	298.0 ± 21.1	-.0847 ±	.0511	.0511 ±	
	3	318.0	331.0	45.0	36.0	251.0 ± 19.6	277.4 ± 19.6	-.0500 ±	.0512	.0512 ±	

Table 10

CHARGE ASYMMETRIES

Table 11

	P_t Bin (GeV/c)		
	.48 to .67	.67 to 1.0	1.0 to 2.7
\bar{P} Incident			
R	$.0001 \pm .0148$	$.0343 \pm .0187$	$.0280 \pm .0390$
L	$.0023 \pm .0171$	$-.0111 \pm .0216$	$-.0315 \pm .0468$
(R+L)/2	$.0012 \pm .0113$	$.0116 \pm .0143$	$-.0018 \pm .0305$
Pion Incident			
R	$.0497 \pm .0870$	$-.2033 \pm .1009$	$.0195 \pm .2230$
L	$-.2186 \pm .0914$	$-.2095 \pm .1110$	$.0279 \pm .3506$
(R+L)/2	$-.0845 \pm .0631$	$-.2064 \pm .0750$	$.0237 \pm .2077$
(R+L)/66	$-.0025 \pm .0021$	$-.0062 \pm .0023$	$.0007 \pm .0062$
\bar{P} Incident Minus Pion Incident	$.0037 \pm .0115$	$.0178 \pm .0145$	$-.0025 \pm .0311$
Systematic Error	$\pm .014$	$\pm .009$	± 0.0